CHEMISTRY
A European Journal

Supporting Information

Size-Selective Hydroformylation by a Rhodium Catalyst Confined in a Supramolecular Cage

Sandra S. Nurttila,[a] Wolfgang Brenner,[b] Jesús Mosquera,[b] Kaj M. van Vliet,[a] Jonathan R. Nitschke,[b] and Joost N. H. Reek*[a]

chem_201804333_sm_miscellaneous_information.pdf

Supplementary Materials for

Size-selective hydroformylation by a rhodium catalyst confined in a supramolecular cage

Sandra S. Nurttila,[a] Wolfgang Brenner,[b] Jesús Mosquera,[b] Kaj M. van Vliet,[a] Jonathan R. Nitschke,[b] and Joost N. H. Reek*[a]

[a] S.S. Nurttila, Prof. Dr. J.N.H. Reek

Homogeneous, Supramolecular and Bio-Inspired Catalysis, Van 't Hoff Institute for Molecular Sciences

University of Amsterdam

Science Park 904, 1098XH Amsterdam (The Netherlands)

[b] Dr. Wolfgang Brenner, Dr. Jesús Mosquera, Prof. Dr. J.R. Nitschke

Department of Chemistry, University of Cambridge

Lensfield Road, CB2 1EW Cambridge (United Kingdom)

Email: j.n.h.reek@uva.nl

Contents

1. Materials and methods 3
2. Synthesis and characterisation of ligands **L1**, **L2** and **L3** 4
3. Synthesis and characterisation of **Au1** 9
4. Synthesis and characterisation of building block **Zn-P** 12
5. Synthesis and characterisation of **Fe_4(Zn-L)$_6$** 16
6. Synthesis and characterisation of substrate **Sub1** 23
7. Binding studies of **Fe_4(Zn-L)$_6$** with various guests 25
8. Encapsulation studies of **Fe_4(Zn-L)$_6$** with various guests 43
9. Formation and characterization of the active species 62
10. Cage and guest volume determination 72
11. XTB and DFT calculations 73
12. Catalysis 78
13. High-pressure Infrared (HP IR) studies under syngas 80
14. Cage stability under hydroformylation conditions 81
15. General titration fitting procedure 81
16. References 84

1. Materials and methods

All reactions were carried out under an atmosphere of N_2 using standard Schlenk techniques when noted. All solvents were distilled prior to use by conventional methods. NMR spectra were recorded on a Bruker AMX 300 (300.1 MHz, 75.5 MHz and 121.5 MHz for ^{1}H, ^{13}C and ^{31}P respectively), Bruker AMX 400 (400.1 MHz, 100.6 MHz and 162.0 MHz for ^{1}H, ^{13}C and ^{31}P respectively) and Bruker AMX 500 (500.1 MHz, 125.8 MHz and 202.5 MHz for ^{1}H, ^{13}C and ^{31}P respectively). ^{1}H NMR spectral data are referenced to the solvent residual signal (7.26 ppm for $CDCl_3$, 3.58 ppm for THF-d_8, 5.32 ppm for CD_2Cl_2 and 1.32 ppm for CD_3CN), ^{31}P NMR data are given relative to external H_3PO_4 and ^{19}F NMR data are given relative to external $CFCl_3$. 2D ^{1}H-DOSY spectral data were performed with temperature and gradient calibration prior to the measurements, and the temperature was kept at 298 K during the measurements. Low resolution electrospray ionisation mass spectra (ESI-MS) were obtained on a Micromass Quattro LC. Detection was in positive-ion mode, the cone voltage was 13 eV, the desolvation and ionisation temperature were 313 K. The solution was infused from a Harvard Syringe Pump at a rate of 10 µL per minute. Coldspray ionisation mass spectra (CSI-MS) were obtained on an AccuTOF LC, JMS-T100LP Mass spectrometer (JEOL, Japan). Detection was in positive-ion mode, needle voltage 2000 V, Orifice 1 voltage 90 V, Orifice 2 voltage 9 V, Ring Lens voltage 22 V, ion source temperature 80°C, spray temperature 250°C, flow injection with a flow rate of 0.01 mL/min. High resolution mass spectra of cage samples were collected on a HR-ToF Bruker Daltonik GmbH (Bremen, Germany) Impact II, an ESI-ToF MS capable of resolution of at least 40000 FWHM, which was coupled to a Bruker cryospray unit. Detection was in positive-ion mode and the source voltage was between 4 and 6 kV. The flow rates were 18 ul/hr. The drying gas (N_2) was held at -35 °C and the spray gas was held at – 40 °C. The machine was calibrated prior to every experiment via direct infusion of a TFA-Na solution, which provided a m/z range of singly charged peaks up to 3500 Da in both ion modes. UV-Vis spectroscopy was performed on a single beam Hewlett Packard 8453 spectrometer and a double beam Shimadzu UV-2600 spectrometer in a quartz cuvette with a path length of 10 mm using the solvent as a background. IR measurements were conducted on a Thermo Nicolet Nexus FT-IR spectrometer. Gas chromatographic analyses were conducted on Shimadzu GC-17A apparatus (split/splitless injector, J&W 30 m column, film thickness 3.0 µm, carrier gas 70kPa He, FID detector) and Trace GC ultra-apparatus (split/splitless injector, Restek RTX1 column, film thickness 0.25 µm, carrier gas 70kPa He, FID detector). All reagents were purchased from commercial suppliers and used without further purification.

2. Synthesis and characterisation of ligands L1, L2 and L3

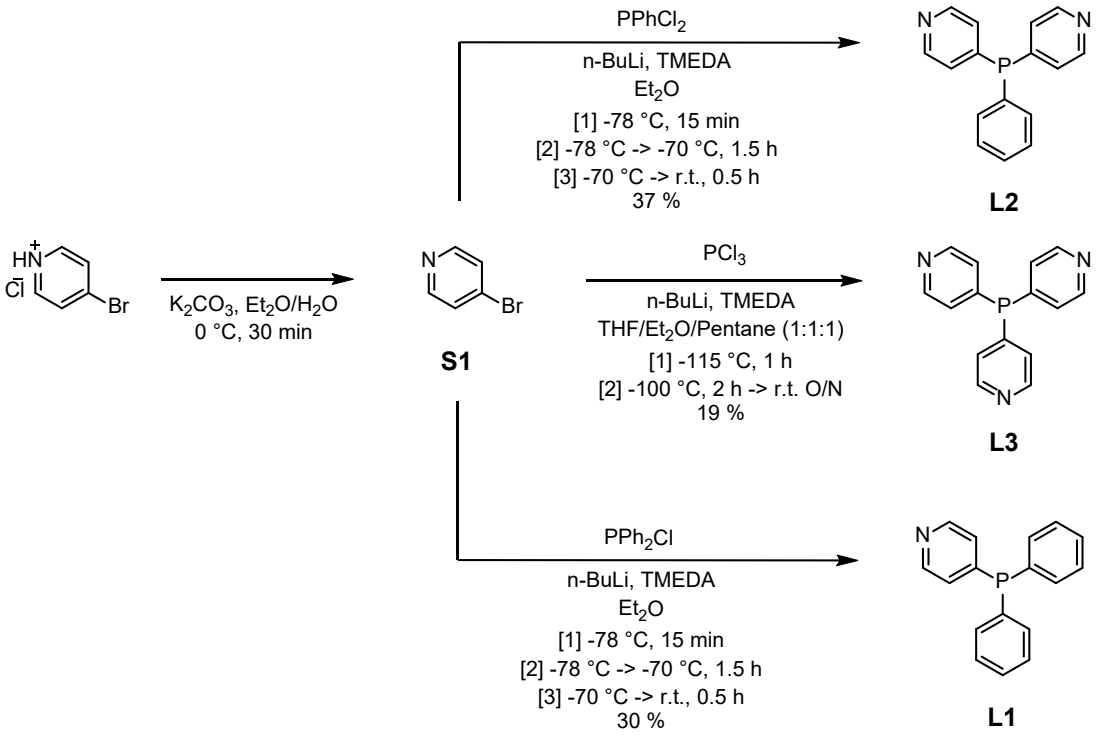

L1, L2 and L3 were synthesised using two modified literature procedures[1,2]:

4-bromopyridine (S1):

4-bromopyridine hydrochloride (5.5 g, 28.3 mmol) and K_2CO_3 (11.7 g, 84.9 mmol) were dissolved in water (300 mL) at 0°C, resulting in effervescence and the separation of a yellow oily layer from the aqueous phase. The mixture was continuously stirred for 30 min while maintaining a temperature of 0°C to avoid polymerisation of the formed **S1**. Next, the yellow oil was separated from the aqueous phase and the water layer was extracted with diethyl ether (3 x 70 mL). The oil and the combined organic phases were dried over $MgSO_4$, filtered and the solvent was removed under reduced pressure at 0°C to give **S1** as a yellow oil. The oil was immediately used for the next step without further purification.

4-(Diphenylphosphaneyl)pyridine (L1):

n-BuLi (9.4 mL, 23.5 mmol, 2.5 M in hexanes) and freshly distilled and dried TMEDA (3.5 mL, 23.5 mmol) were transferred along with diethyl ether (20 mL) into a flame-dried Schlenk flask under N_2 atmosphere. The yellow solution was stirred at room temperature for 15 min, where after it was cooled to -78°C using a dry ice/acetone cooling bath. Subsequently, a solution of **S1** (3.1 mL, 32.6 mmol) in diethyl ether (40 mL) was added dropwise over 15 min, while keeping the temperature at -78°C. After 15 min of stirring the brown-red reaction mixture, a solution of PPh_2Cl (3.3 mL, 18.1 mmol) in diethyl ether (20 mL) was added dropwise, where after the resulting brown reaction mixture was stirred for 1.5 h at -75°C and then allowed to come to room temperature over 30 minutes. Next, a few blocks of ice and NH_4OH (aq) (8 mL) were added to the beige suspension, where after the organic layer was separated and washed with degassed water (3 x 100 mL). The organic phase was dried with $MgSO_4$, filtered and the solvent was removed under reduced pressure to give an orange-brown oil. The crude product was purified by column chromatography (silica, eluent: dichloromethane + 2% MeOH and 1% triethylamine) under N_2

atmosphere to give **L1** as colourless crystals in 30% yield. ^{1}H NMR (300 MHz, $CDCl_3$) δ (ppm) = 8.53 – 8.48 (m, 1H), 7.42 – 7.31 (m, 5H), 7.10 (t, *J* = 6.2 Hz, 1H); ^{31}P NMR (121 MHz, $CDCl_3$) δ (ppm) = -7.05.

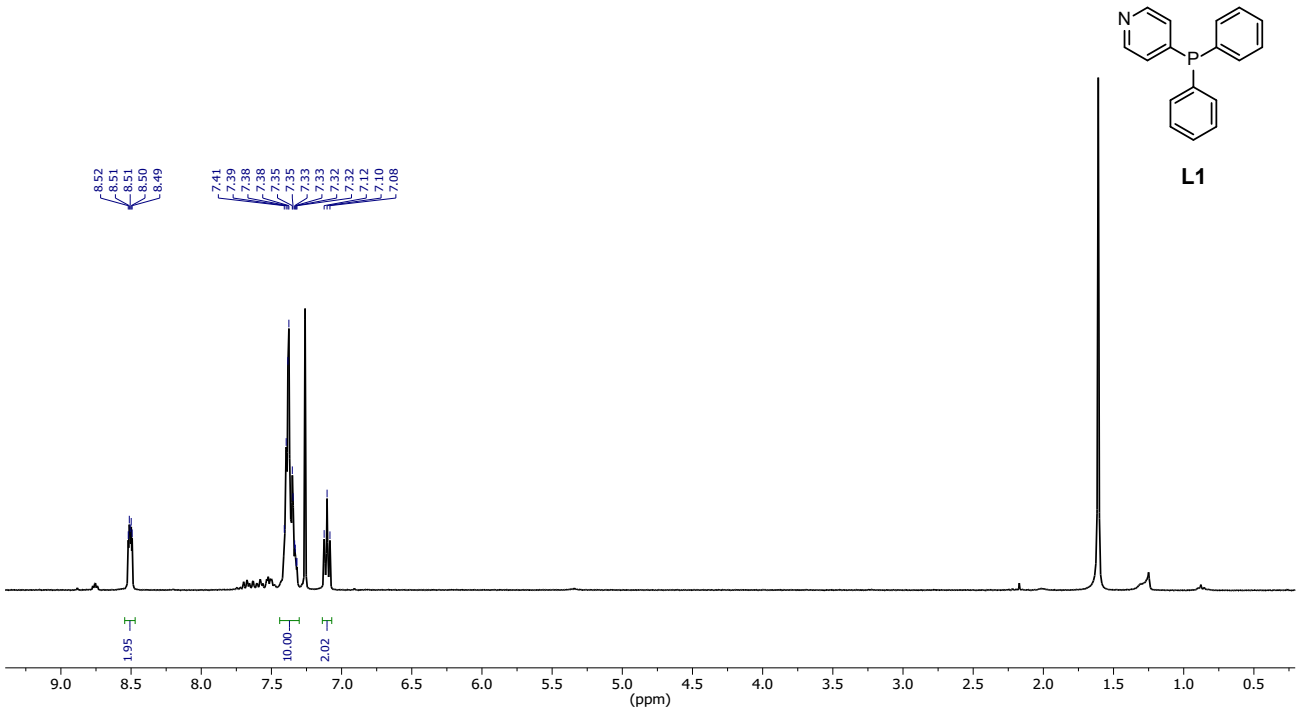

Figure S 1. ^{1}H NMR (300 MHz, 298 K) of **L1** in $CDCl_3$.

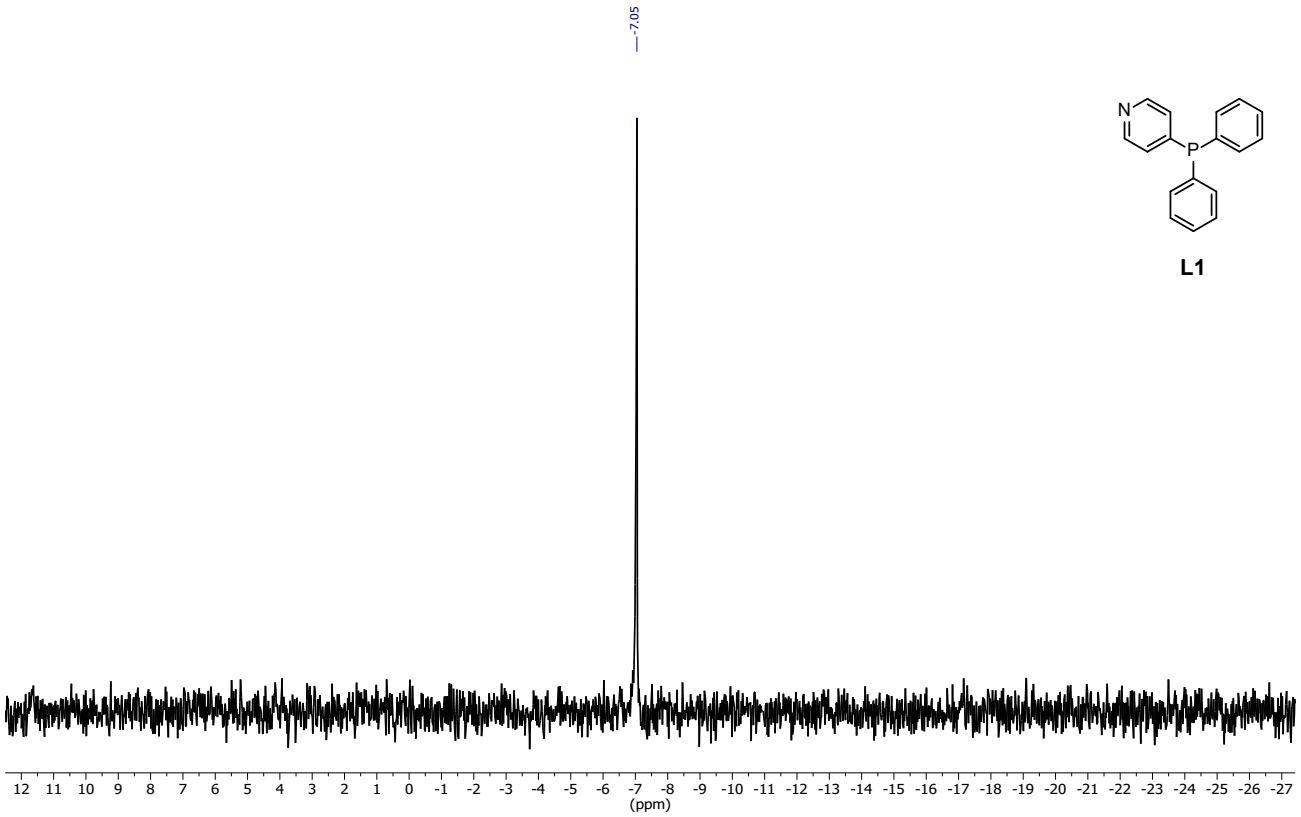

Figure S 2. ^{31}P NMR (121 MHz, 298 K) of **L1** in $CDCl_3$.

4,4'-(Phenylphosphanediyl)dipyridine (L2):

n-BuLi (4.5 mL, 11.3 mmol, 2.5 M in hexanes) and freshly distilled and dried TMEDA (1.7 mL, 11.3 mmol) were transferred along with diethyl ether (9 mL) into a flame-dried Schlenk flask under N_2 atmosphere. The yellow solution was stirred at room temperature for 15 min, where after it was cooled to -78°C using a dry ice/acetone cooling bath. Subsequently, a solution of **S1** (1.4 mL, 14.8 mmol) in diethyl ether (17 mL) was added dropwise over 15 min, while keeping the temperature at -78°C. After 15 min of stirring the brown-red reaction mixture, a solution of $PPhCl_2$ (0.6 mL, 4.9 mmol) in diethyl ether (5 mL) was added dropwise, where after the resulting dark yellow reaction mixture was stirred for 1.5 h at -75°C and then allowed to come to room temperature over 30 minutes. Next, a few blocks of ice and NH_4OH (aq) (4.3 mL) were added to the suspension, where after the organic layer was separated and washed with degassed water (3 x 100 mL). The organic phase was dried with $MgSO_4$, filtered and the solvent was removed under reduced pressure to give a red-orange oil. The crude product was purified by column chromatography (silica, eluent: dichloromethane + 4% MeOH and 1.5% triethylamine) under N_2 atmosphere to give **L2** as a waxy pale yellow solid in 37% yield. ^{1}H NMR (300 MHz, $CDCl_3$) δ (ppm) = 8.61 – 8.55 (m, 4H), 7.49 – 7.32 (m, 5H), 7.15 (m, 4H); ^{31}P NMR (121 MHz, $CDCl_3$) δ (ppm) = -9.08; HRMS (CSI^+) calc. for [**L2**]$^+$ ($C_{16}H_{14}N_2P^+$) 265.0889, found 265.0907.

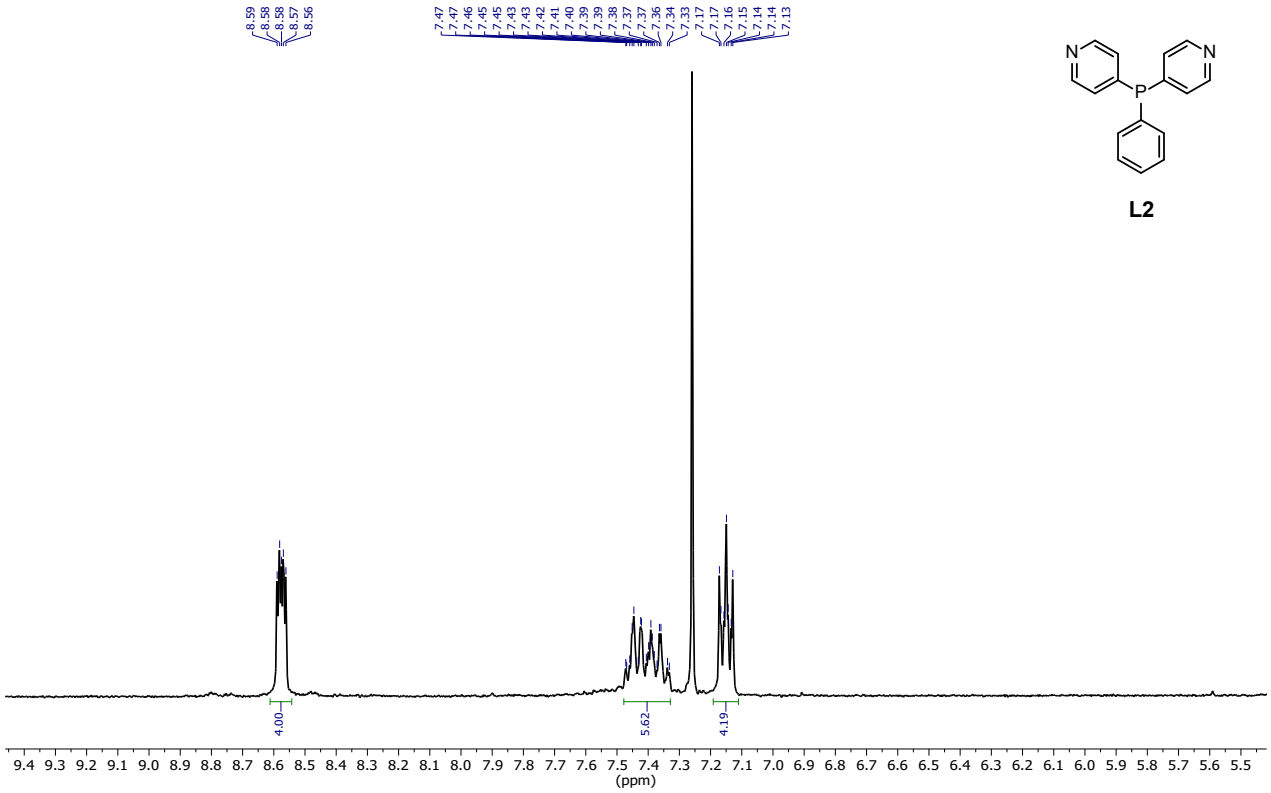

Figure S 3. ^{1}H NMR (300 MHz, 298 K) of **L2** in $CDCl_3$.

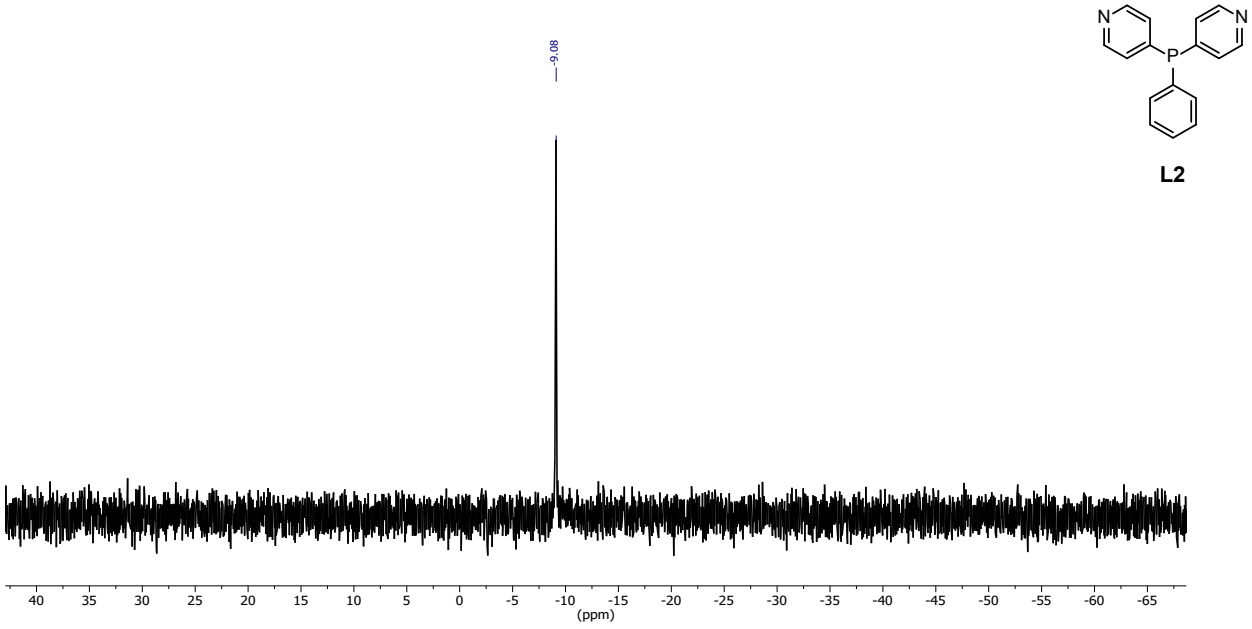

Figure S 4. ^{31}P NMR (121 MHz, 298 K) of **L2** in $CDCl_3$.

Tris(pyridin-4-yl)phosphane (L3):

n-BuLi (9.6 mL, 24 mmol, 2.5 M in hexanes) and freshly distilled and dried TMEDA (3.6 mL, 24 mmol) were transferred into a flame-dried Schlenk flask under N_2 atmosphere. The yellow solution was stirred at room temperature for 20 min, where after it was cooled to between -80 and -90°C using a pentane/liquid N_2 cooling bath. Next, pentane (25 mL), diethyl ether (25 mL) and tetrahydrofuran (25 mL) were added to the reaction mixture and the resulting solution was cooled to -115°C. Subsequently, a solution of **S1** (2.5 mL, 25.4 mmol) in diethyl ether (15 mL) was added dropwise over 15 min, while keeping the temperature at -115°C. 5 min later PCl_3 (0.6 mL, 7.2 mmol) was added dropwise, where after the resulting red-brown reaction mixture was heavily stirred for 1 h at -115°C and then 2 h at a temperature of -100 to -115°C, after which the reaction mixture was allowed to warm to room temperature slowly overnight. Next, the reaction mixture was quenched with degassed water resulting in the formation of a yellow-orange suspension. The suspension was extracted with degassed water (4 x 100 mL) and the combined aqueous layers were further extracted with chloroform (4 x 100 mL). The combined organic phases were dried over $MgSO_4$, filtered and the solvent was removed under reduced pressure to give a yellow-orange solid. The crude product was purified by column chromatography (silica, eluent: chloroform/hexane = 3:1 + 2% triethylamine) under N_2 atmosphere to give **L3** as a pale-yellow crystalline solid in 19% yield. ^{1}H NMR (300 MHz, $CDCl_3$) δ (ppm) = 8.64 (m, 2H), 7.21-7.13 (m, 2H); ^{31}P NMR (121 MHz, $CDCl_3$) δ (ppm) = -11.46.

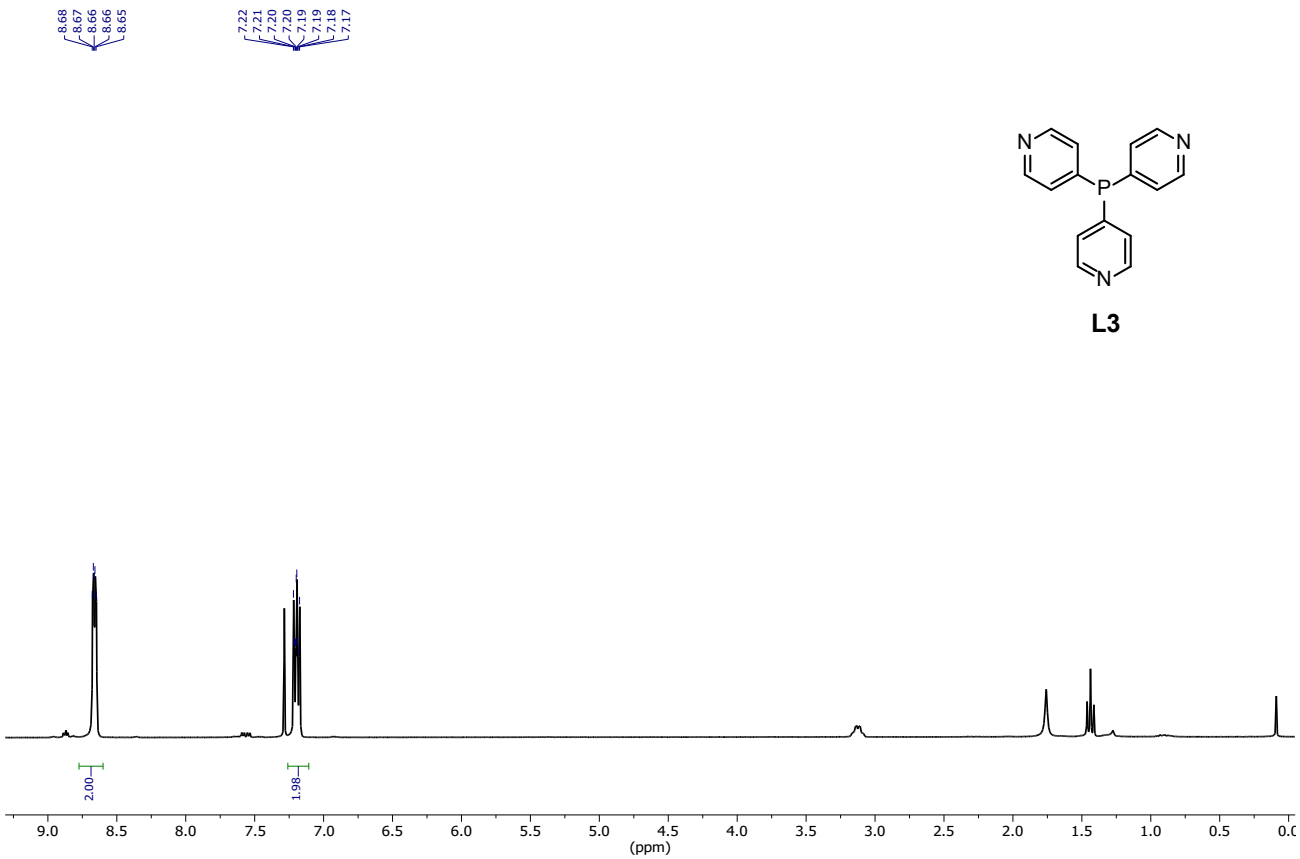

Figure S 5. ^{1}H NMR (300 MHz, 298 K) of **L3** in $CDCl_3$.

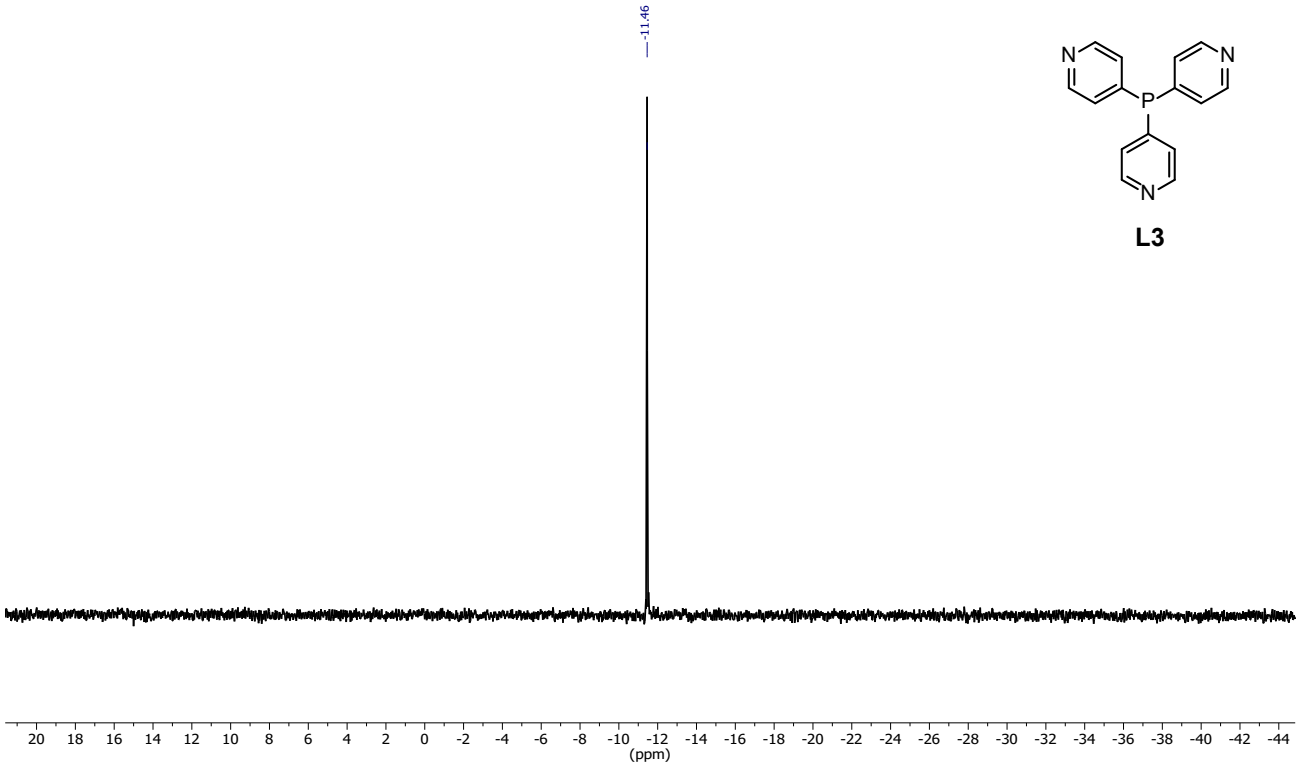

Figure S 6. ^{31}P NMR (121 MHz, 298 K) of **L3** in $CDCl_3$.

3. Synthesis and characterisation of Au1

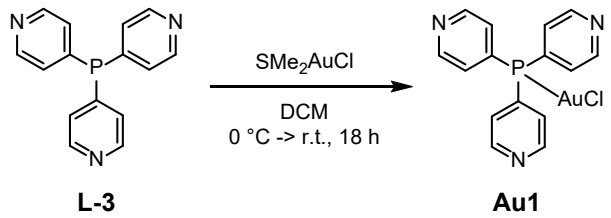

Au-L-3 was synthesised using a modified literature procedure[3]:

A solution of SMe_2AuCl (21.5 mg, 73 µmol) in dichloromethane (5 mL) under N_2 was cooled to 0°C, where after a solution of **L3** (19.5 mg, 73 µmol) in dichloromethane (5 mL) was added dropwise. The resulting yellow solution was allowed to come to room temperature and stirred for 18 h under N_2. Next, the solvent was removed under reduced pressure to give an off-white solid, which was further washed with pentane and cold ethanol to give **Au1** in 31% yield. Single crystals were grown by liquid-liquid diffusion of a toluene solution of **Au1** with pentane at 4°C. ^{1}H NMR (300 MHz, $CDCl_3$) δ (ppm) = 8.88 – 8.82 (m, 6H), 7.41 (ddd, *J* = 13.5, 4.4, 1.6 Hz, 6H). ^{31}P NMR (121 MHz, $CDCl_3$) δ (ppm) = 29.72. HRMS (CSI^+) calc. for [**Au1**]$^+$ ($C_{15}H_{13}N_3PAuCl^+$) 498.02011, found 498.02256.

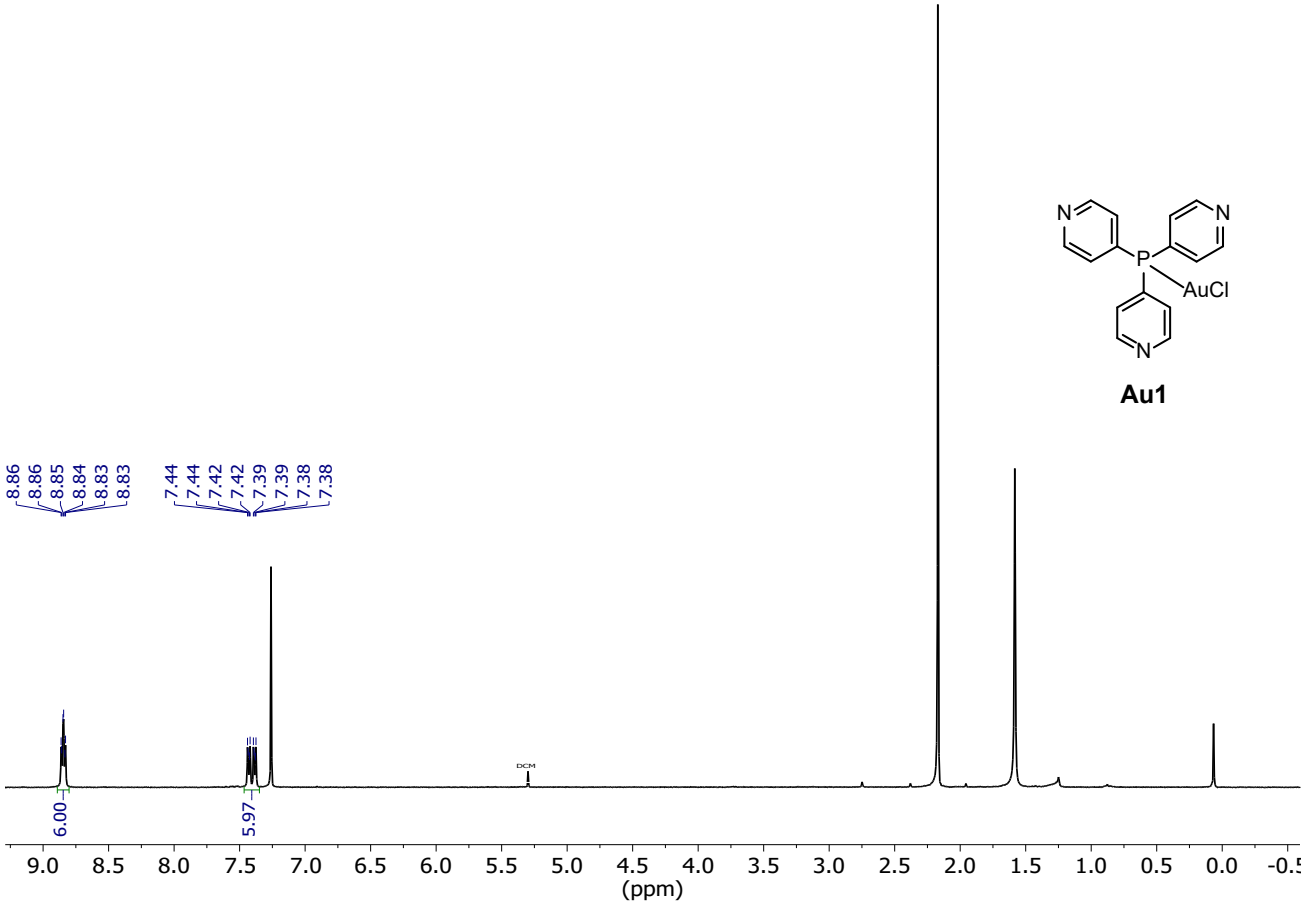

Figure S 7. ^{1}H NMR (300 MHz, 298 K) of **Au1** in $CDCl_3$.

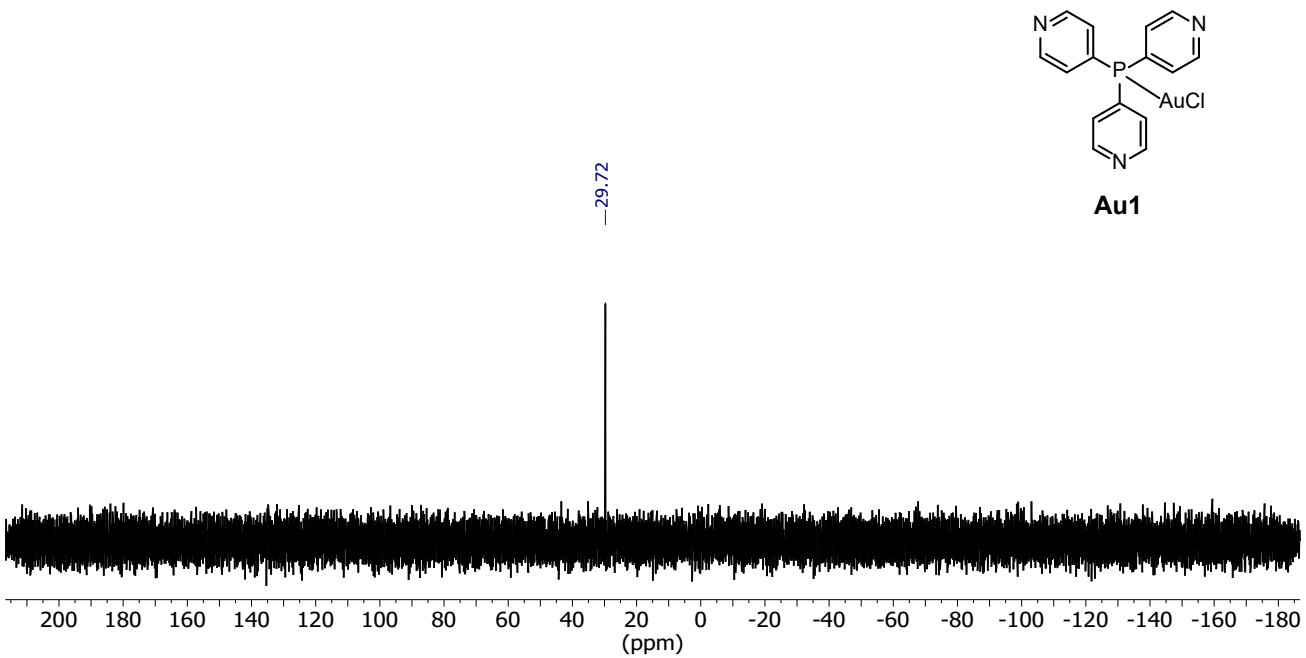

Figure S 8. ^{31}P NMR (121 MHz, 298 K) of **Au1** in $CDCl_3$.

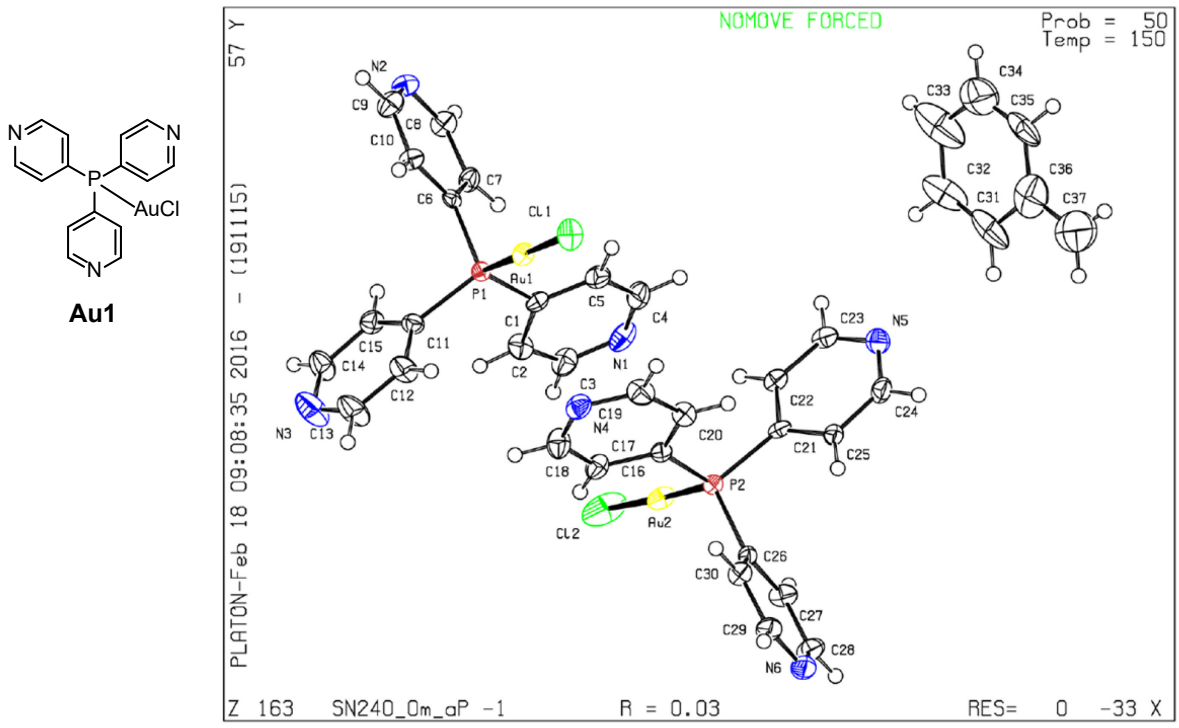

Figure S 9. X-ray crystal structure of complex **Au1** (CCDC number: 1819341). Thermal ellipsoids are drawn with 50% probability. Colour code: C, black and white; H, white; N, blue; P, red; Au, yellow; Cl, green.

4. Synthesis and characterisation of building block Zn-P

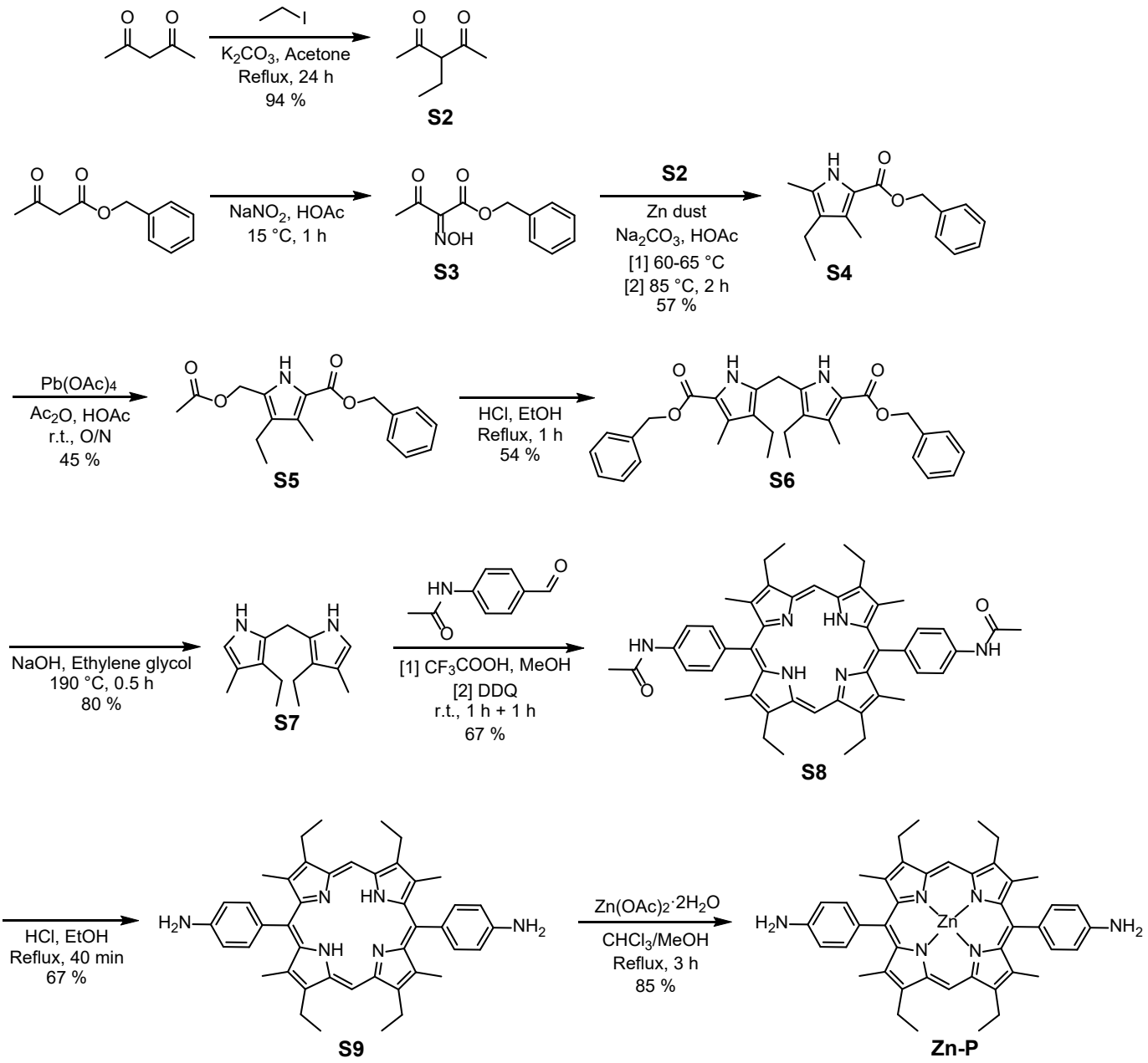

S2-S6 were synthesised using a literature procedure[4], **S7-S9 and Zn-P** were synthesised using modified literature procedures[5,6]:

Bis(3-ethyl-4-methyl-1H-pyrrol-2-yl)methane (S7):

S6 (2.0 g, 5.3 mmol) and NaOH (0.85 g, 21.3 mmol) were transferred along with degassed ethylene glycol (20 mL) in a round-bottom Schlenk flask under an atmosphere of a N_2. The suspension was heated to 190°C for 30 minutes resulting in the formation of a tan solid at the bottom of the flask. Subsequently, the flask was immediately cooled on an ice bath, after which water was added to the flask in air to make the ethylene glycol less viscous. The suspension was extracted with dichloromethane (4 x 100 mL), dried with $MgSO_4$, filtered and the solvent was removed under reduced pressure to yield a dark brown-red oil. The crude product was purified by column chromatography (silica, eluent: dichloromethane) to give **S7**

as a pale solid in 80% yield. ^{1}H NMR (300 MHz, $CDCl_3$) δ (ppm) = 7.35 (s, 2H), 6.43 – 6.30 (m, 2H), 3.83 (s, 2H), 2.46 (q, *J* = 7.5 Hz, 4H), 2.07 (s, 6H), 1.12 (t, *J* = 7.5 Hz, 6H).

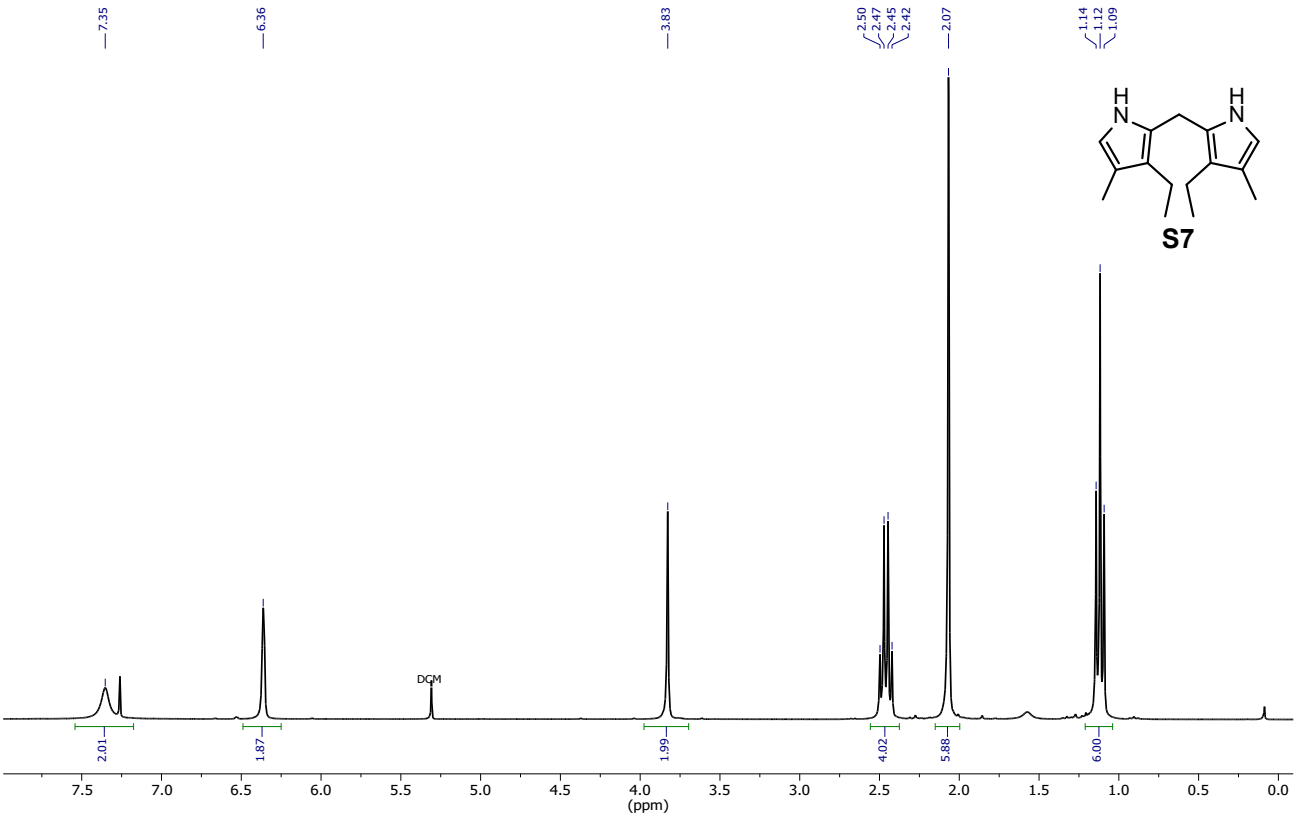

Figure S 10. ^{1}H NMR (300 MHz, 298 K) of **S7** in $CDCl_3$.

N,N'-((2,8,12,18-tetraethyl-3,7,13,17-tetramethylporphyrin-5,15-diyl)bis(4,1-phenylene)) diacetamide (S8):

S7 (0.25 g, 1.1 mmol) and 4-acetamidobenzaldehyde (0.18 g, 1.1 mmol) were transferred along with dry and degassed methanol (100 mL) into a two-necked Schlenk flask under an atmosphere of N_2. Next, trifluoroacetic acid (10.1 µL, 0.1 mmol) was added and the reaction mixture was stirred at room temperature covered in foil for 1 h, followed by the addition of DDQ (0.37 g, 1.6 mmol). The resulting black solution was further stirred in air at room temperature covered in foil to complete the oxidation of the porphyrinogen. Subsequently, chloroform (100 mL) and triethylamine (1 mL) were added. Most of the polypyrrole by-product was removed with a short plug of silica eluting with a 9:1 mixture of chloroform and methanol. The resulting crude solid was purified with column chromatography (silica, eluent: chloroform/tetrahydrofuran = 8:2) to give **S8** as a purple solid in 67% yield. ^{1}H NMR (300 MHz, THF-d_8) δ (ppm) = 10.22 (s, 2H), 9.64 (s, 1H), 8.09 (d, *J* = 8.3 Hz, 2H), 7.93 (d, *J* = 8.4 Hz, 1H), 4.05 (q, *J* = 7.5 Hz, 4H), 2.58 (s, 6H), 2.22 (s, 3H), 1.78 (t, *J* = 7.6 Hz, 6H), -2.29 (s, 1H).

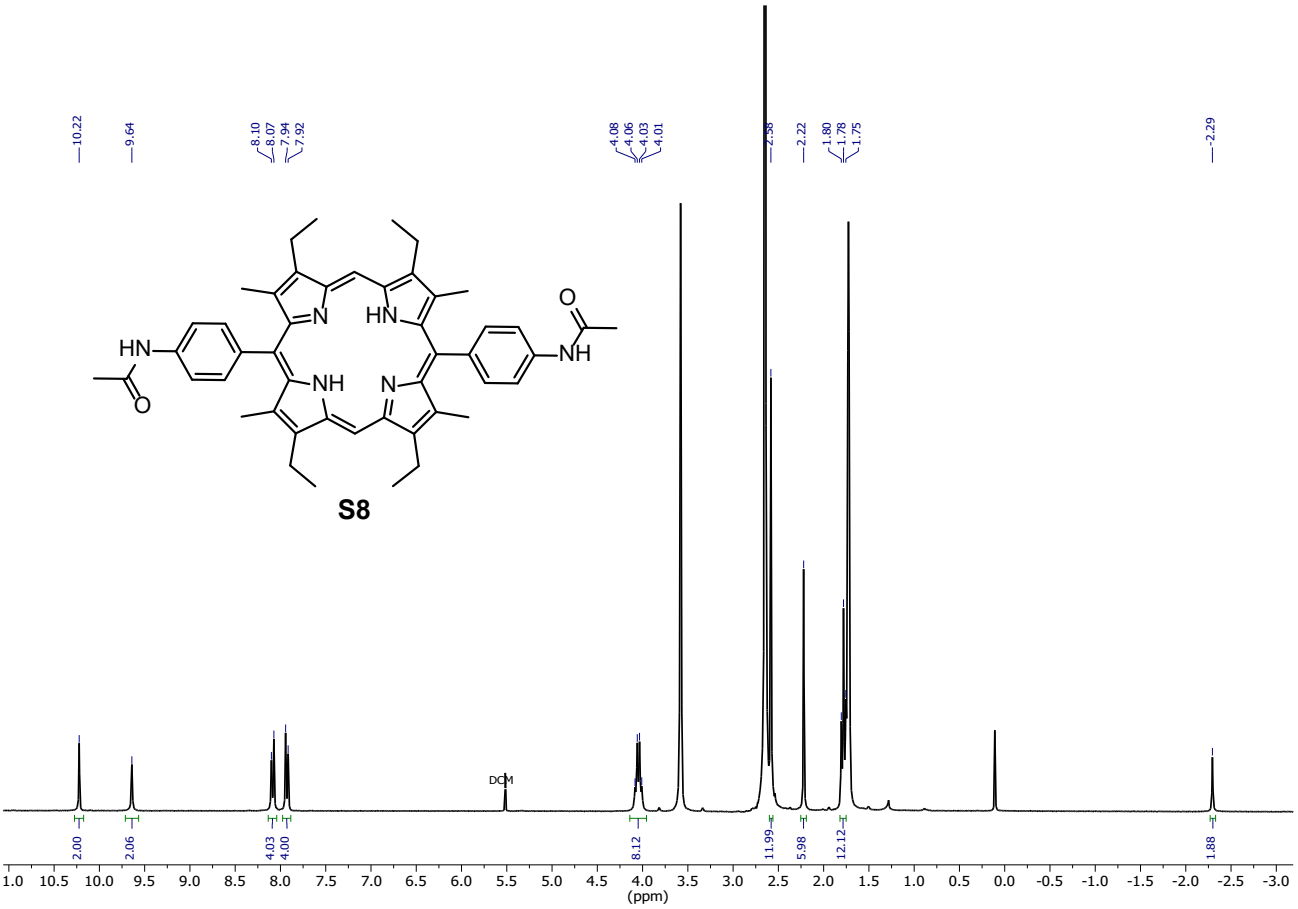

Figure S 11. ^{1}H NMR (300 MHz, 298 K) of **S8** in THF-d_8.

4,4'-(2,8,12,18-tetraethyl-3,7,13,17-tetramethylporphyrin-5,15-diyl)dianiline (S9):

S8 (0.5 g, 0.67 mmol), conc. HCl (20.7 mL) and EtOH (31 mL) were transferred to a round-bottom flask. The resulting green solution was heated at reflux for 40 minutes, after which it was cooled in an ice bath. Next, the solution was neutralised with sat. Na_2CO_3 (aq) precipitating a purple solid. The residual ethanol was removed under reduced pressure, where after filtration gave pure **S9** as a purple solid in 67% yield. ^{1}H NMR (300 MHz, CD_2Cl_2) δ (ppm) = 10.23 (s, 2H), 7.77 (d, *J* = 8.2 Hz, 4H), 7.08 (d, *J* = 8.2 Hz, 4H), 4.24 – 3.98 (m, 12H), 2.64 (s, 12H), 1.79 (t, *J* = 7.5 Hz, 12H), -2.54 (s, 2H).

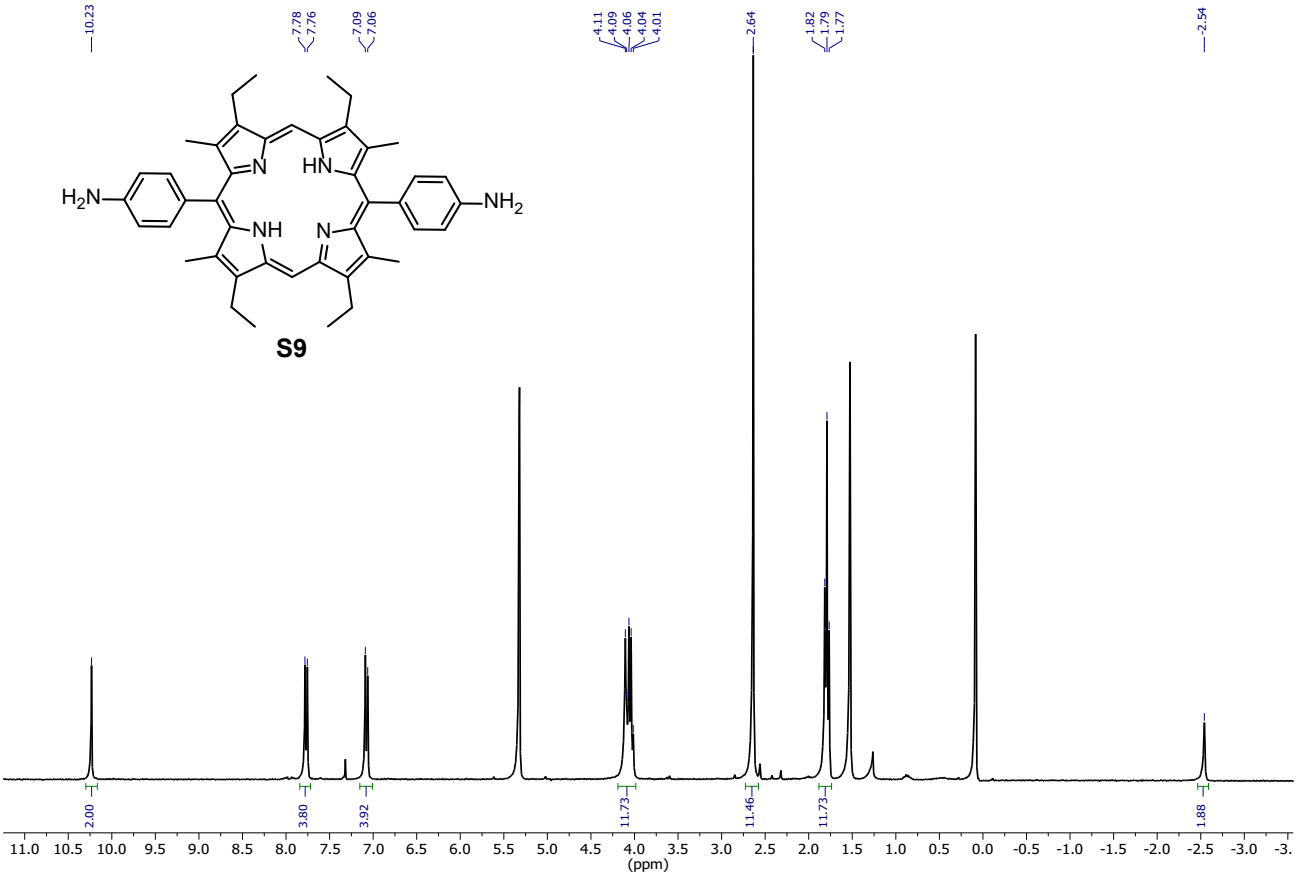

Figure S 12. ^{1}H NMR (300 MHz, 298 K) of **S9** in CD_2Cl_2.

4,4'-(2,8,12,18-tetraethyl-3,7,13,17-tetramethylporphyrin-5,15-diyl)dianiline zinc(II) (Zn-P):

S9 (0.3 g, 0.45 mmol) and $Zn(OAc)_2{\cdot}H_2O$ (0.5 g, 2.26 mmol) were transferred into a round-bottom flask along with chloroform (90 mL) and methanol (24 mL). The purple-pink solution was heated to reflux for 3 h, where after it was cooled down to room temperature, washed with saturated Na_2CO_3 (aq) and water. The resulting crude purple solid was purified with column chromatography (silica, eluent: chloroform, short column like a plug) to give **Zn-P** as a bright purple solid in 85% yield. ^{1}H NMR (300 MHz, CD_2Cl_2) δ (ppm) = 10.18 (s, 2H), 7.75 (d, *J* = 8.1 Hz, 4H), 7.03 (d, *J* = 8.2 Hz, 4H), 5.33 (s, 4H), 4.03 (q, *J* = 7.8 Hz, 8H), 2.60 (s, 12H), 1.78 (t, *J* = 7.6 Hz, 12H).

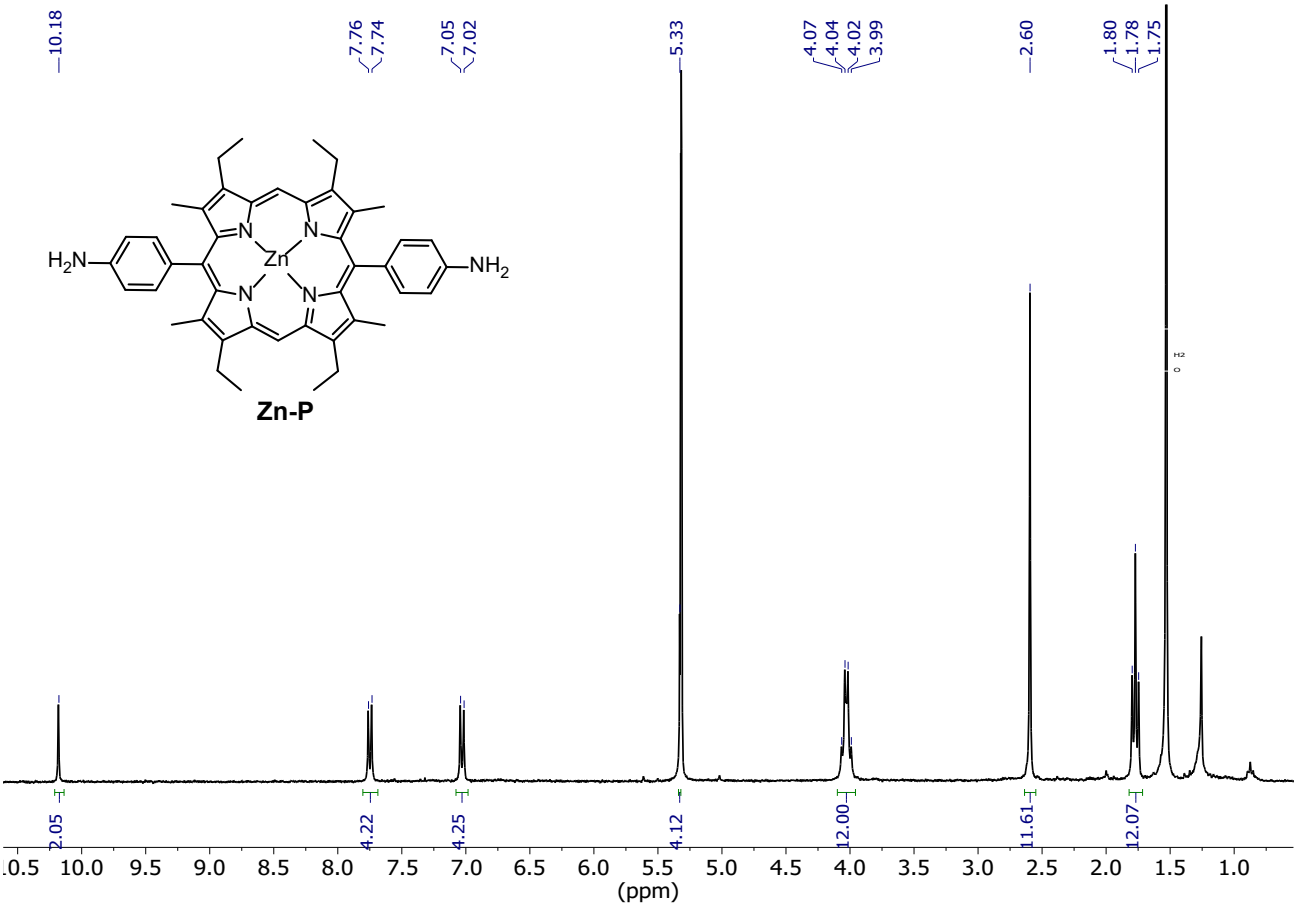

Figure S 13. ^{1}H NMR (300 MHz, 298 K) of **Zn-P** in CD_2Cl_2.

5. Synthesis and characterisation of $Fe_4(Zn\text{-}L)_6$

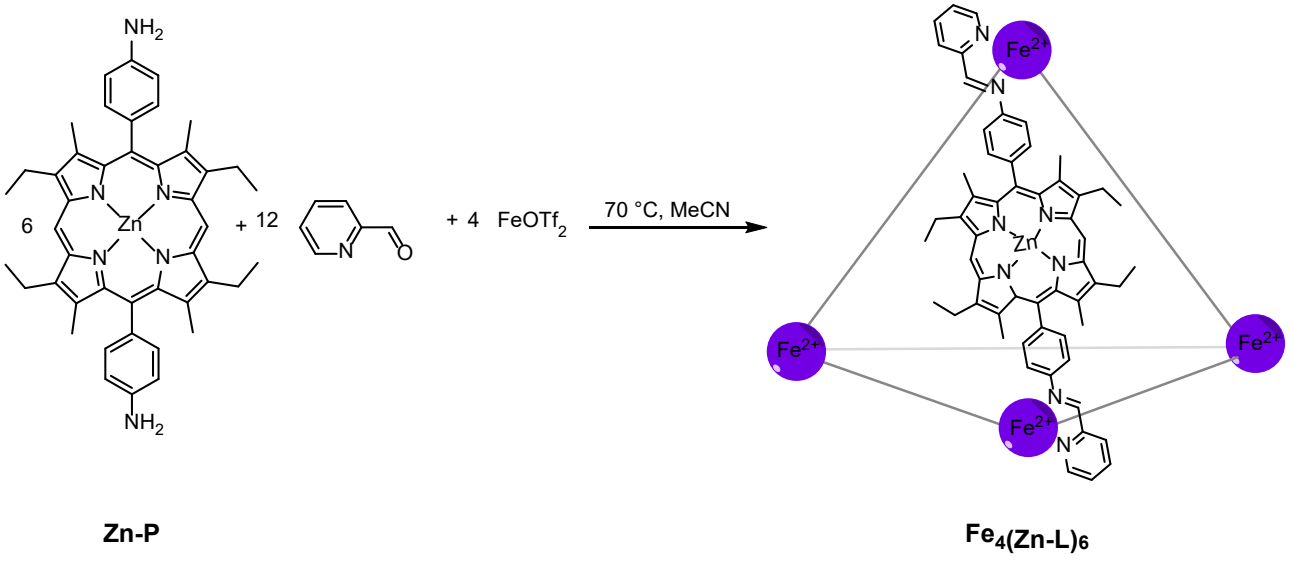

Zn-P $Fe_4(Zn\text{-}L)_6$

Zn-P (68.7 mg, 94.7 µmol), 2-formylpyridine (18.6 µL, 195.6 µmol) and $Fe(OTf)_2$ (22 mg, 62.1 µmol) were transferred along with acetonitrile (8.5 mL) into a Schlenk flask under an atmosphere of N_2. The dark purple suspension was sonicated and then heated at 70°C for 4 h to complete the cage formation.

Subsequently, the resulting dark purple solution was cooled down to room temperature and added dropwise into diethyl ether (10 mL) to give rise to a purple suspension. The solid was recovered by centrifugation, where after it was further washed with diethyl ether (2 x 4 mL). The residual diethyl ether was removed to give pure **Fe_4(Zn-L)$_6$** as a purple, microcrystalline solid in 93% yield. ^{1}H NMR (300 MHz, CD_3CN) δ (ppm) = 10.03 – 9.81 (m, 1H), 9.70 (bs, 0.5H), 9.59 (m, 0.5H), 8.84 (m, 1H), 8.58 (m, 1H), 8.14 – 7.89 (m, 2H), 7.79 (bs, 2H), 6.83 (bs, 2H), 3.92 (bs, 4H), 2.52 – 2.36 (m, 6H), 1.55 (t, *J* = 7.7 Hz, 6H); ^{13}C NMR (126 MHz, CD_3CN) δ (ppm) = 176.08, 175.78, 159.73, 159.62, 157.36, 152.23, 147.73, 146.43, 146.02, 145.72, 141.05, 137.79, 137.76, 135.20, 132.52, 131.84, 122.04, 97.87, 20.30, 18.03, 16.58.; *m/z* (ESI$^+$) = 704.61 $[Fe_4(Zn\text{-}L)_6]^{8+}$, 813.75 [Zn-L - 1 pyridine]$^+$, 900.52 [Zn-L]$^+$, 989.55 $[Fe_4(Zn\text{-}L)_6]^{6+}$, 1217.03 $[Fe_4L_6]^{5+}$; Elemental analysis calc. (%) for $C_{344}H_{312}F_{24}Fe_4N_{48}O_{24}S_8Zn_6$ x $12H_2O$ = calc. C 58.63, H 4.81, N 9.54, found: C 58.50, H 4.64, N 9.52; DOSY NMR (CD_3CN, 298 K): logD = -9.41, $r_h \approx 1.6$ nm.

Stokes-Einstein Equation for the estimation of sphere hydrodynamic radius:

$D = \frac{kT}{6\pi\eta R}$ T = 298 K; k = 1.38 x 10^{-23} N m K^{-1}; η = 3.57 x 10^{-4} N s m^{-2}[7]

$r_h = (k * T) / (6 * \pi * \eta * D)$

For **Fe_4(Zn-L)$_6$**, D = $10^{-9.41}$ m^2 s^{-1}, $r_h \approx 1.6$ nm

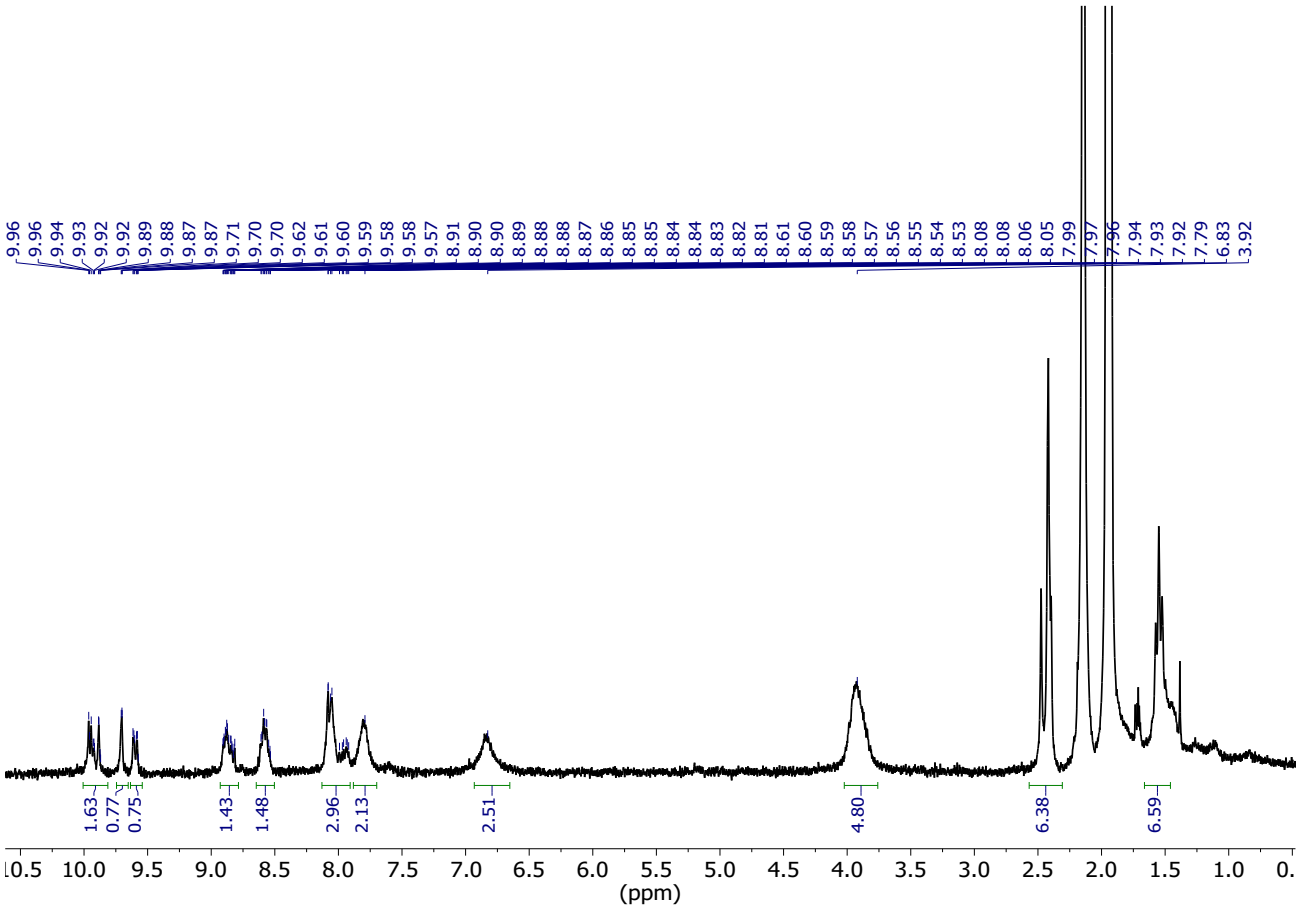

Figure S 14. ^{1}H NMR (300 MHz, 298 K) of **Fe_4(Zn-L)$_6$** in CD_3CN.

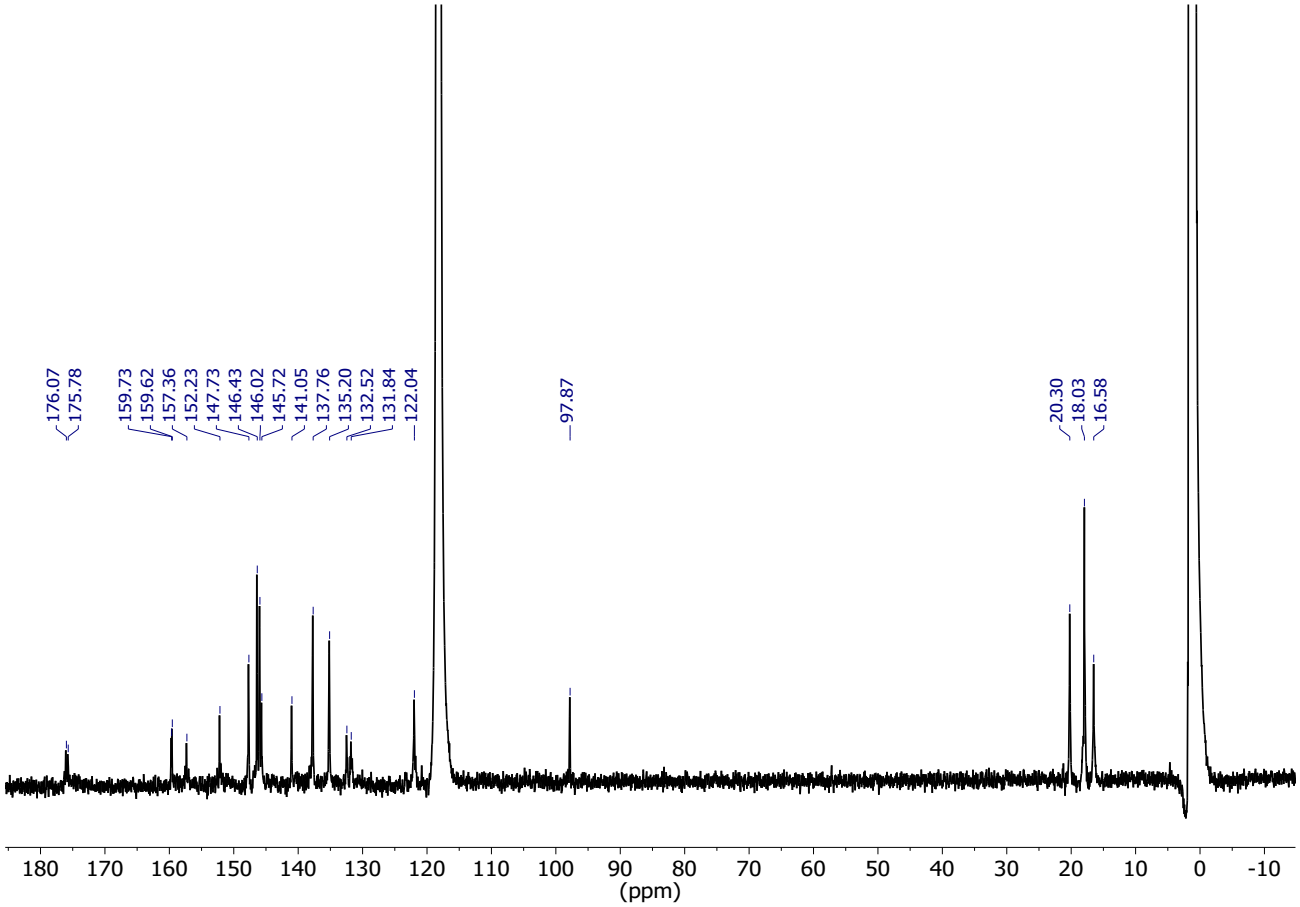

Figure S 15. ^{13}C NMR (126 MHz, 298 K) of **Fe_4(Zn-L)$_6$** in CD_3CN.

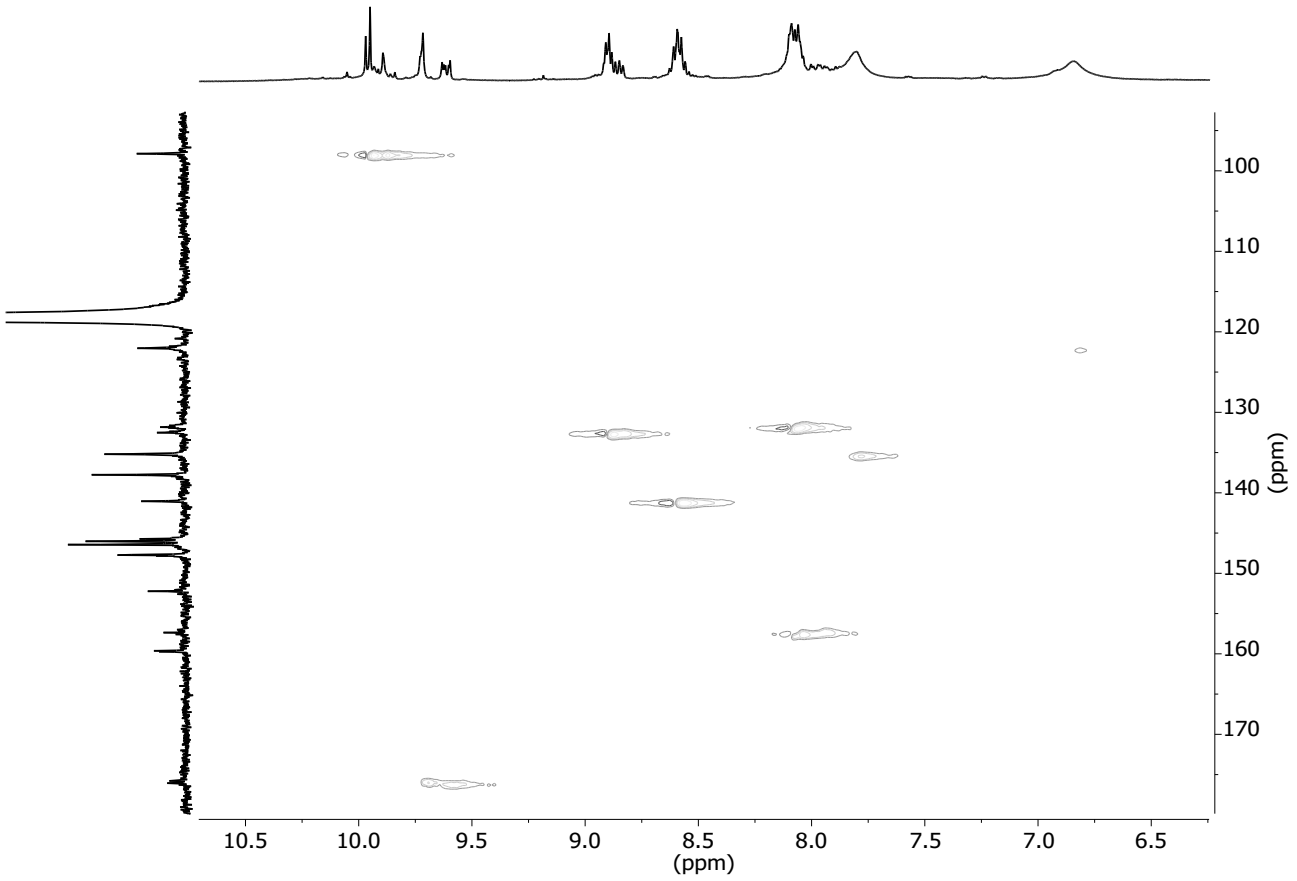

Figure S 16. Aromatic region of the HSQC (126 MHz, 298 K) spectrum of **Fe_4(Zn-L)$_6$** in CD_3CN.

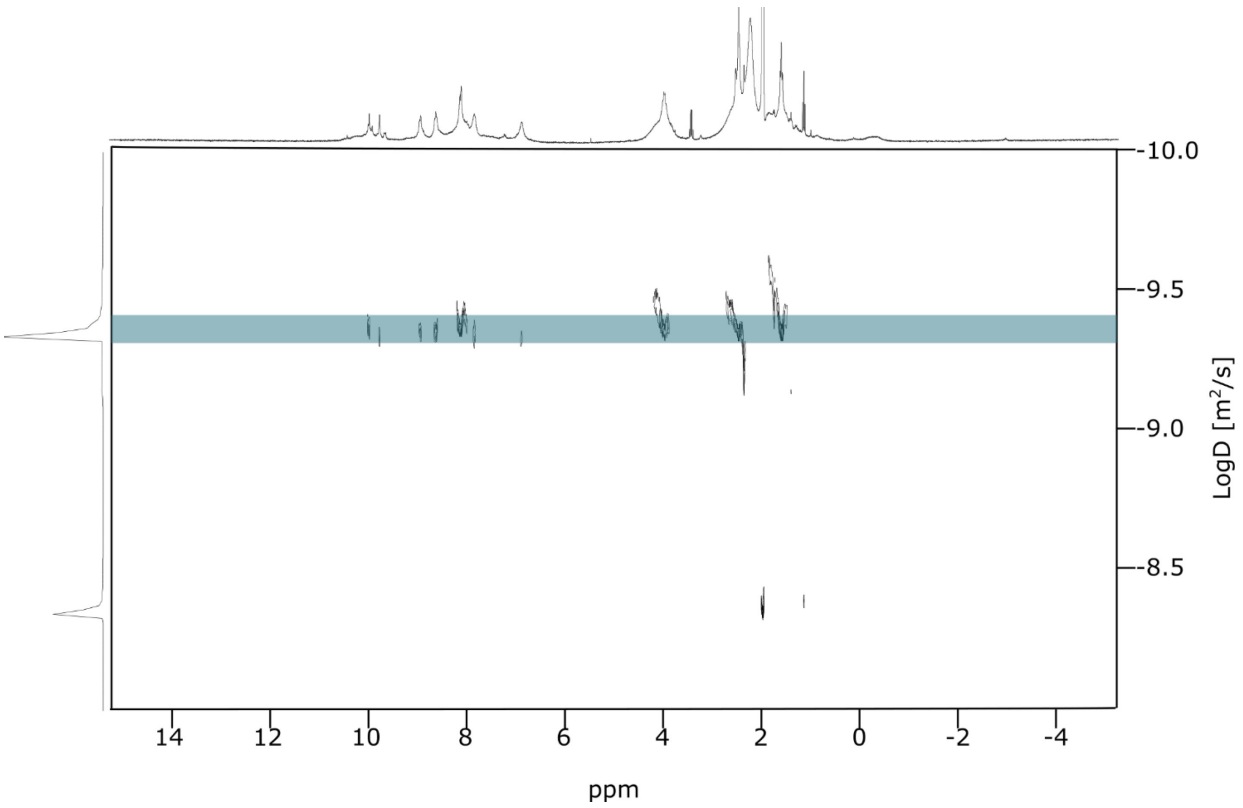

Figure S 17. 2D ^{1}H DOSY (298 K) of **Fe_4(Zn-L)$_6$** in CD_3CN.

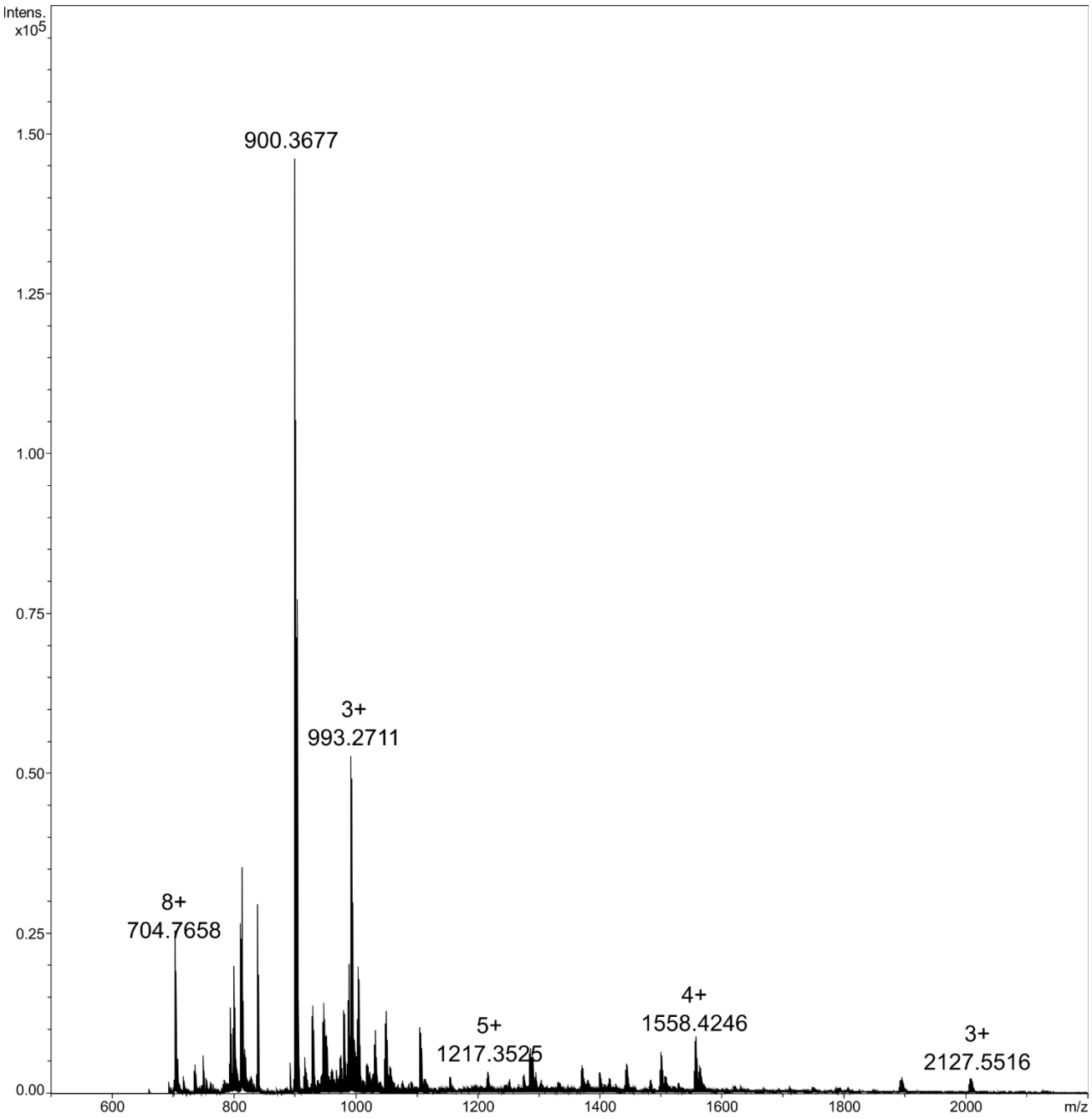

Figure S 18. CSI mass spectrum (full spectrum) of the sphere **Fe_4(Zn-L)$_6$** with a spray temperature of -40 °C and a dry gas temperature of -35 °C. The peak with m/z ratio of 900.3677 belongs to a single ligand of the cage.

Table S 1. Different charged species observed in the CSI mass spectrum of the sphere **$Fe_4(Zn\text{-}L)_6$** and the corresponding found and calculated [m/z].

Species	Charge	Found [m/z]	Calculated [m/z]
$Fe_4(Zn\text{-}L)_6(OTf)_0$	8+	704.7655	704.7376
$Fe_4(Zn\text{-}L)_6(OTf)_1$	7+	826.7179	826.6934
$Fe_4(Zn\text{-}L)_6(OTf)_2$	6+	989.3071	989.3010
$Fe_4(Zn\text{-}L)_6(OTf)_3$	5+	1216.9523	1216.9517
$Fe_4(Zn\text{-}L)_6(OTf)_4$	4+	1558.4243	1558.4278
$Fe_4(Zn\text{-}L)_6(OTf)_5$	3+	2127.5516	2127.5546

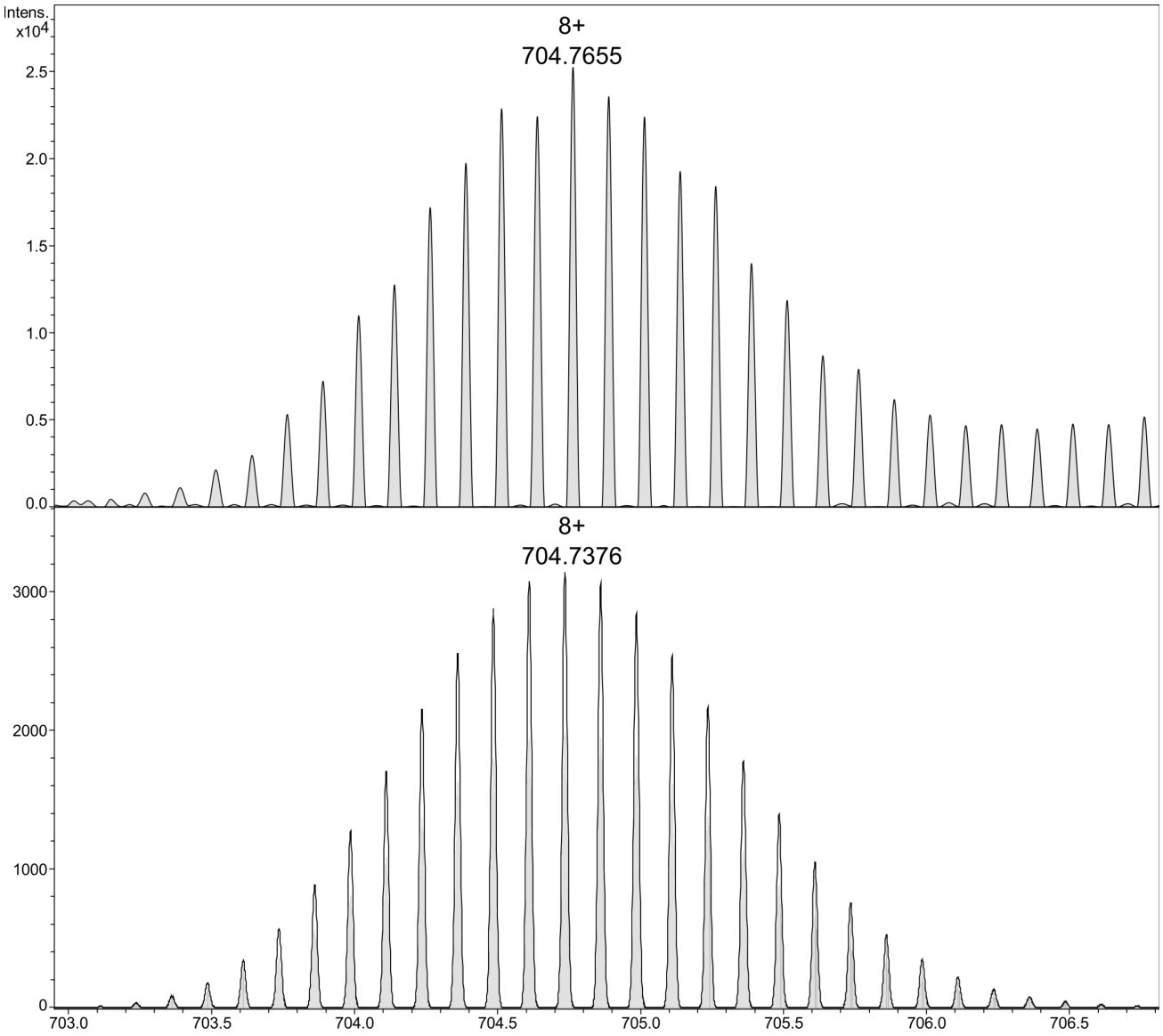

Figure S 19. Expanded spectrum for the charged species $[Fe_4(Zn\text{-}L)_6(OTf)_0]^{8+}$ observed (above) in the CSI mass spectrum of the sphere **$Fe_4(Zn\text{-}L)_6$** and simulated isotopic distribution (below).

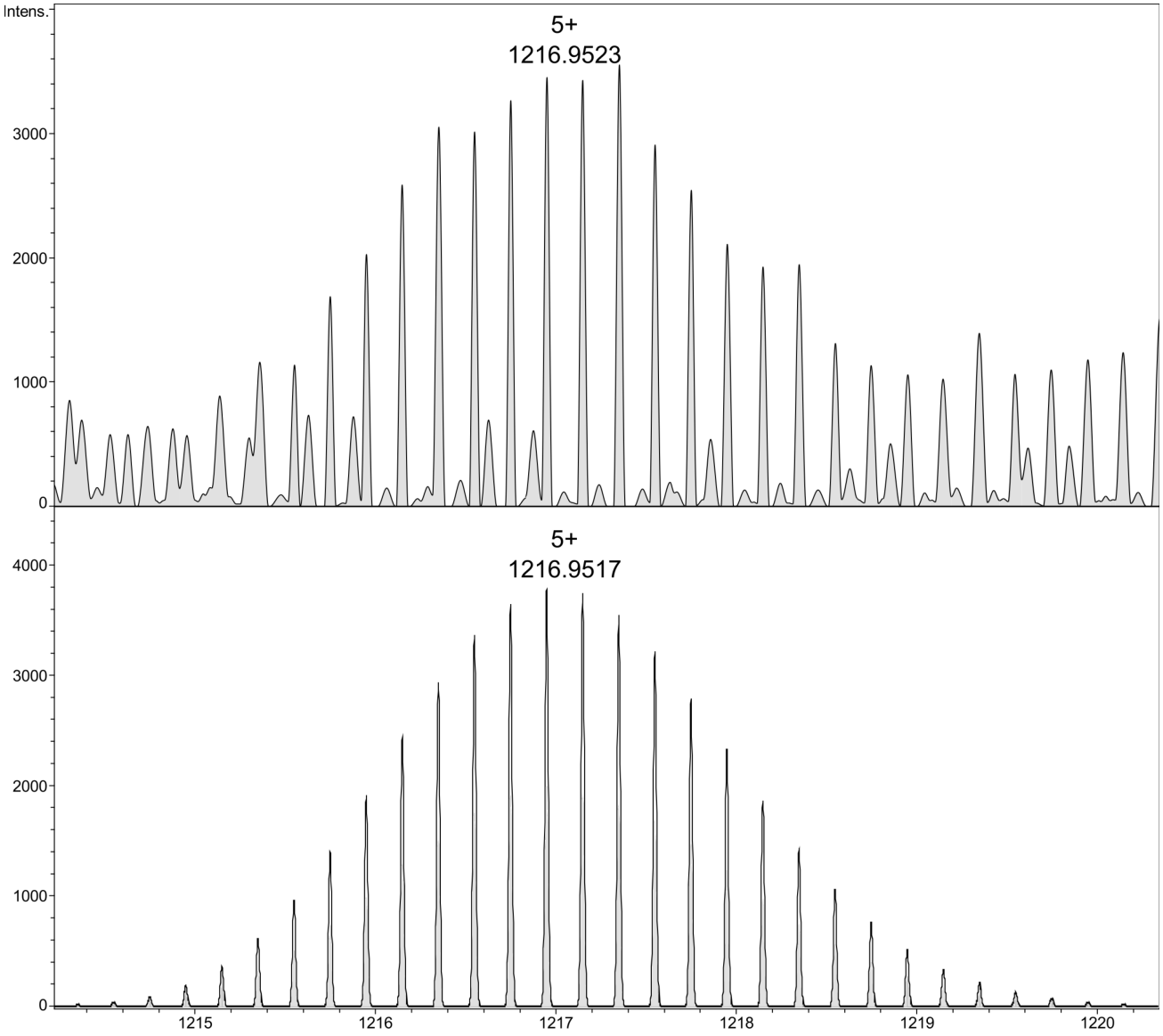

Figure S 20. Expanded spectrum for the charged species $[Fe_4(Zn\text{-}L)_6(OTf)_3]^{5+}$ observed (above) in the CSI mass spectrum of the sphere **Fe_4(Zn-L)$_6$** and simulated isotopic distribution (below).

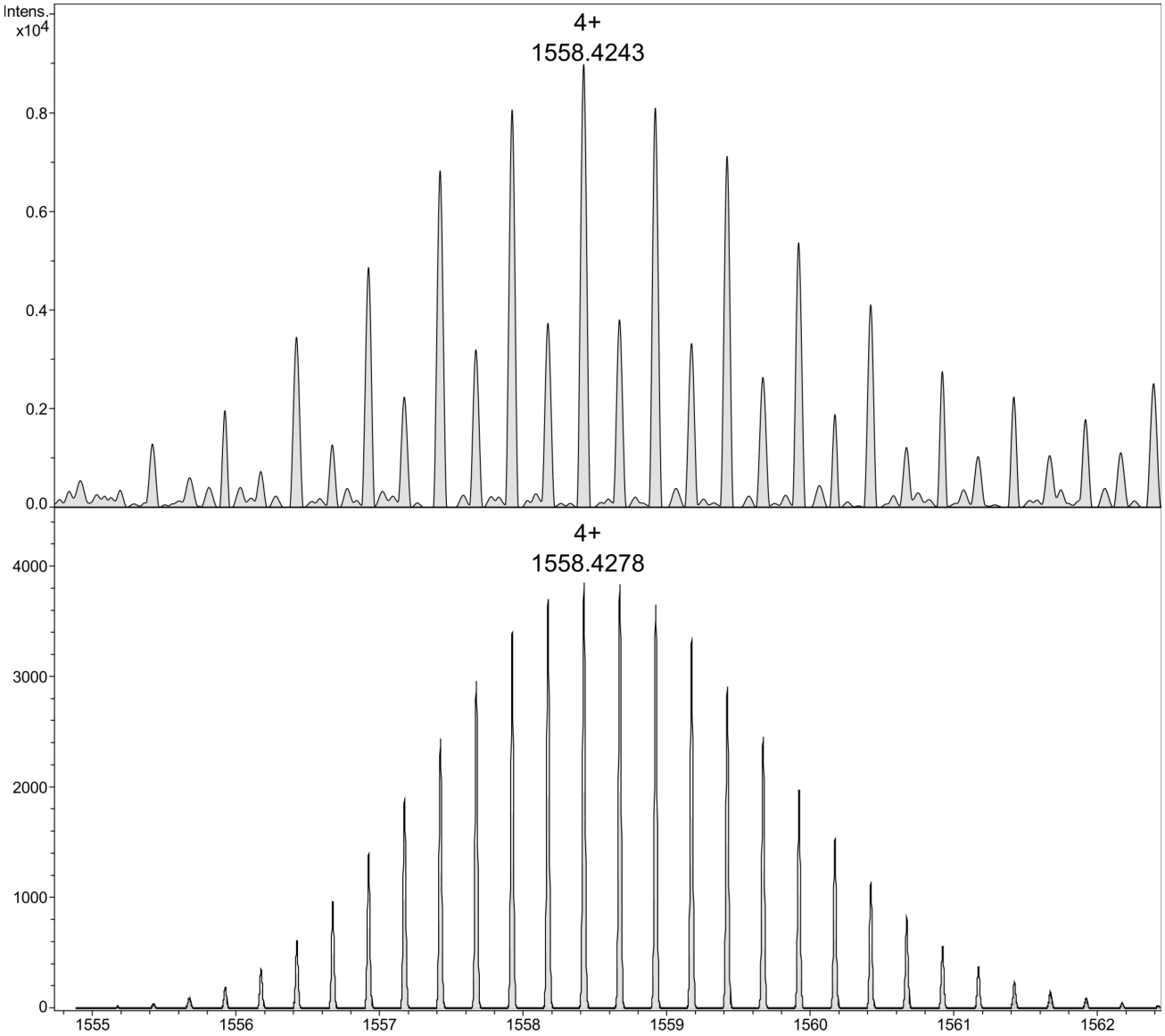

Figure S 21. Expanded spectrum for the charged species $[Fe_4(Zn\text{-}L)_6(OTf)_4]^{4+}$ observed (above) in the CSI mass spectrum of the sphere **$Fe_4(Zn\text{-}L)_6$** and simulated isotopic distribution (below). The difference in intensity between the peaks in the experimental spectrum are due to a symmetrical fragmentation of the cage in two.

6. Synthesis and characterisation of substrate Sub1

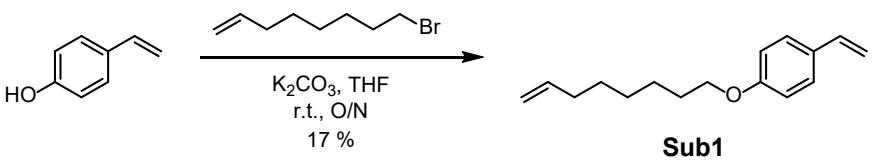

Sub1

K_2CO_3 (0.53 g, 3.8 mmol) was transferred into a flame-dried schlenk flask under N_2. Dry tetrahydrofuran (100 mL) along with 4-vinylphenol (2.58 mL, 2.23 mmol, 10% solution in propylene glycol) were added. The solution was allowed to stir at room temperature for 30 min, where after 8-bromo-1-octene (0.45 mL, 2.68 mmol) was added dropwise and the solution was further stirred overnight. The next day the

solvent was removed under vacuum and the yellow residue was dissolved in dichloromethane and the undissolved salts were removed by filtration. The solvent was removed and the resulting crude yellow oil was purified with column chromatography (silica, eluent: dichloromethane/hexane = 1:2) to give **Sub1** as a pale yellow oil in 17% yield. ^{1}H NMR (400 MHz, CD_2Cl_2) δ (ppm) = 7.33 (d, *J* = 8.7 Hz, 2H), 6.84 (d, *J* = 8.7 Hz, 2H), 6.66 (dd, *J* = 17.6 Hz, 10.9 Hz, 1H), 5.90 – 5.76 (m, 1H), 5.60 (dd, *J* = 17.6 Hz, 1.1 Hz, 1H), 5.10 (dd, *J*= 10.9 Hz, 1.0 Hz, 1H), 5.04 – 4.89 (m, 2H), 3.95 (t, *J* = 6.6 Hz, 2H), 2.05 (t, *J* = 7.1 Hz, 2H), 1.82 – 1.70 (m, 3H), 1.51 – 1.30 (m, 6H).

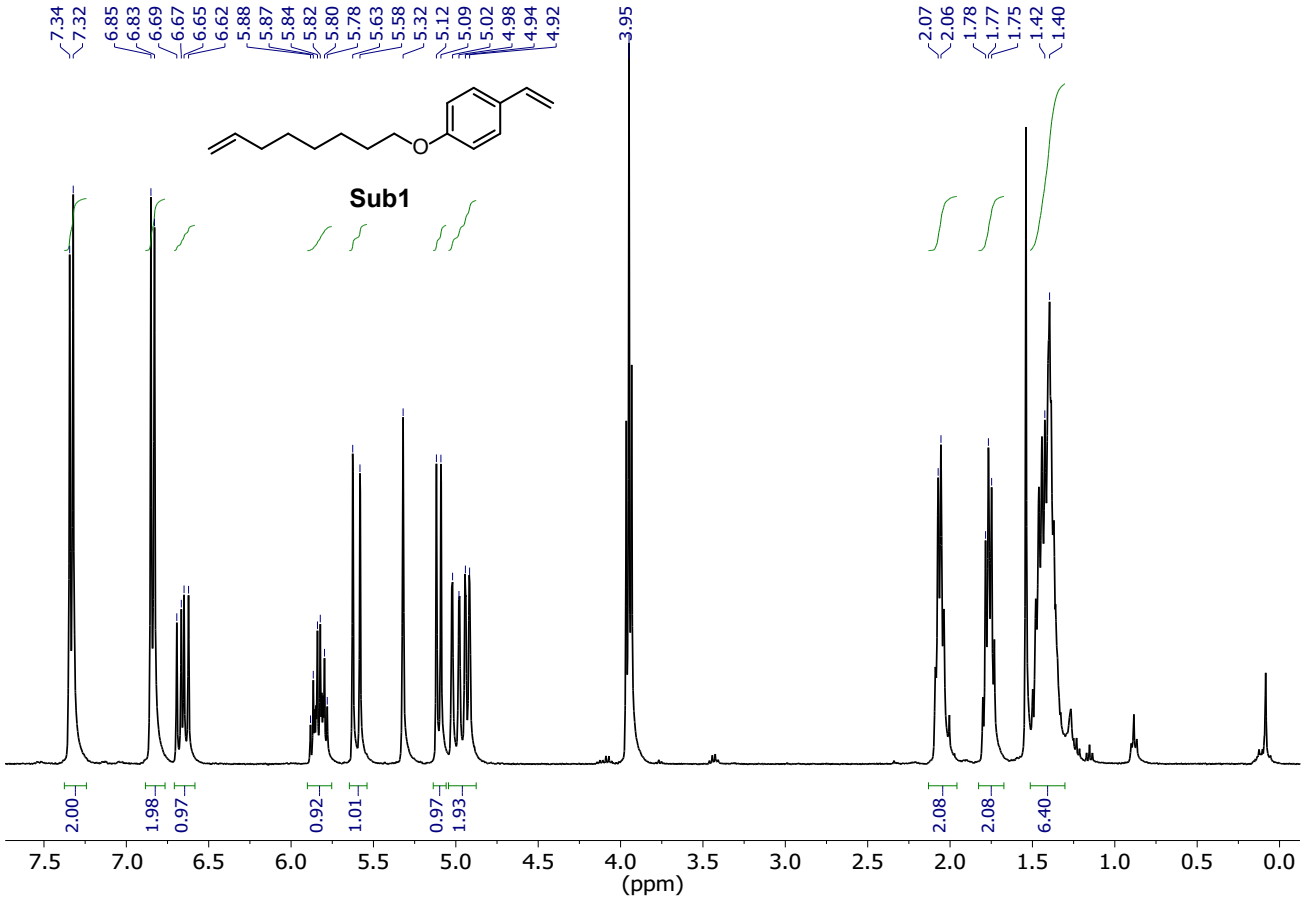

Figure S 22. ^{1}H NMR (400 MHz, 298 K) of **Sub1** in CD_2Cl_2.

7. Binding studies of $Fe_4(Zn\text{-}L)_6$ with various guests

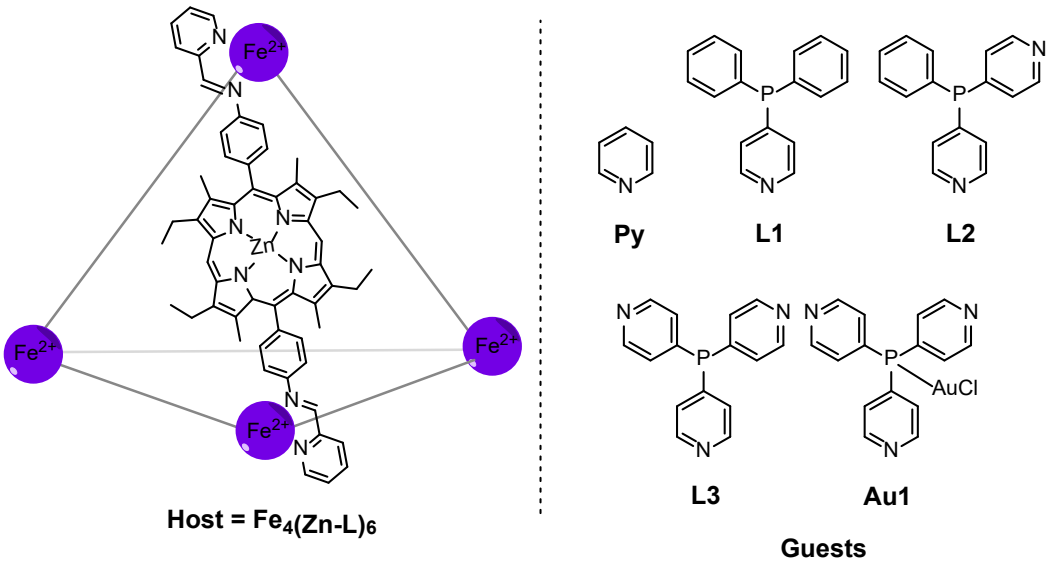

The binding affinities of **$Fe_4(Zn\text{-}L)_6$** towards **Py**, **L1**, **L2**, **L3** and **Au1** were obtained by UV-vis titrations in acetonitrile. A solution of **$Fe_4(Zn\text{-}L)_6$** in acetonitrile (solution **A**), and stock solutions of each guest containing the same concentration of host in acetonitrile (solution **B**) were prepared respectively. Aliquots of each guest from stock solution **B** were added to a quartz cuvette containing the solution **A**. Each titration was performed at 298 K. The progress of the titration was monitored by the shifts in the Q-bands of **$Fe_4(Zn\text{-}L)_6$**. The general titration fitting procedure is described in Section 6.

Uv-vis binding study of $Fe_4(Zn\text{-}L)_6$ and Py:

Table S 2. Fitting results for the 1:1 host-guest system between **$Fe_4(Zn\text{-}L)_6$** and **Py** in acetonitrile for K = 1.19 x 10^3 M^{-1} at 298 K.

Wavelength [nm]	ε_{HG} / 10^4	R^2
544	1.75	0.91
550	1.92	0.94
578	0.69	0.93

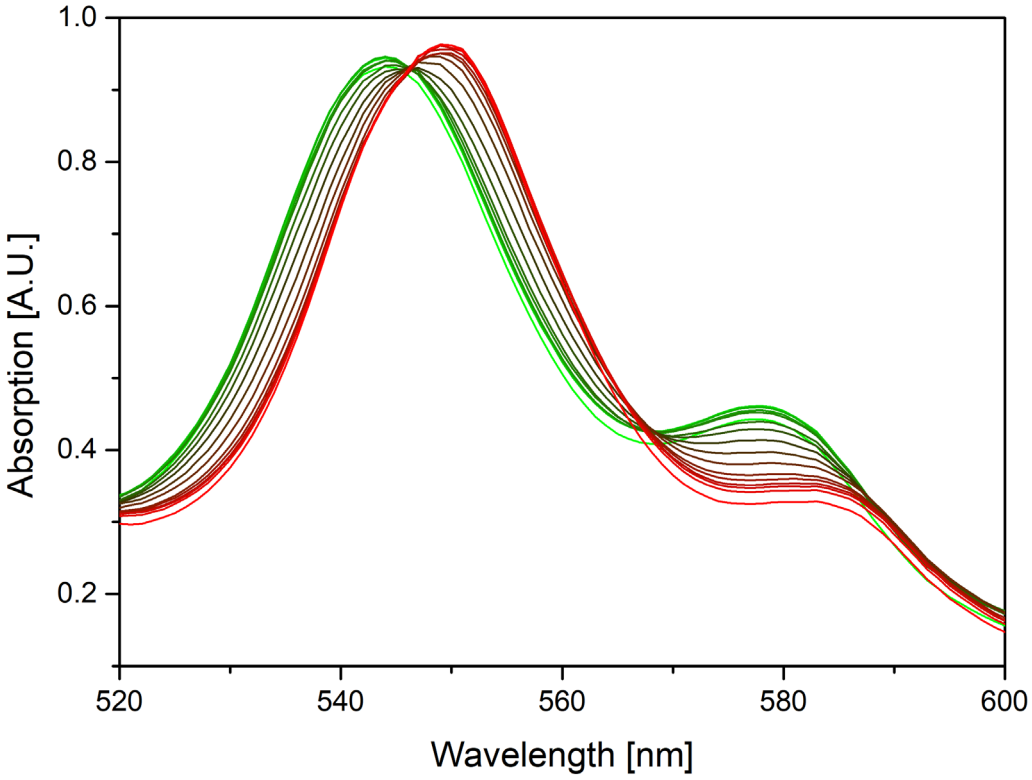

Figure S 23. Overlay of UV-vis spectra of the titration of **Fe_4(Zn-L)$_6$** (host) with **Py** (guest), at a fixed host concentration of 8.4 µM in acetonitrile at 298 K.

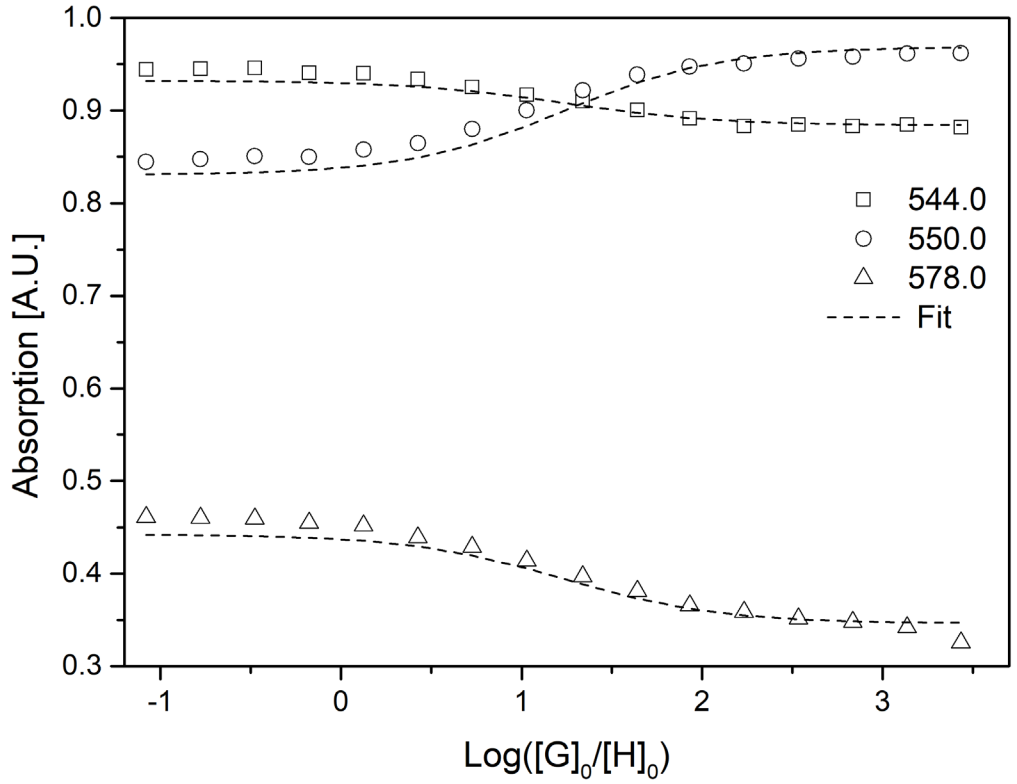

Figure S 24. Fitted UV-vis titration curves of **Fe_4(Zn-L)$_6$** with **Py** in acetonitrile (298 K).

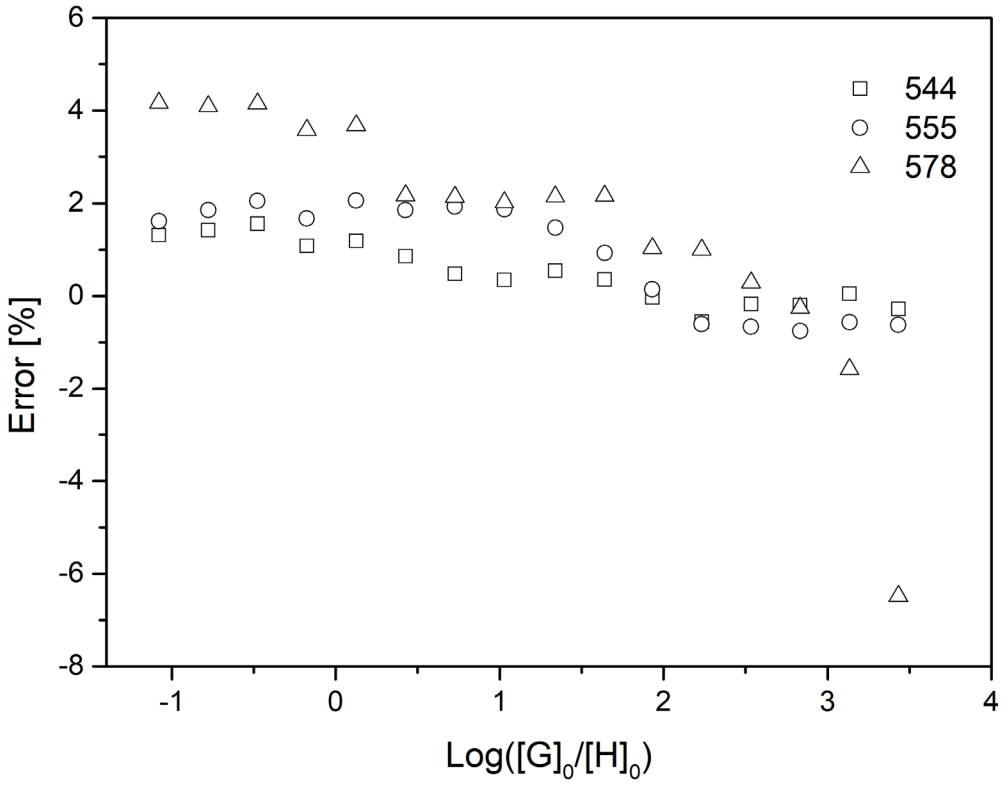

Figure S 25. The error distribution for the fitted curves of **Fe_4(Zn-L)$_6$** with **Py** in acetonitrile (298 K).

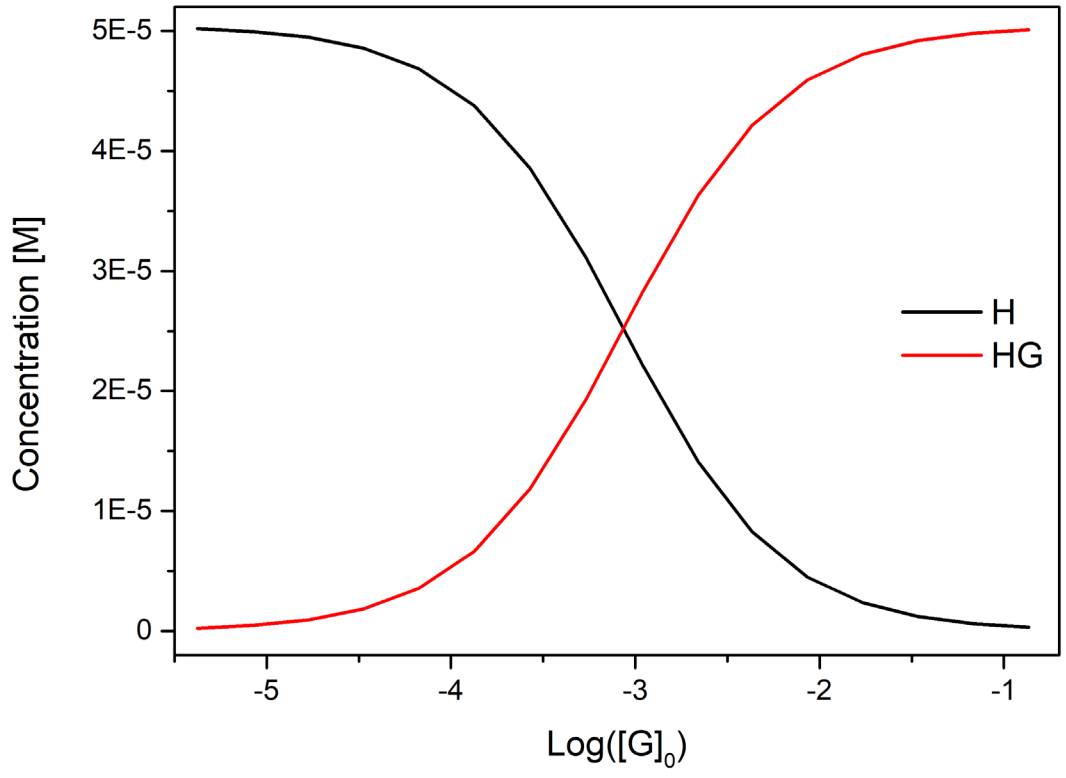

Figure S 26. Calculated species concentration of the titration of **Fe_4(Zn-L)$_6$** with **Py** in acetonitrile (298 K).

Uv-vis binding study of $Fe_4(Zn\text{-}L)_6$ and L1 (HG binding model):

Table S 3. Fitting results for the 1:1 host-guest system between **$Fe_4(Zn\text{-}L)_6$** and **L1** in acetonitrile for K = 6.45 x 10^3 M^{-1} at 298 K.

Wavelength [nm]	ε_{HG} / 10^4	R^2
540	1.35	0.93
555	1.56	0.90
578	0.68	0.98

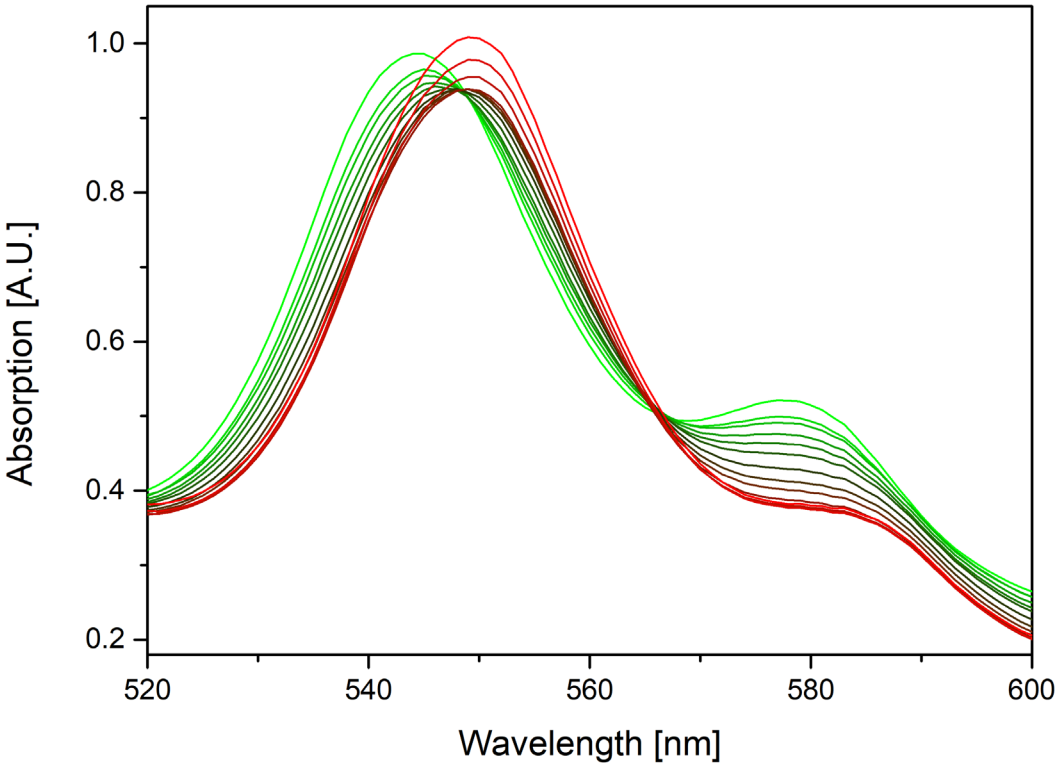

Figure S 27. Overlay of UV-vis spectra of the titration of **$Fe_4(Zn\text{-}L)_6$** (host) with **L1** (guest), at a fixed host concentration of 9.2 µM in acetonitrile at 298 K.

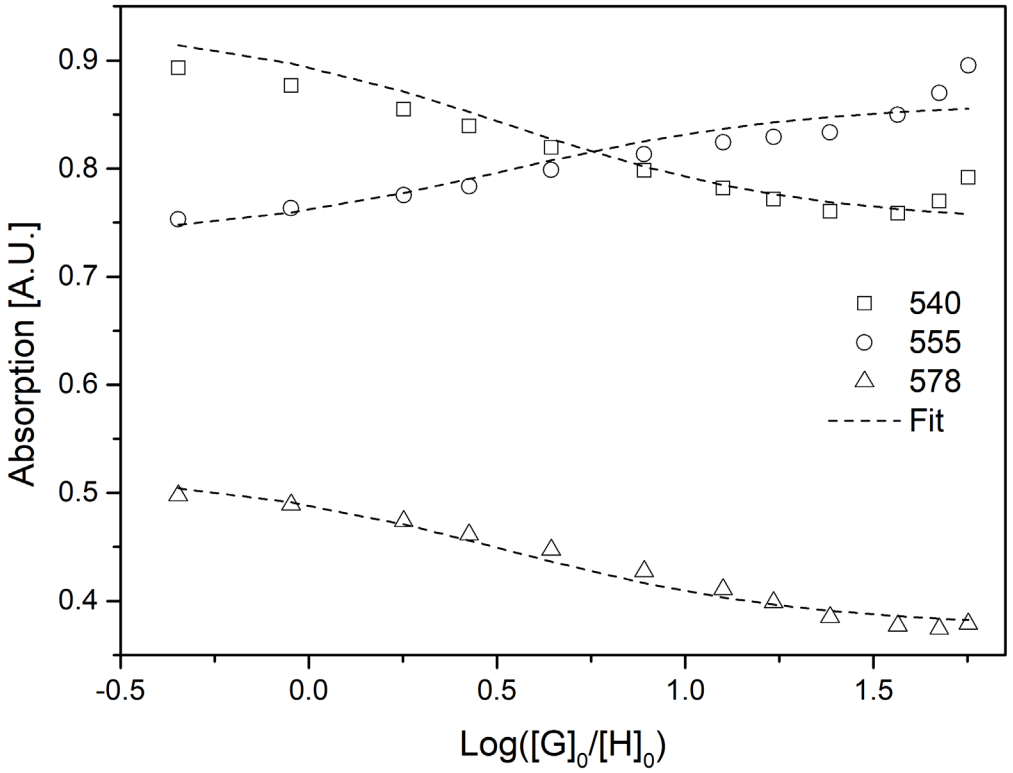

Figure S 28. Fitted UV-vis titration curves of **Fe_4(Zn-L)$_6$** with **L1** in acetonitrile (298 K).

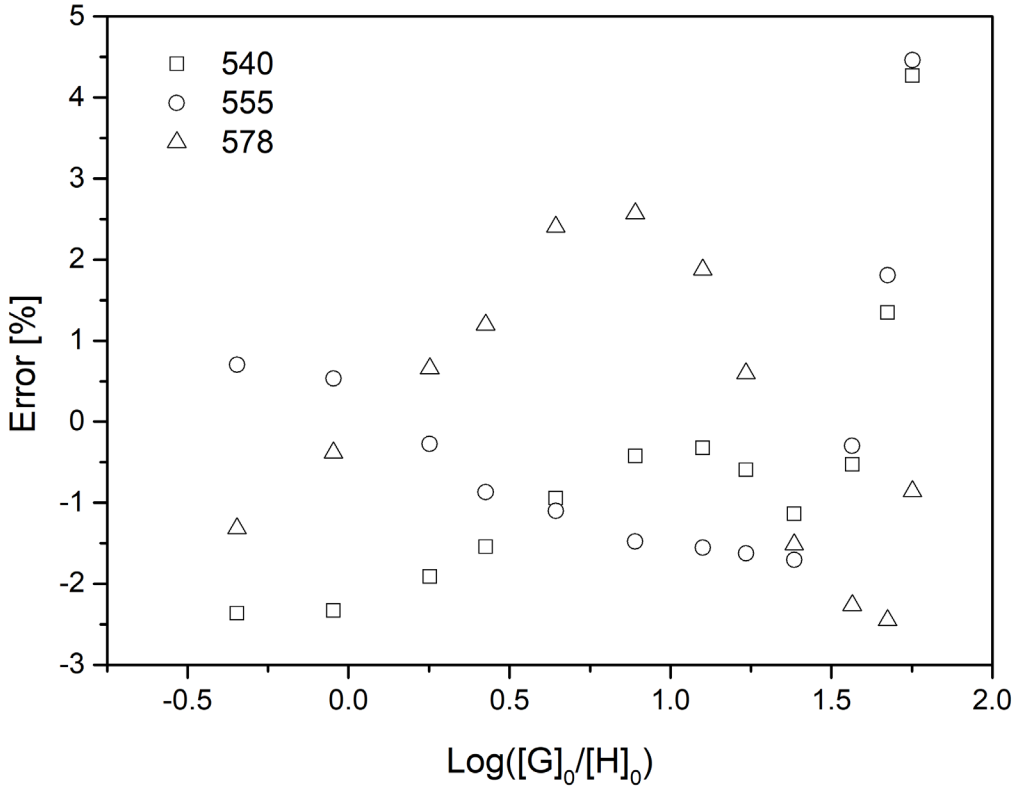

Figure S 29. The error distribution for the fitted curves of **Fe_4(Zn-L)$_6$** with **L1** in acetonitrile (298 K).

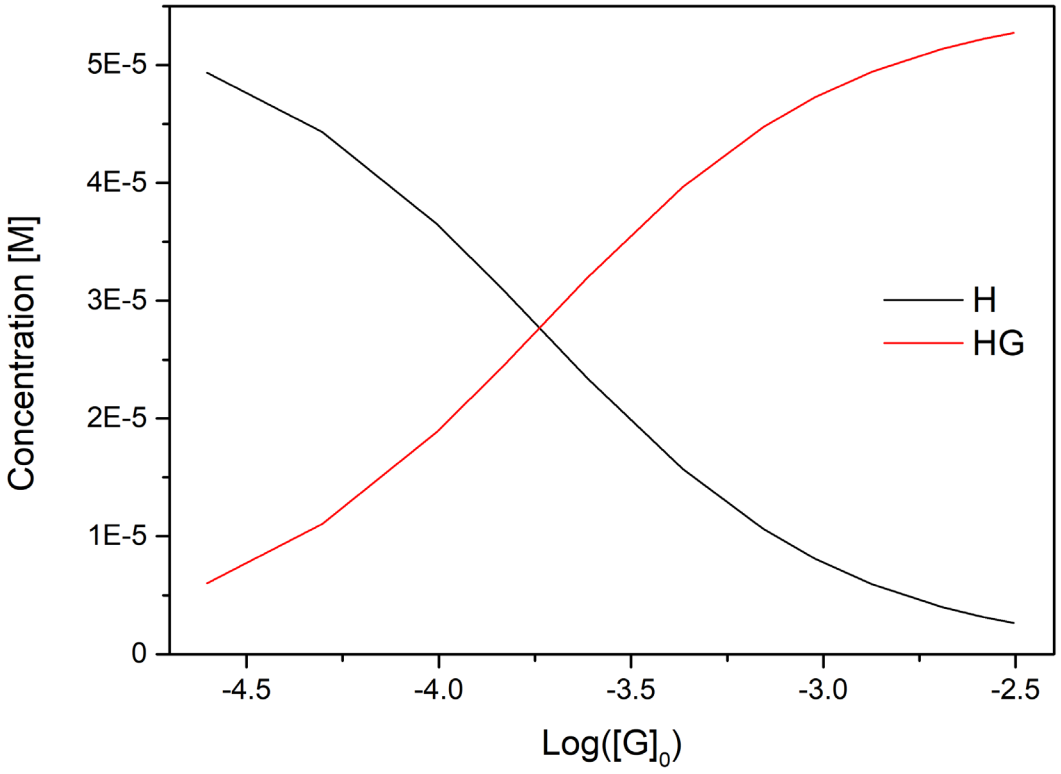

Figure S 30. Calculated species concentration of the titration of **Fe_4(Zn-L)$_6$** with **L1** in acetonitrile (298 K).

Uv-vis binding study of Fe_4(Zn-L)$_6$ and L1 (HGGG binding model):

Table S 4. Fitting results for the 1:3 host-guest system between **Fe_4(Zn-L)$_6$** and **L1** in acetonitrile for K = 2.53 x 10^3 M^{-1} at 298 K, where α_1 = 0.54 and α_2 = 0.53.

Wavelength [nm]	ε_{HG} / 10^4	ε_{HGG} / 10^4	ε_{HGGG} / 10^5	R^2
540	8.33	8.05	0.87	0.972
555	9.13	8.21	1.07	0.986
578	5.63	4.15	0.39	0.995

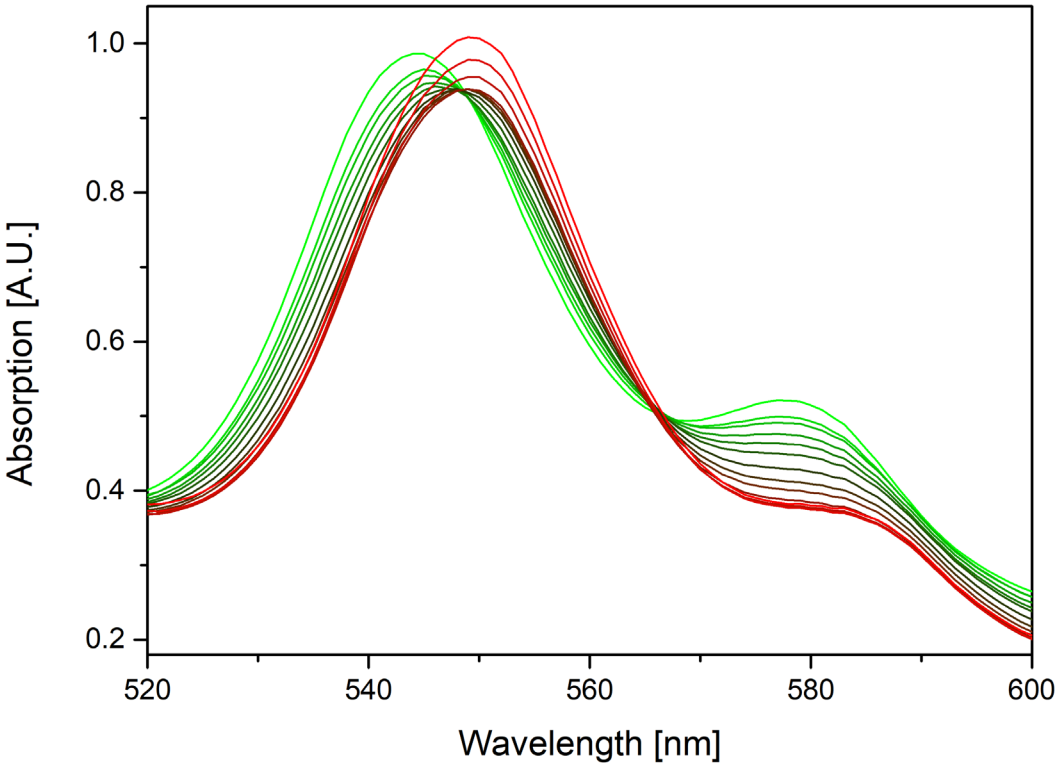

Figure S 31. Overlay of UV-vis spectra of the titration of **Fe_4(Zn-L)$_6$** (host) with **L1** (guest), at a fixed host concentration of 9.2 µM in acetonitrile at 298 K.

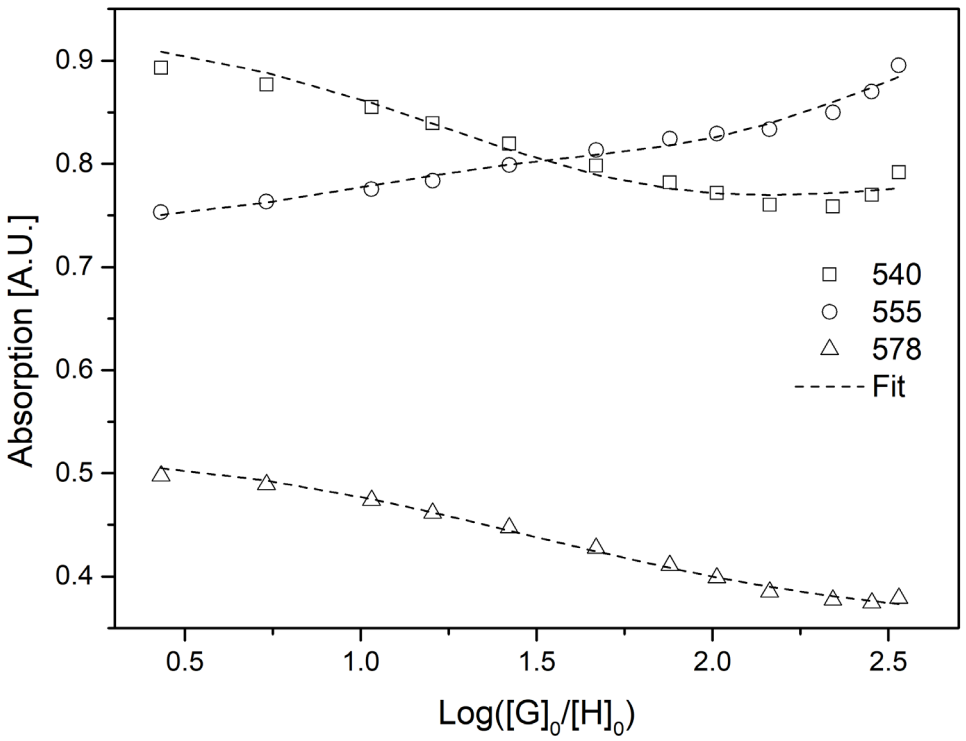

Figure S 32. Fitted UV-vis titration curves of **Fe_4(Zn-L)$_6$** with **L1** in acetonitrile (298 K).

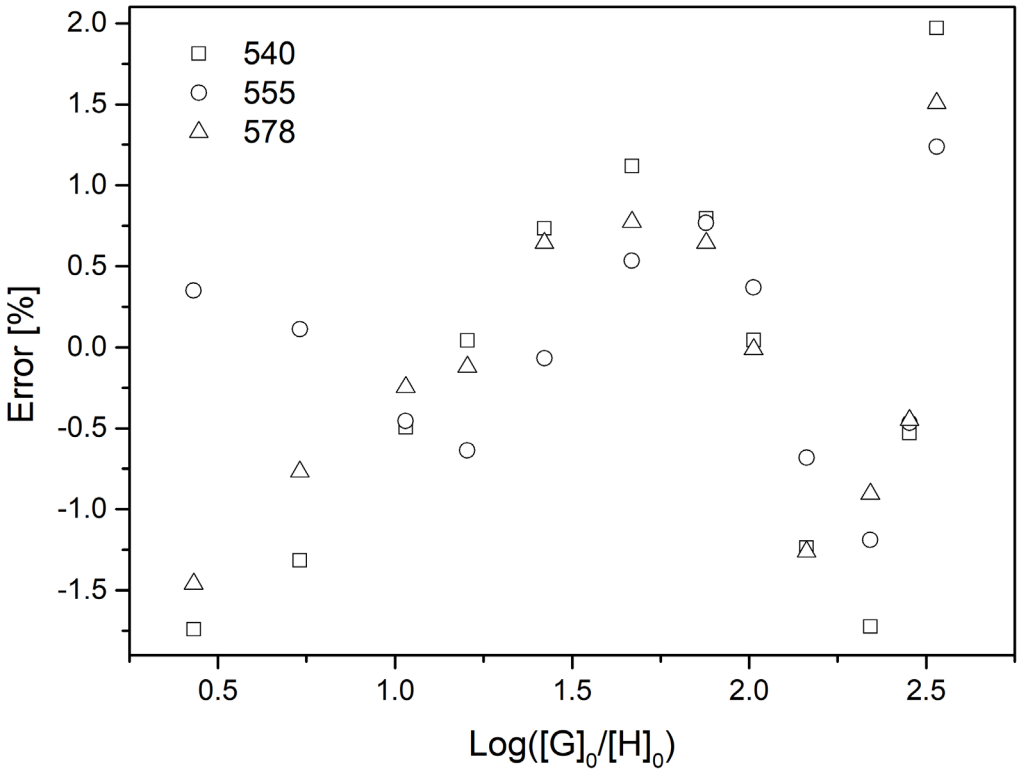

Figure S 33. The error distribution for the fitted curves of **Fe_4(Zn-L)$_6$** with **L1** in acetonitrile (298 K).

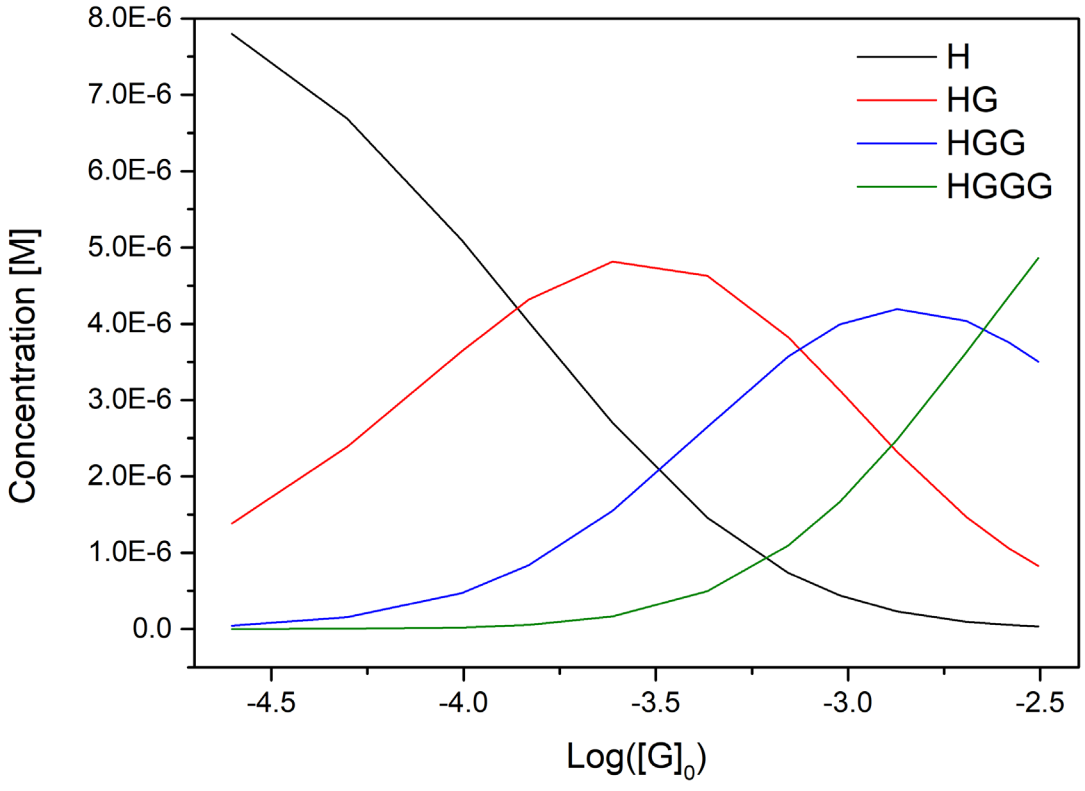

Figure S 34. Calculated species concentration of the titration of **Fe_4(Zn-L)$_6$** with **L1** in acetonitrile (298 K).

Uv-vis binding study of $Fe_4(Zn\text{-}L)_6$ and L2:

Table S 5. Fitting results for the 1:3 host-guest system between **$Fe_4(Zn\text{-}L)_6$** and **L2** in acetonitrile for K = 1.72 x 10^5 M^{-1} at 298 K, where α_1 = 0.39 and α_2 = 0.02.

Wavelength [nm]	ε_{HG} / 10^4	ε_{HGG} / 10^4	ε_{HGGG} / 10^5	R^2
540	9.43	8.80	0.90	0.97
555	9.14	8.96	1.13	0.99
578	4.41	4.20	0.34	0.98

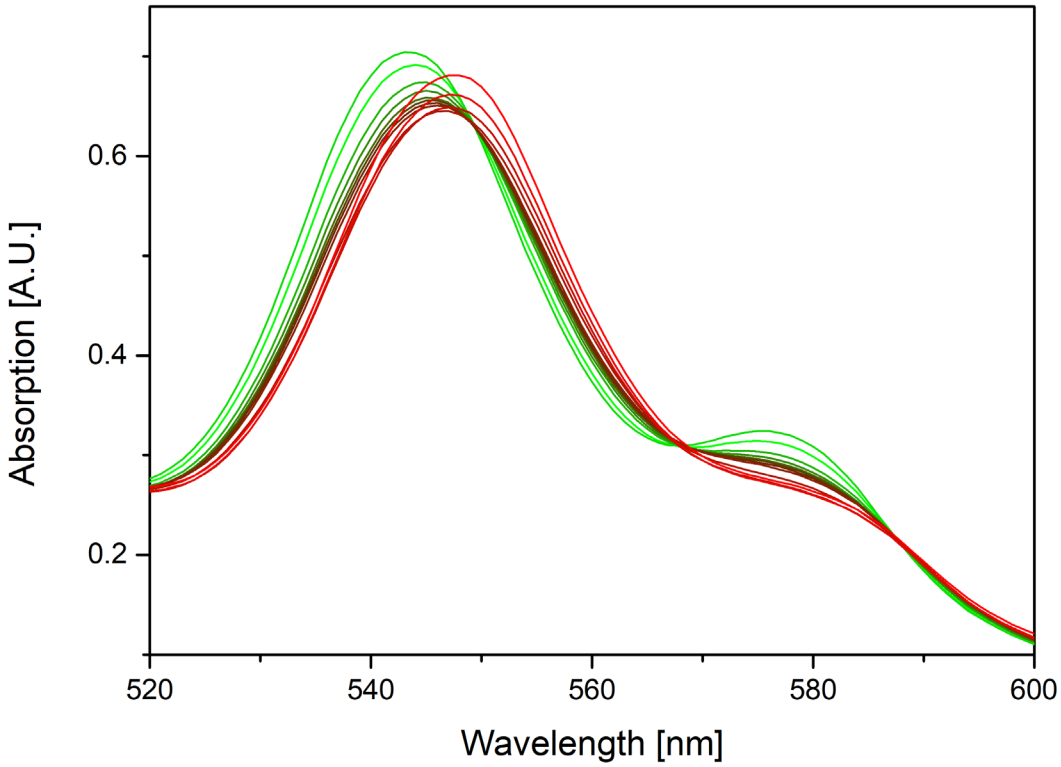

Figure S 35. Overlay of UV-vis spectra of the titration of **$Fe_4(Zn\text{-}L)_6$** (host) with **L2** (guest), at a fixed host concentration of 6.3 µM in acetonitrile at 298 K.

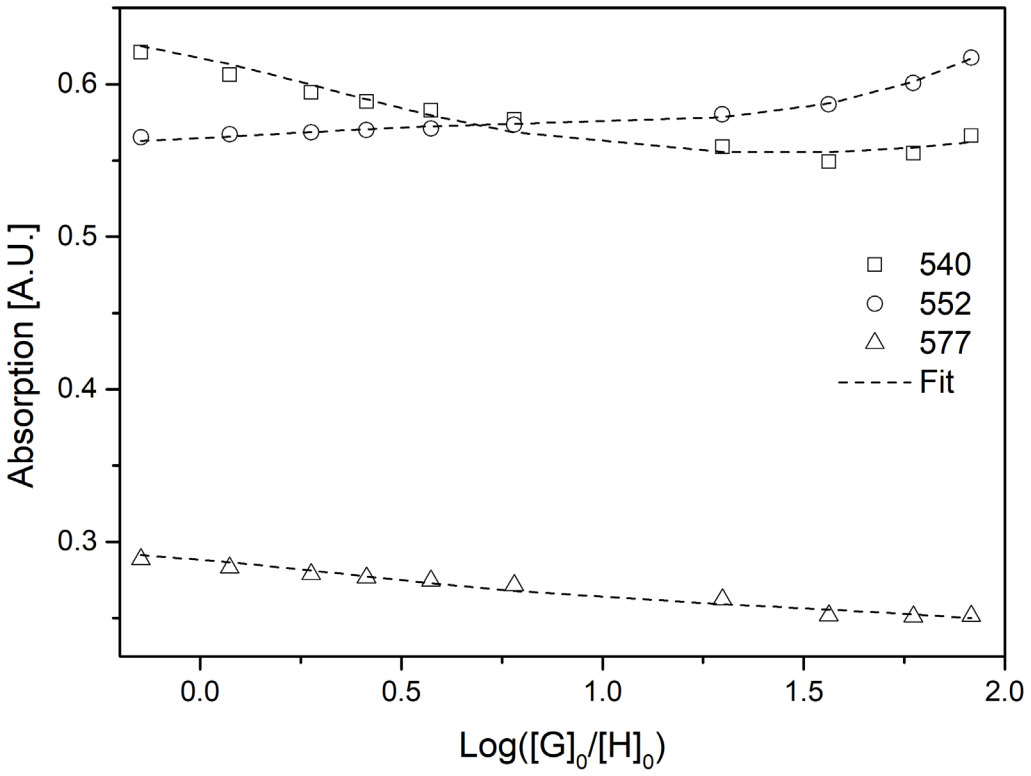

Figure S 36. Fitted UV-vis titration curves of **Fe_4(Zn-L)$_6$** with **L2** in acetonitrile (298 K).

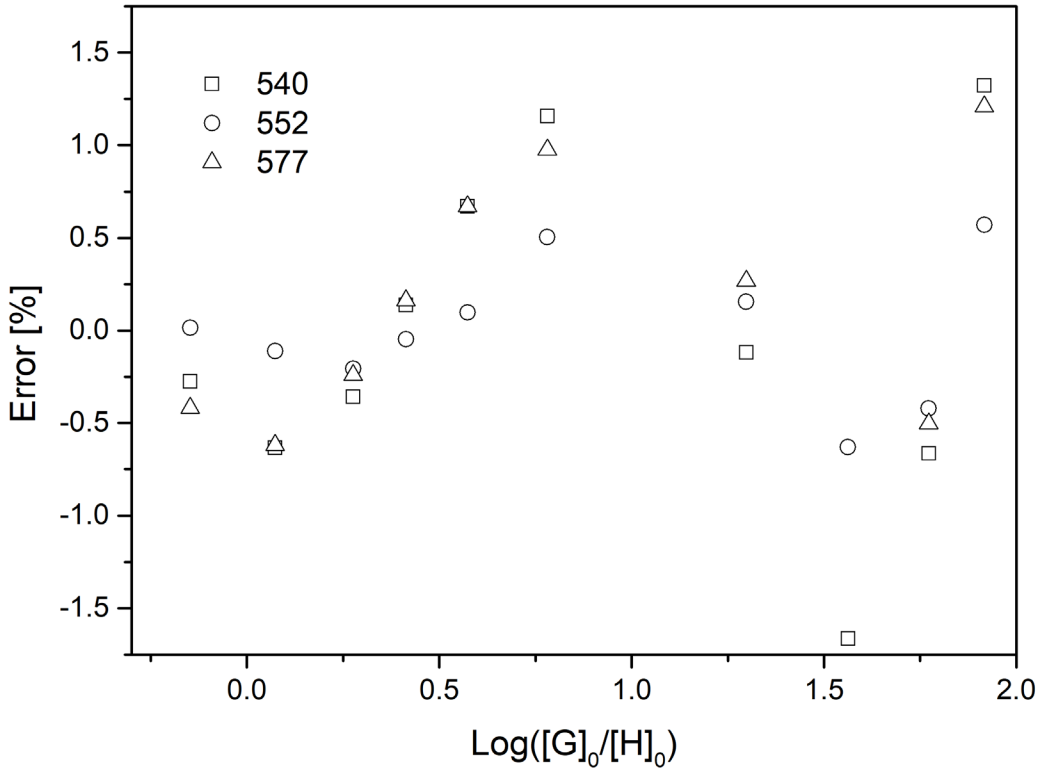

Figure S 37. The error distribution for the fitted curves of **Fe_4(Zn-L)$_6$** with **L2** in acetonitrile (298 K).

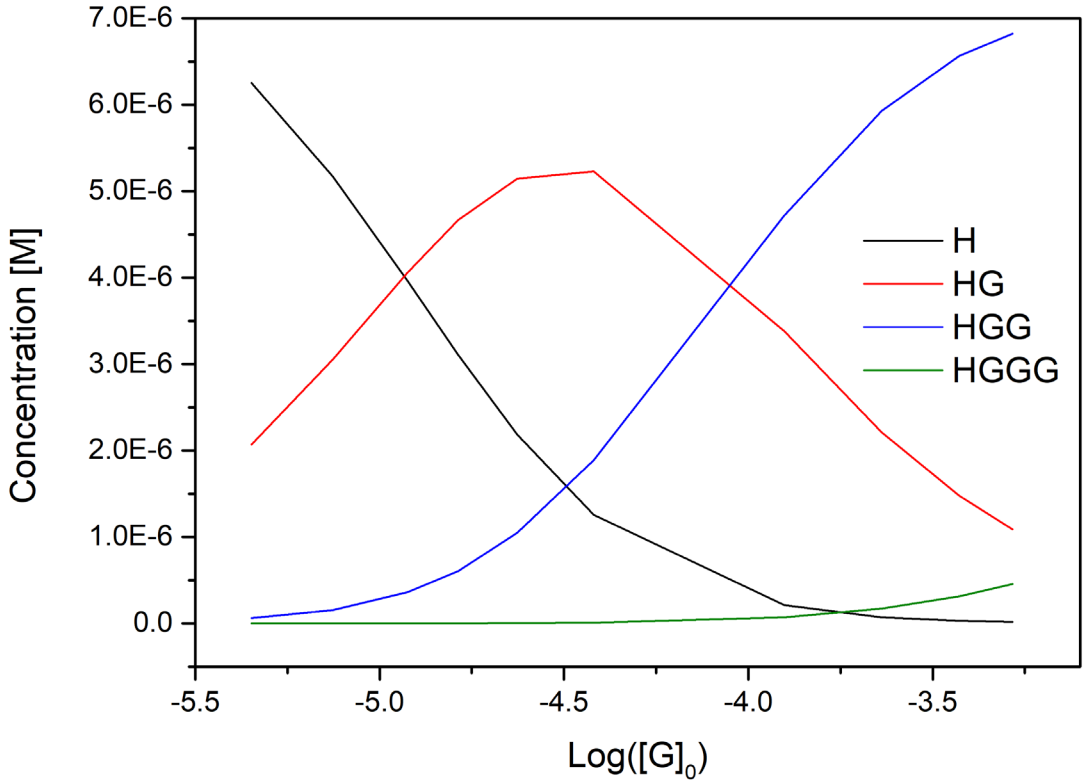

Figure S 38. Calculated species concentration of the titration of **Fe_4(Zn-L)$_6$** with **L2** in acetonitrile (298 K).

Uv-vis binding study of Fe_4(Zn-L)$_6$ and L3:

Table S 6. Fitting results for the 1:3 host-guest system between **Fe_4(Zn-L)$_6$** and **L3** in acetonitrile for K = 3.12 x 10^5 M^{-1} at 298 K, where α_1 = 1.13 and α_2 = 0.02.

Wavelength [nm]	ε_{HG} / 10^5	ε_{HGG} / 10^5	ε_{HGGG} / 10^5	R^2
544	0.92	1.00	1.20	0.994
548	1.02	1.04	1.31	0.977
576	0.38	0.42	0.32	0.984

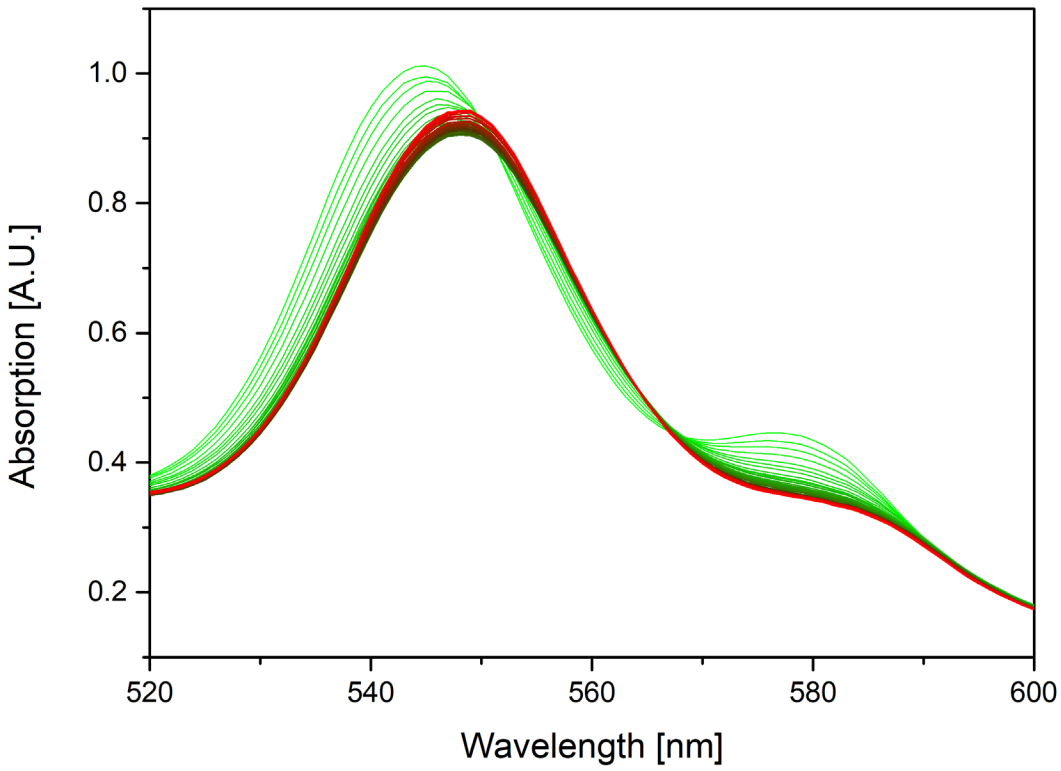

Figure S 39. Overlay of UV-vis spectra of the titration of **Fe_4(Zn-L)$_6$** (host) with **L3** (guest), at a fixed host concentration of 8.8 µM in acetonitrile at 298 K.

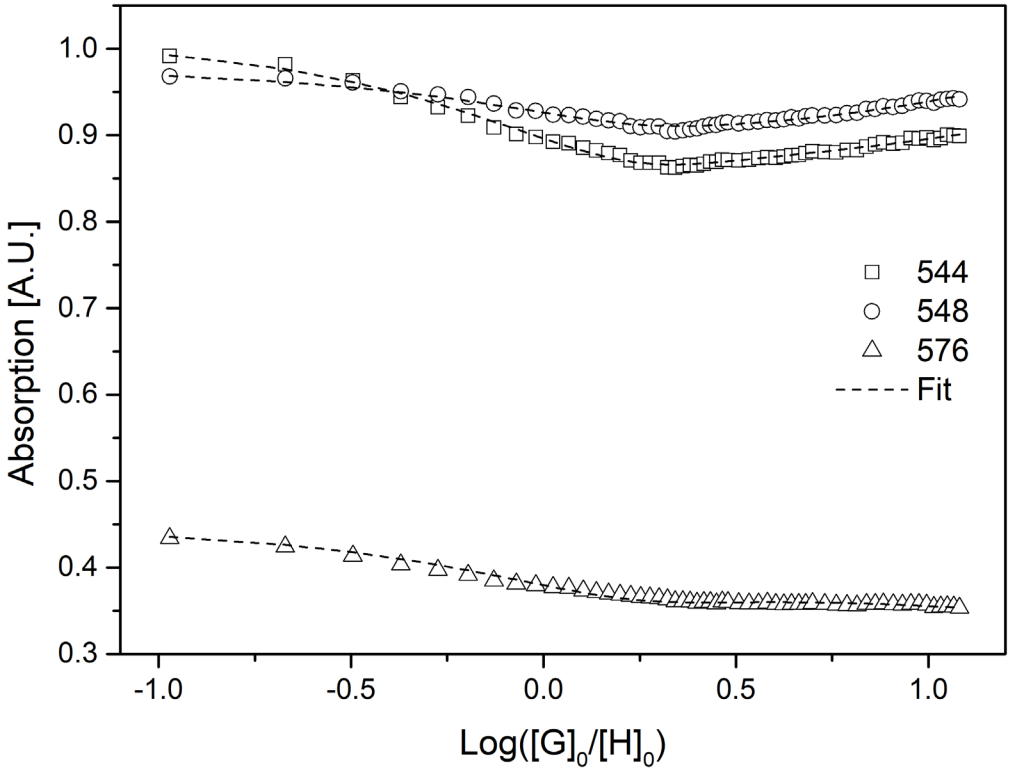

Figure S 40. Fitted UV-vis titration curves of **Fe_4(Zn-L)$_6$** with **L3** in acetonitrile (298 K).

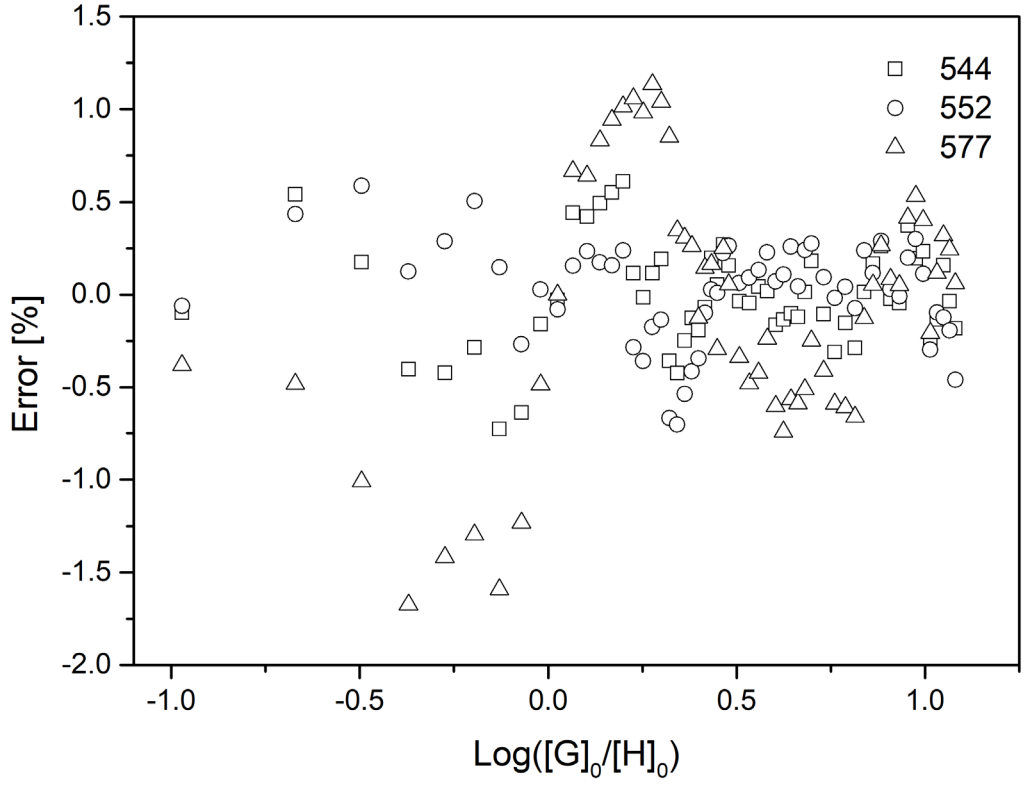

Figure S 41. The error distribution for the fitted curves of **Fe_4(Zn-L)$_6$** with **L3** in acetonitrile (298 K).

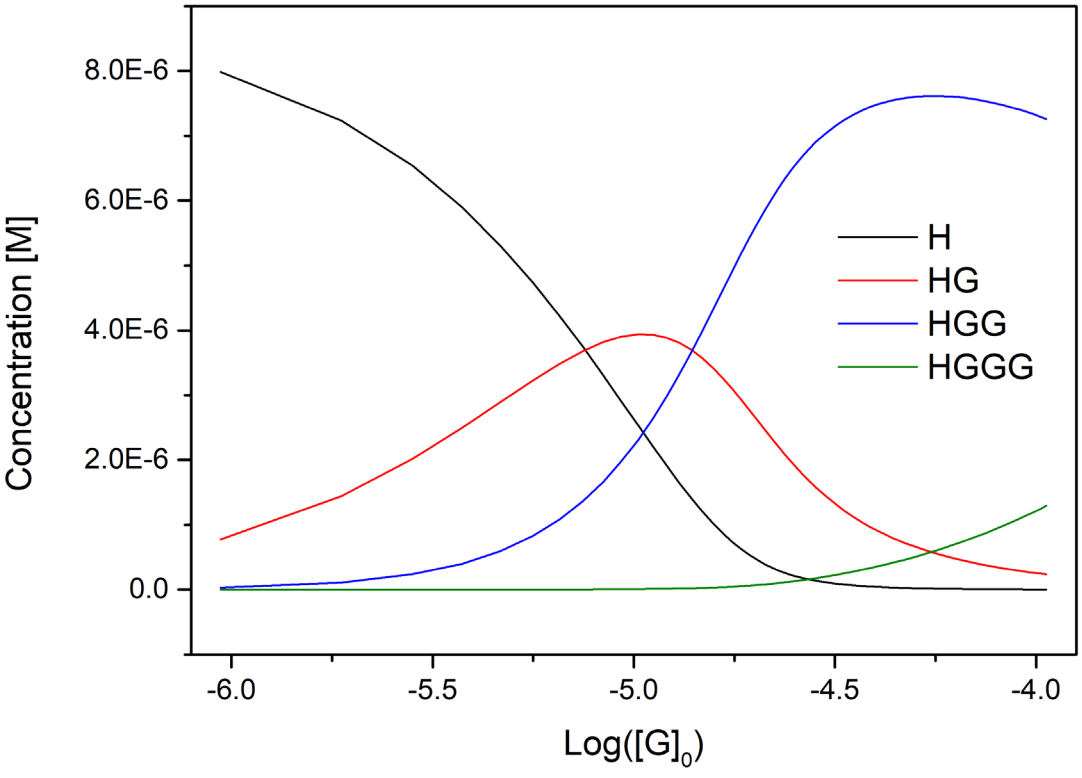

Figure S 42. Calculated species concentration of the titration of **Fe_4(Zn-L)$_6$** with **3** in acetonitrile (298 K).

Uv-vis binding study of $Fe_4(Zn\text{-}L)_6$ and Au1:

Table S 7. Fitting results for the 1:3 host-guest system between **$Fe_4(Zn\text{-}L)_6$** and **Au1** in acetonitrile for K = 4.08 x 10^4 M^{-1} at 298 K, where α_1 = 0.06 and α_2 = 0.05.

Wavelength [nm]	ε_{HG} / 10^4	ε_{HGG} / 10^5	ε_{HGGG} / 10^5	R^2
540	9.46	0.97	0.61	0.985
557	8.27	0.93	0.96	0.995
587	4.00	0.52	0.80	0.996

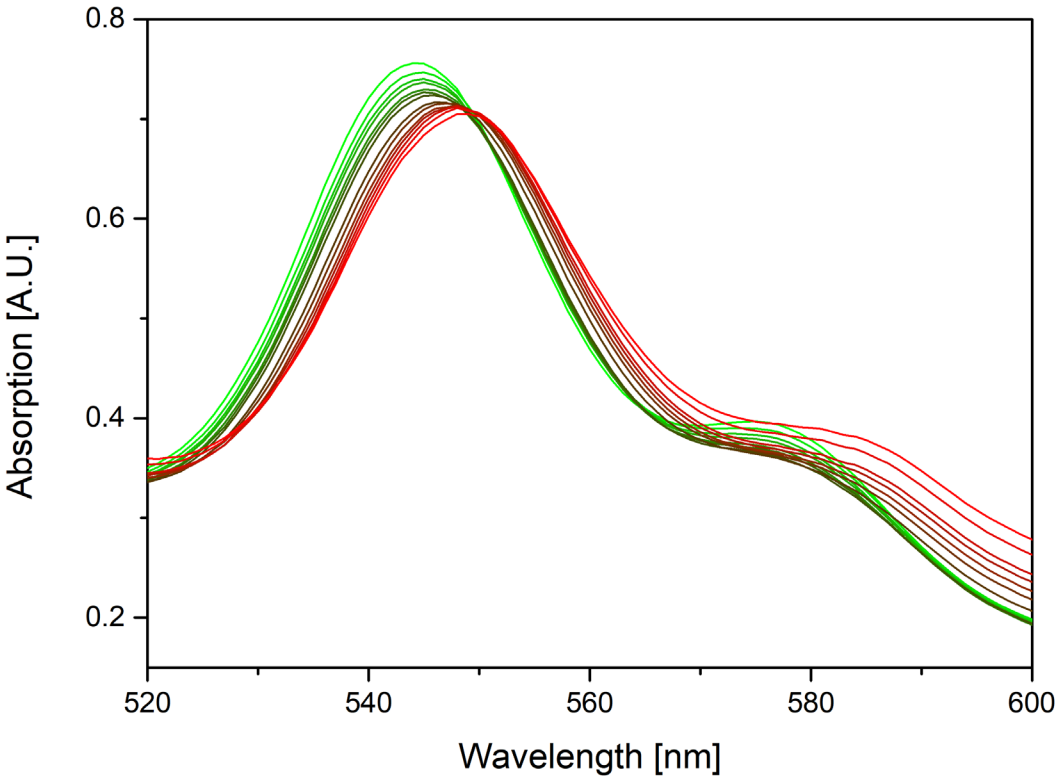

Figure S 43. Overlay of UV-vis spectra of the titration of **$Fe_4(Zn\text{-}L)_6$** (host) with **Au1** (guest), at a fixed host concentration of 8.8 µM in acetonitrile at 298 K.

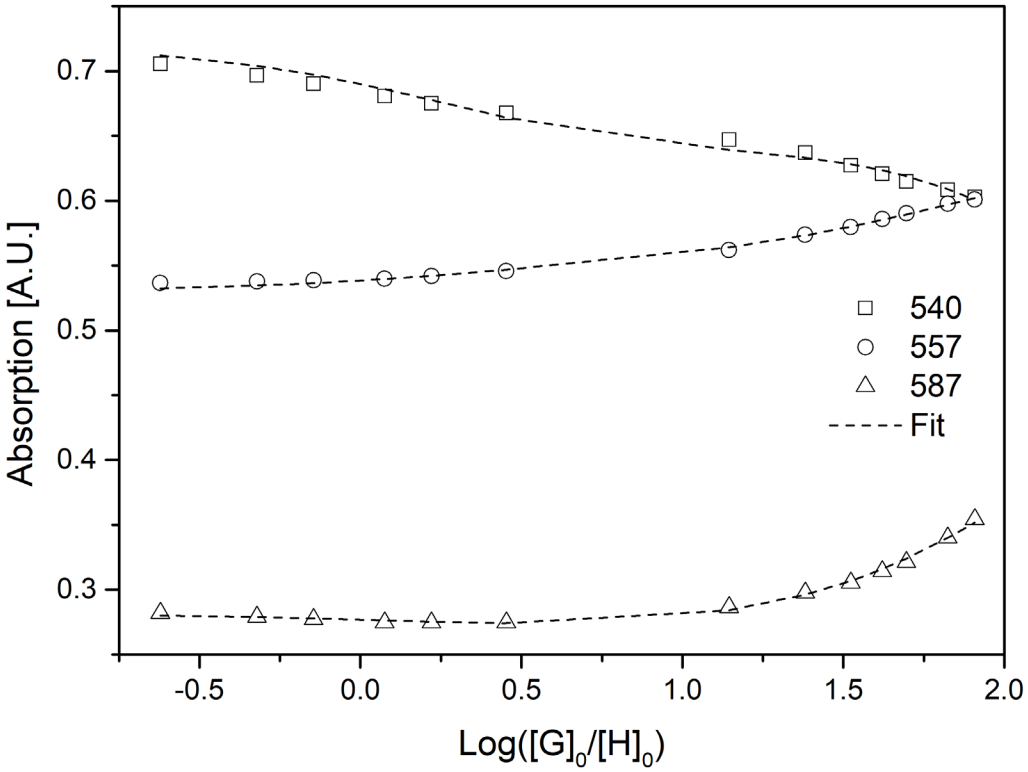

Figure S 44. Fitted UV-vis titration curves of **Fe_4(Zn-L)$_6$** with **Au1** in acetonitrile (298 K).

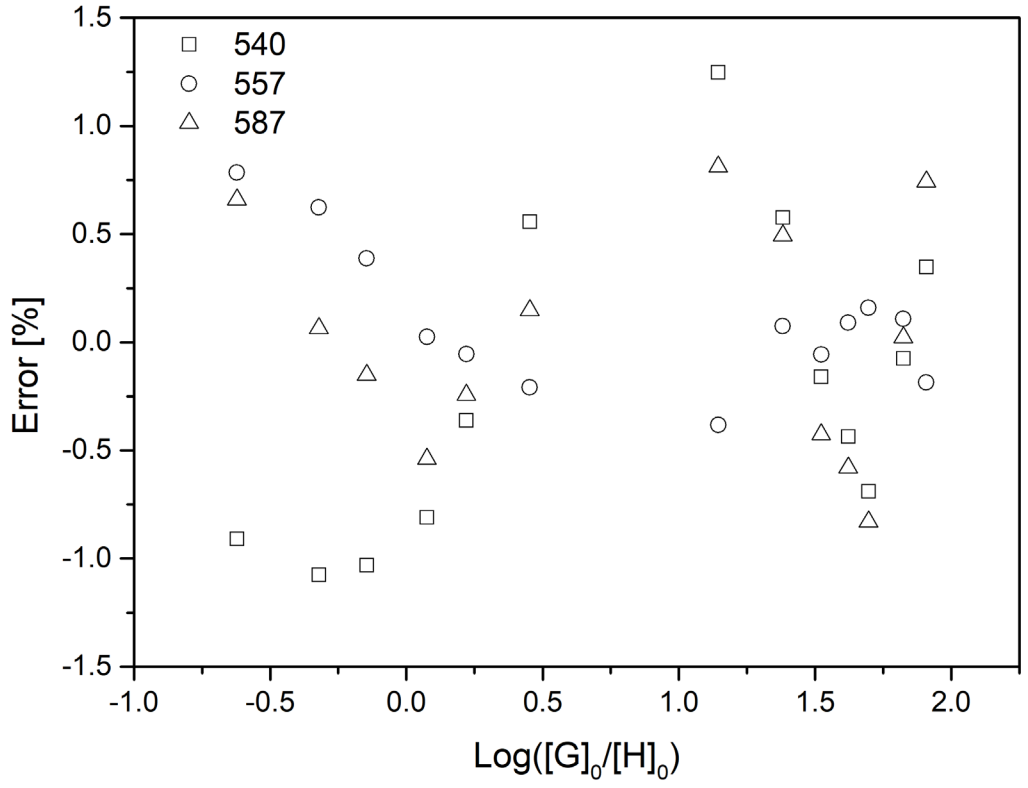

Figure S 45. The error distribution for the fitted curves of **Fe_4(Zn-L)$_6$** with **Au1** in acetonitrile (298 K).

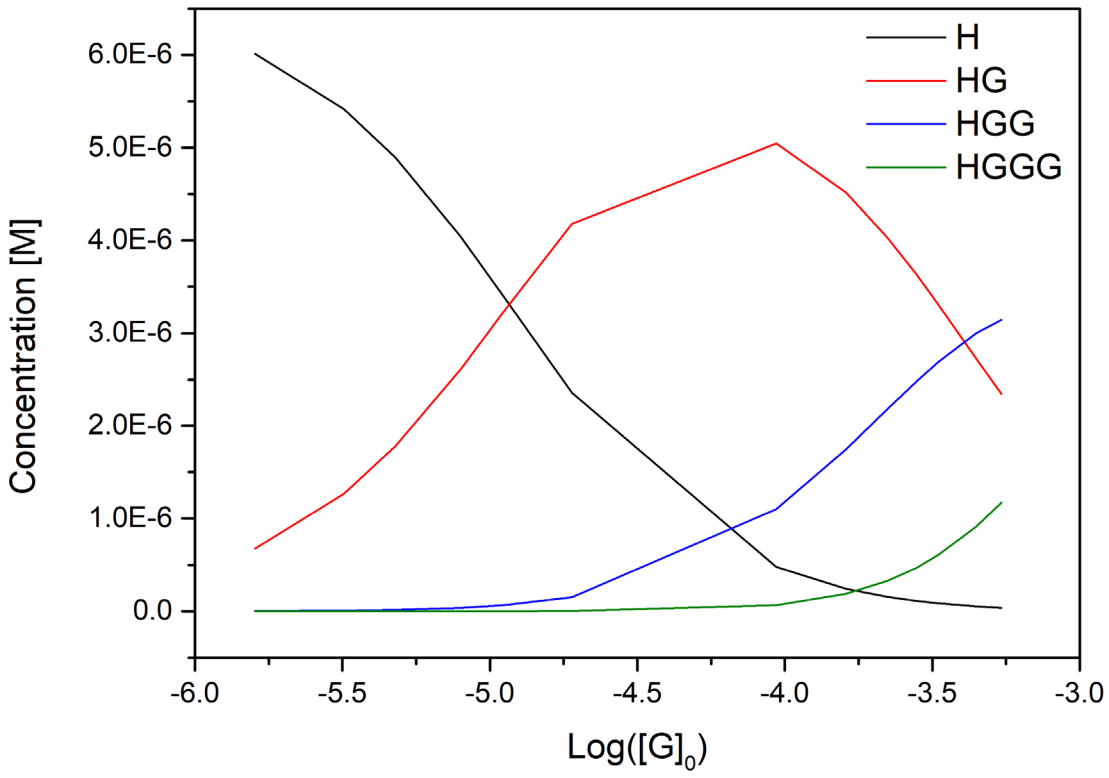

Figure S 46. Calculated species concentration of the titration of **Fe_4(Zn-L)$_6$** with **Au1** in acetonitrile (298 K).

Uv-vis binding study of ZnTPP and Py (control titration):

Table S 8. Fitting results for the 1:1 host-guest system between **ZnTPP** and **Py** in acetonitrile for K = 1.18 x 10^3 M^{-1} at 298 K.

Wavelength [nm]	ε_{HG} / 10^5	R^2
556	0.16	0.9977
561	0.19	0.9967
601	0.11	0.9973

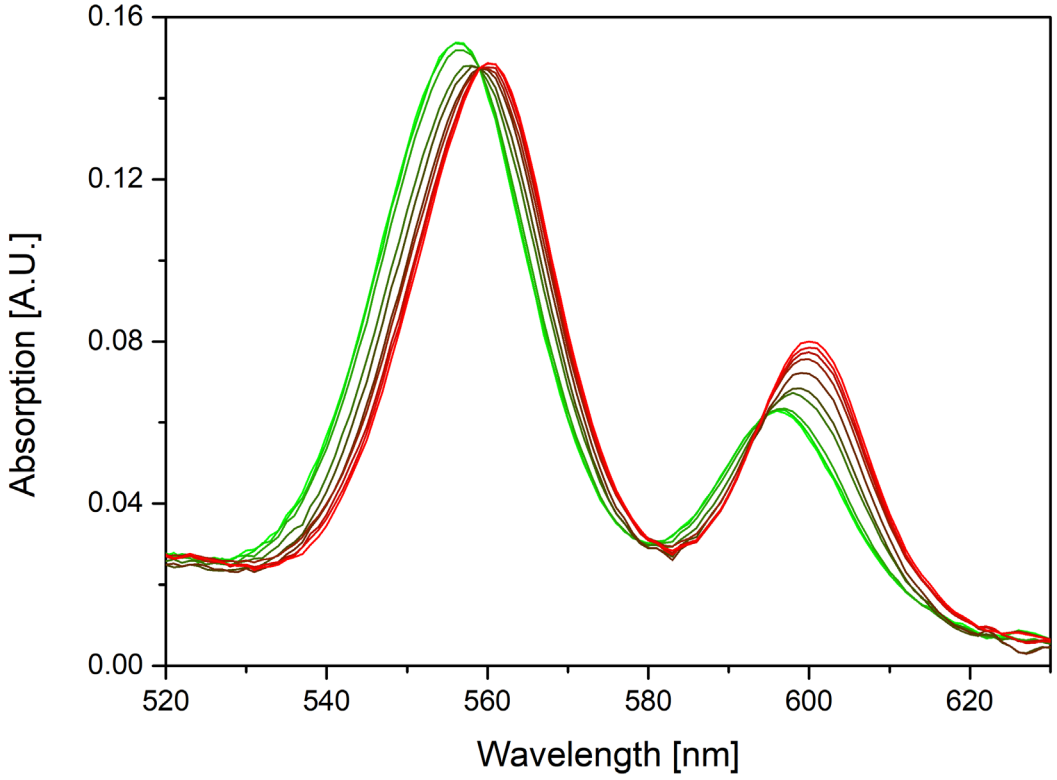

Figure S 47. Overlay of UV-vis spectra of the titration of **ZnTPP** (host) with **Py** (guest), at a fixed host concentration of 8.0 µM in acetonitrile at 298 K.

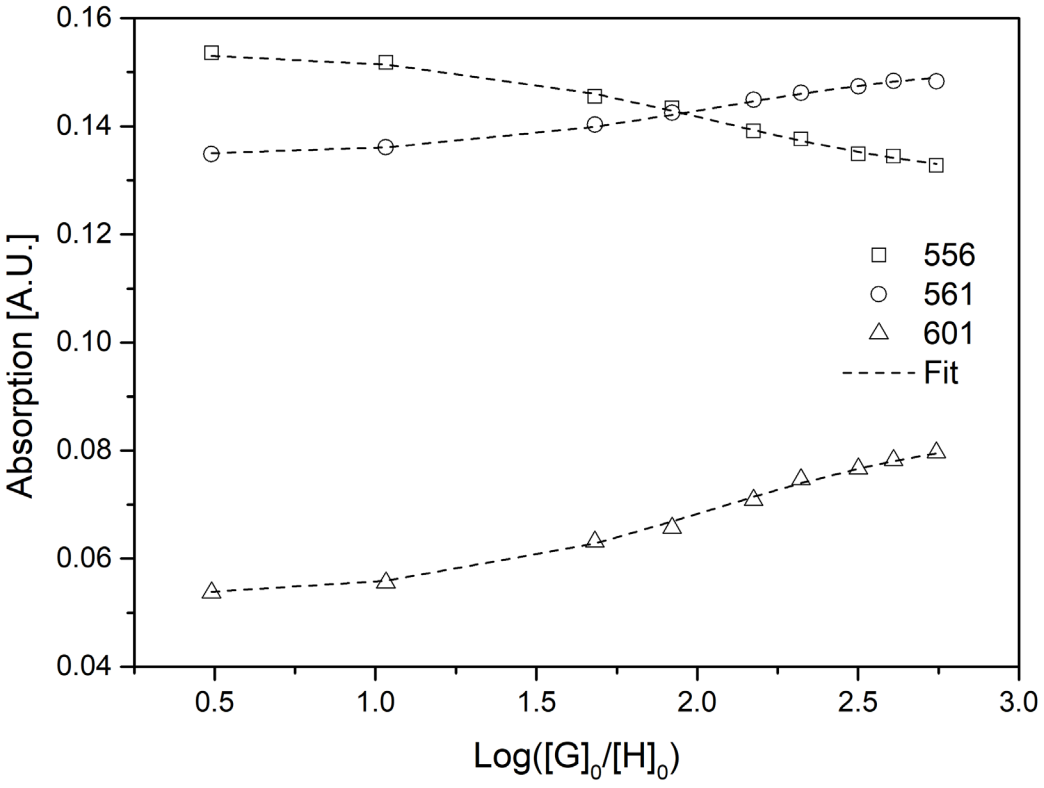

Figure S 48. Fitted UV-vis titration curves of **ZnTPP** with **Py** in acetonitrile (298 K).

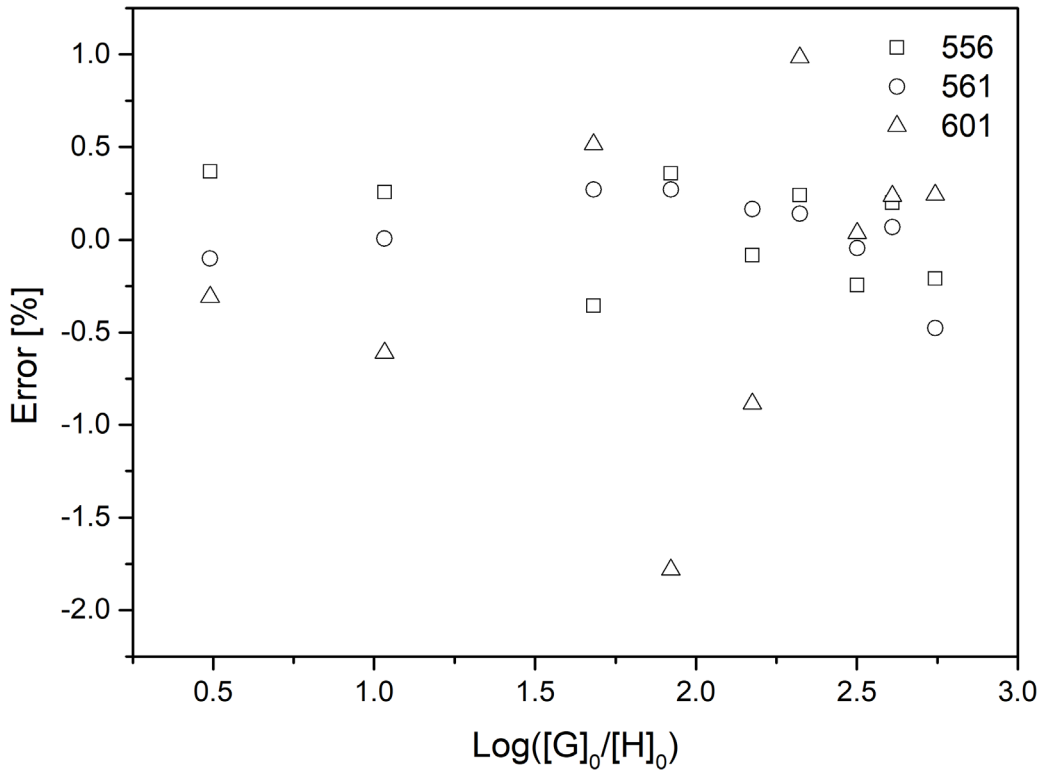

Figure S 49. The error distribution for the fitted curves of **ZnTPP** with **Py** in acetonitrile (298 K).

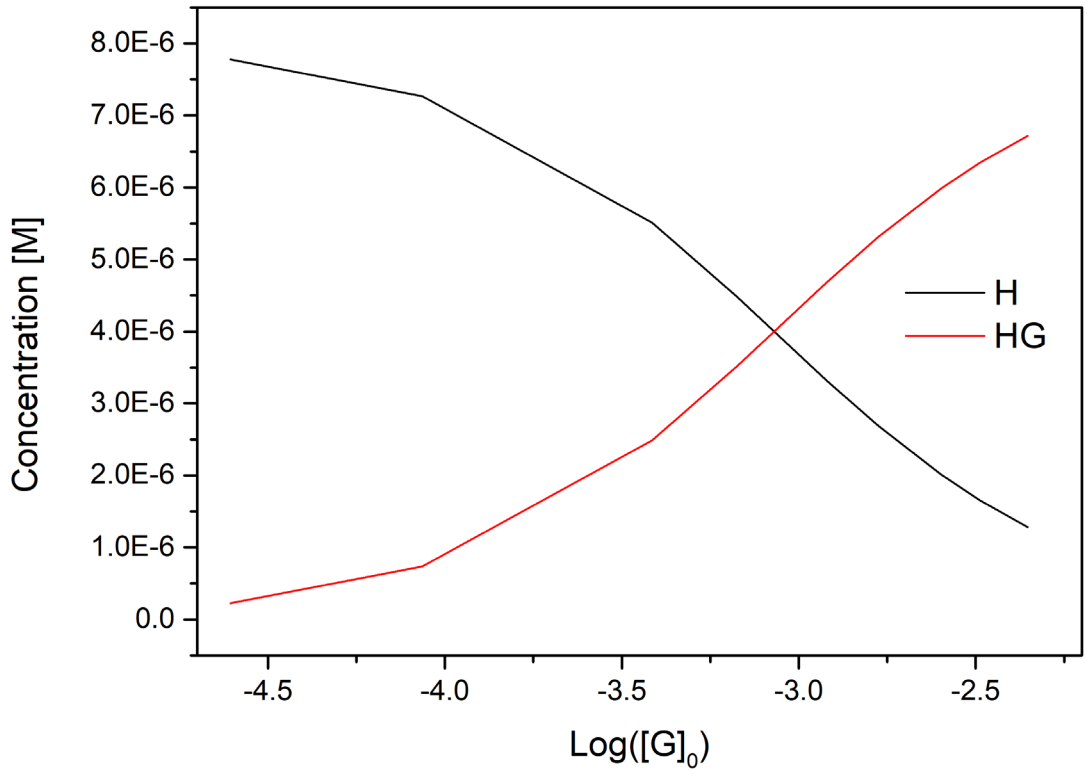

Figure S 50. Calculated species concentration of the titration of **ZnTPP** with **Py** in acetonitrile (298 K).

8. Encapsulation studies of $Fe_4(Zn\text{-}L)_6$ with various guests

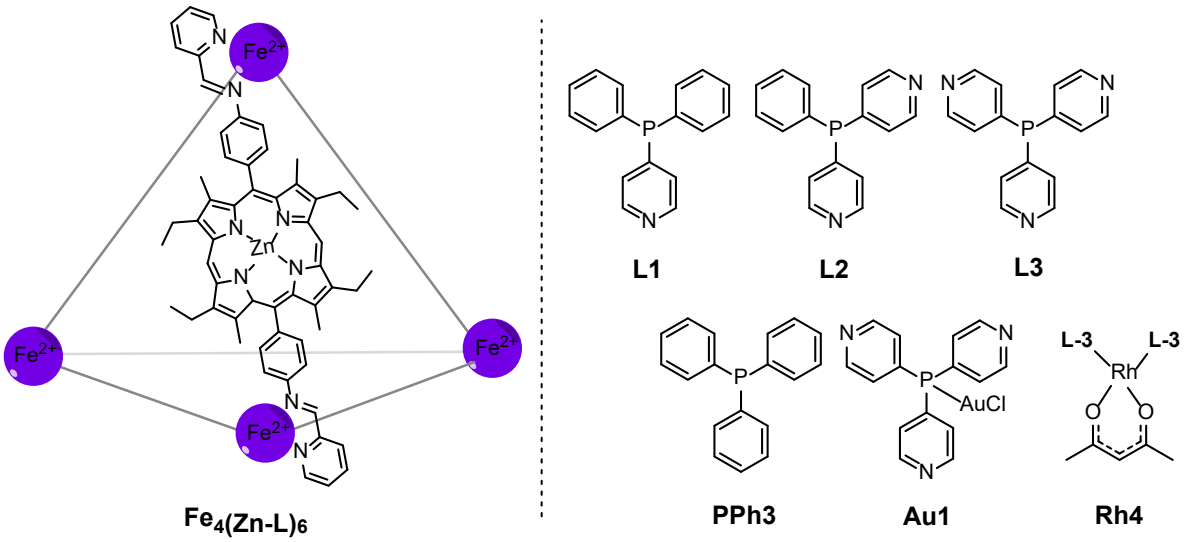

Encapsulation of the various guests was studied using ^{1}H NMR and 2D ^{1}H DOSY NMR spectroscopy under N_2 in CD_3CN at 298 K, in addition with mass spectroscopy. For the strongly bound guests **L2**, **L3** and **Rh4** both ^{1}H NMR and 2D ^{1}H DOSY NMR measurements were performed, and for the rest of the guests **L1**, **PPh_3** and **Au1** the encapsulation was studied by ^{1}H NMR spectroscopy and/or mass spectroscopy.

Encapsulation study of $Fe_4(Zn\text{-}L)_6$ and L1

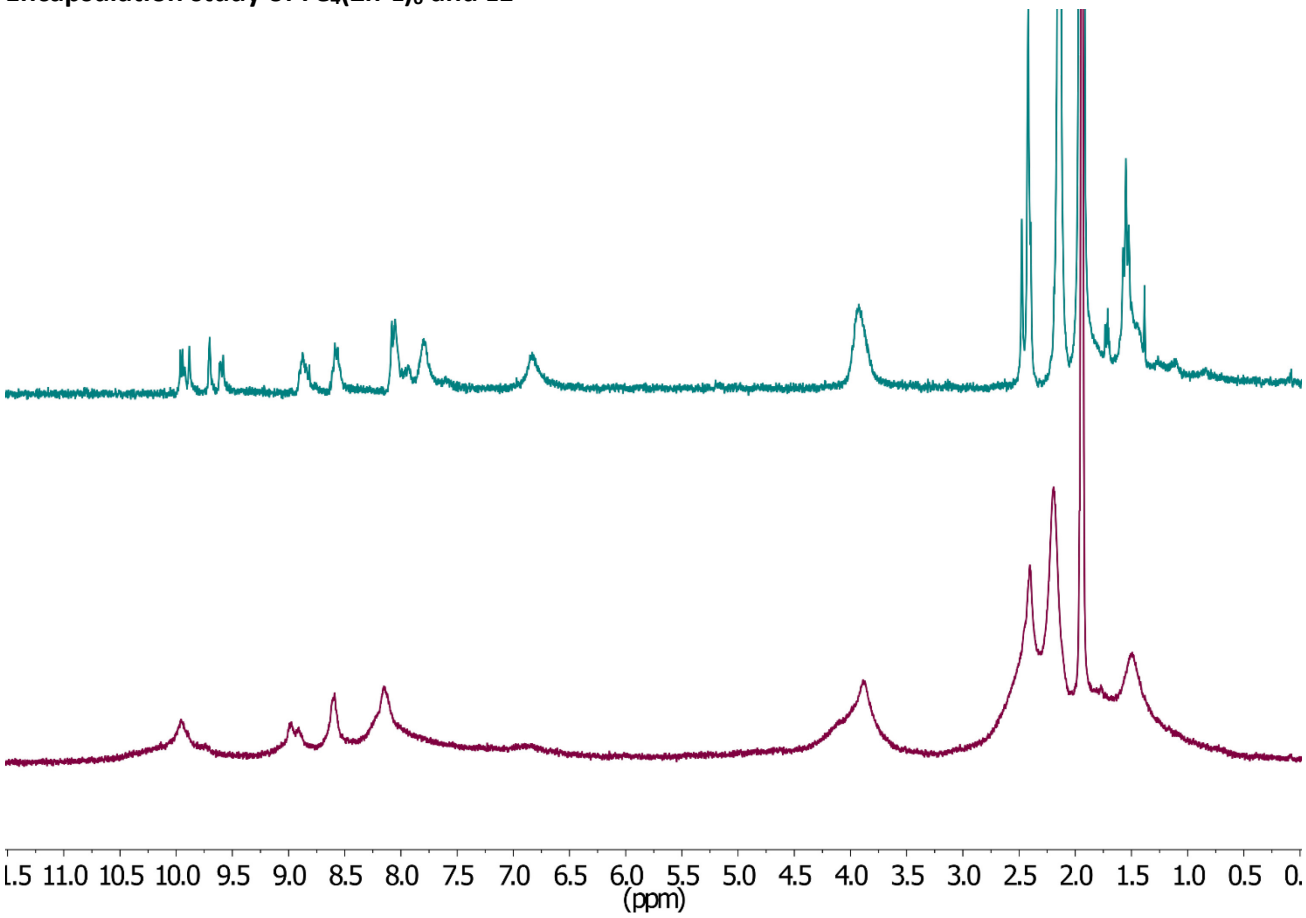

Figure S 51. ^{1}H NMR (400 MHz, 298 K) of **$Fe_4(Zn\text{-}L)_6$** (top) and **$(L1)_2@Fe_4(Zn\text{-}L)_6$** (bottom) in CD_3CN.

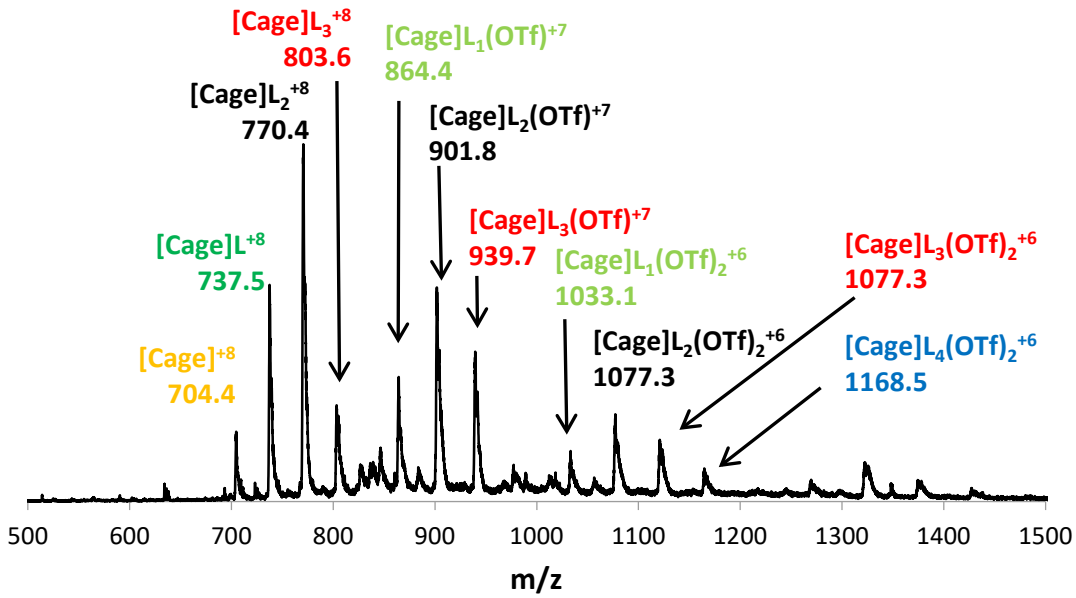

Figure S 52. ESI-MS spectrum of **$(L1)_2@Fe_4(Zn\text{-}L)_6$**. In the image **L** = **L1**.

Encapsulation study of $Fe_4(Zn\text{-}L)_6$ and L2

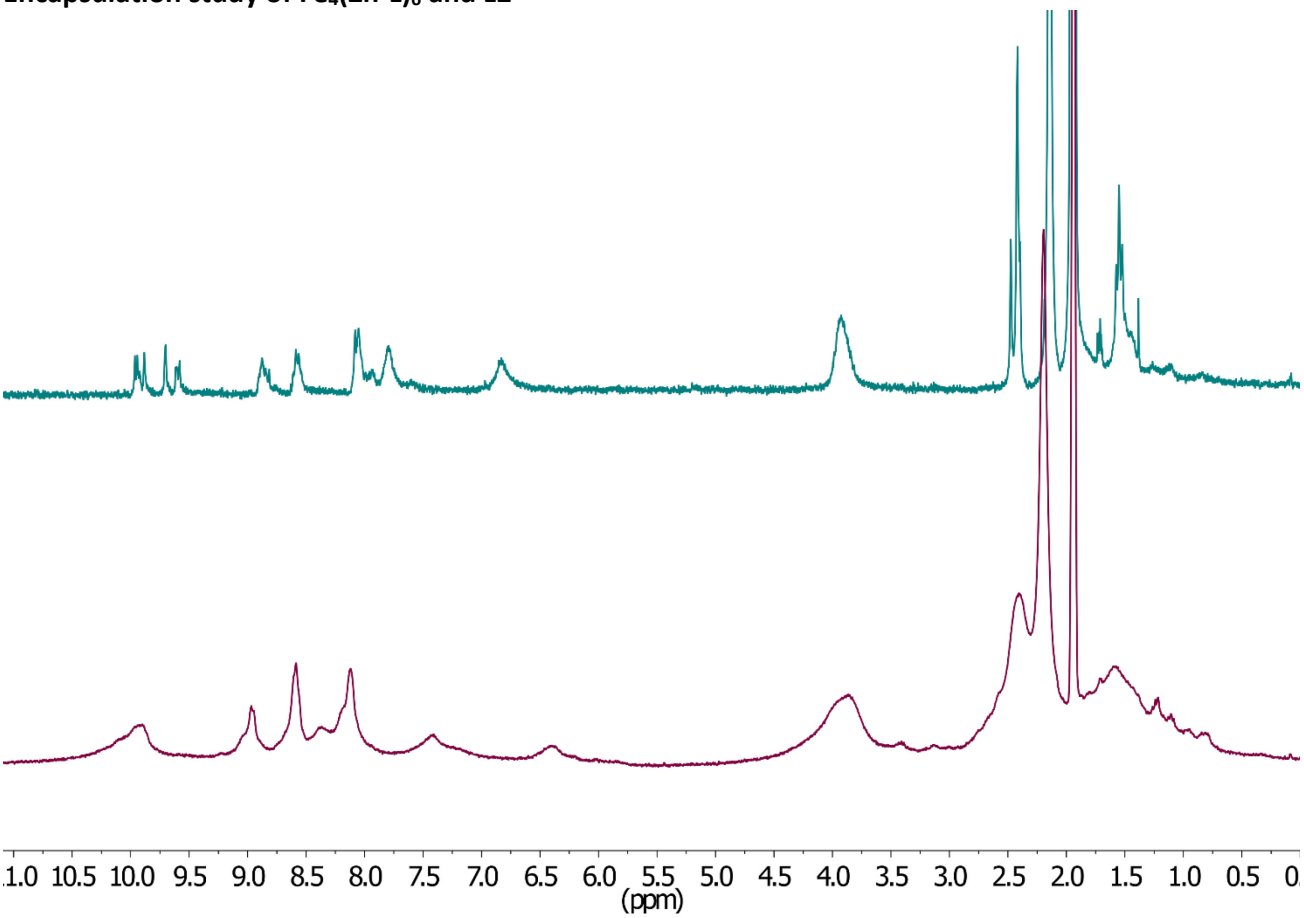

Figure S 53. ^{1}H NMR (400 MHz, 298 K) of **$Fe_4(Zn\text{-}L)_6$** (top) and **$(L2)_2@Fe_4(Zn\text{-}L)_6$** ((bottom) in CD_3CN.

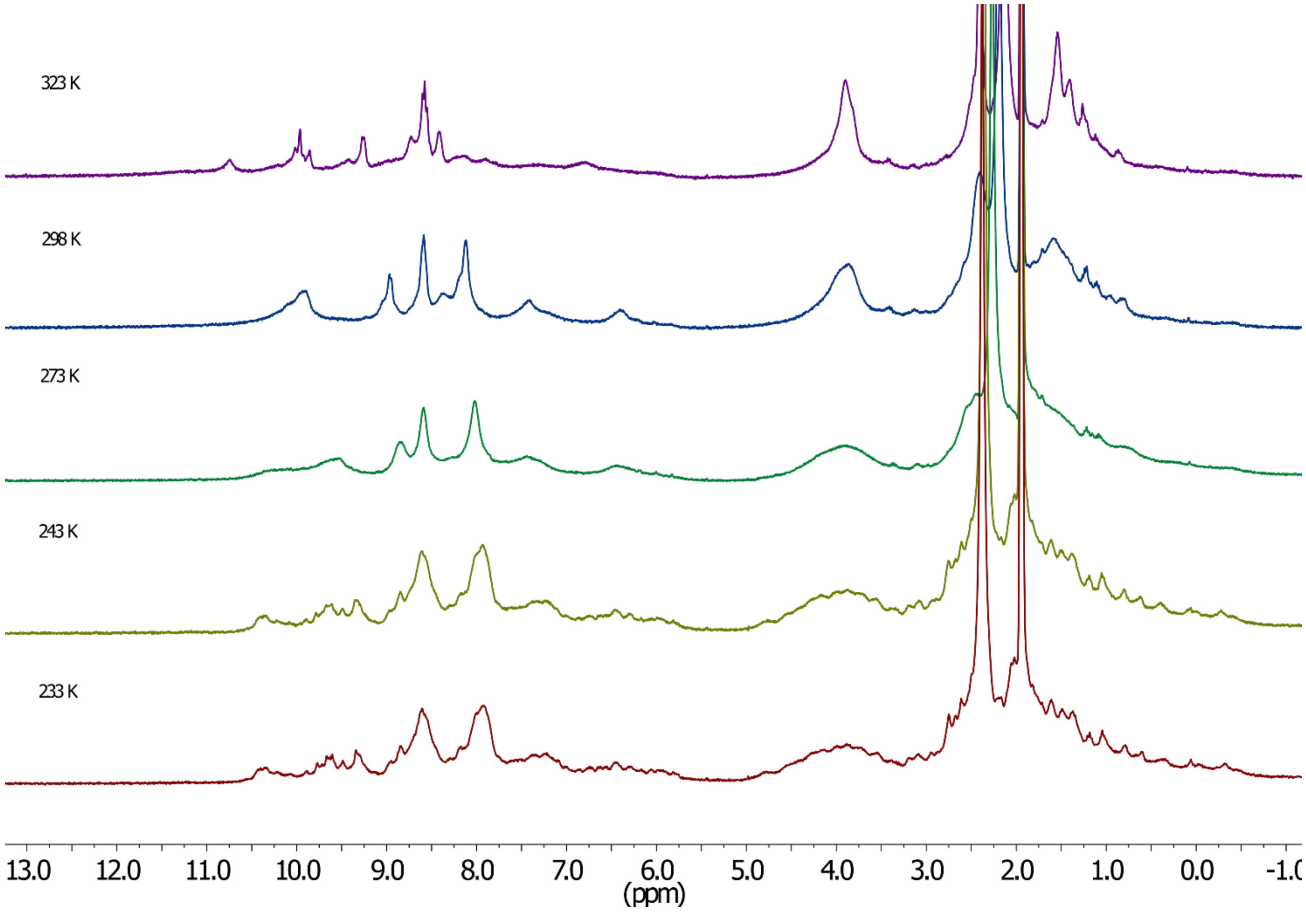

Figure S 54. Variable temperature ^{1}H NMR (300 MHz, 298 K) of **$(L2)_2$@Fe_4(Zn-L)$_6$**.

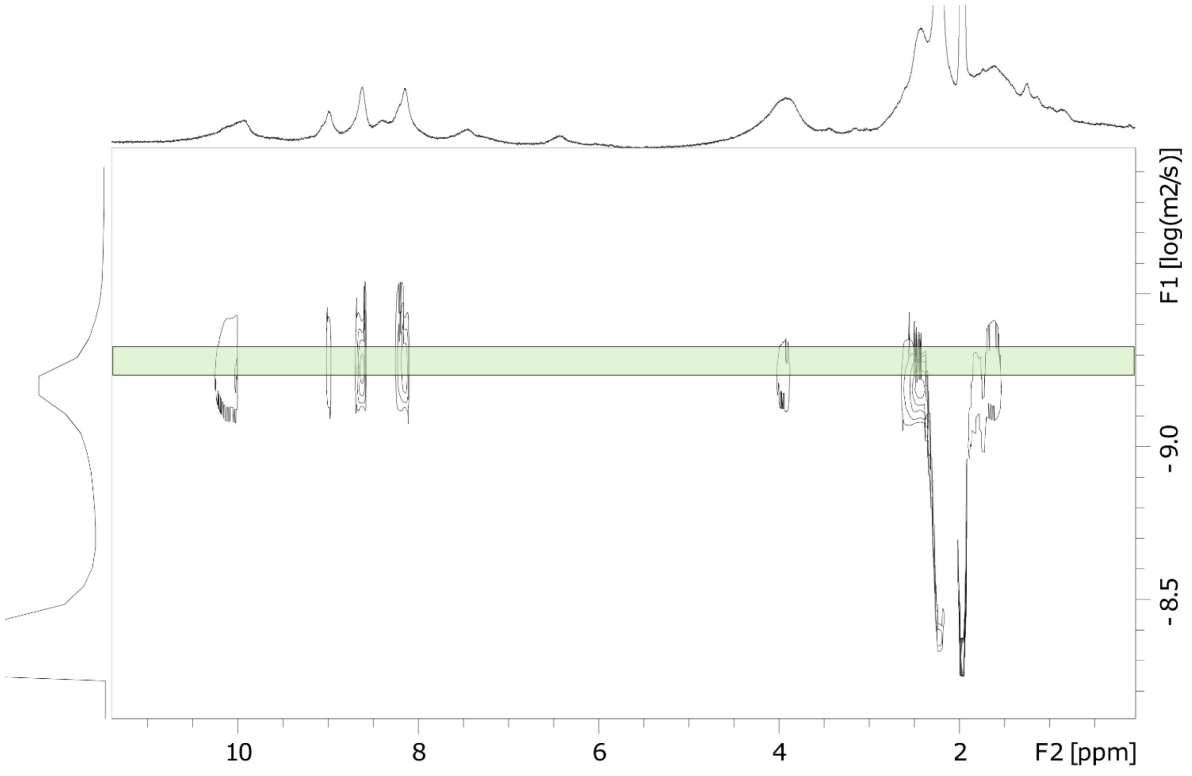

Figure S 55. 2D ^{1}H DOSY (298 K) of **$(L2)_2$@Fe_4(Zn-L)$_6$** in CD_3CN.

Table S 9. Different charged species observed in the CSI mass spectrum of the host-guest complex **$(L2)_2$@Fe_4(Zn-L)$_6$** (and the corresponding found and calculated [m/z].

Species	Charge	Found [m/z]	Calculated [m/z]
$Fe_4(Zn\text{-}L)_6(L2)_2(OTf)_0$	8+	770.7598	770.7582
$Fe_4(Zn\text{-}L)_6(L2)_2(OTf)_1$	7+	902.2890	902.1454
$Fe_4(Zn\text{-}L)_6(L2)_2(OTf)_2$	6+	1077.4950	1077.4951
$Fe_4(Zn\text{-}L)_6(L2)_2(OTf)_3$	5+	1322.7839	1322.7846
$Fe_4(Zn\text{-}L)_6(L2)_2(OTf)_4$	4+	1690.7164	1690.7188
$Fe_4(Zn\text{-}L)_6(L2)_2(OTf)_5$	3+	2303.9420	2303.9426

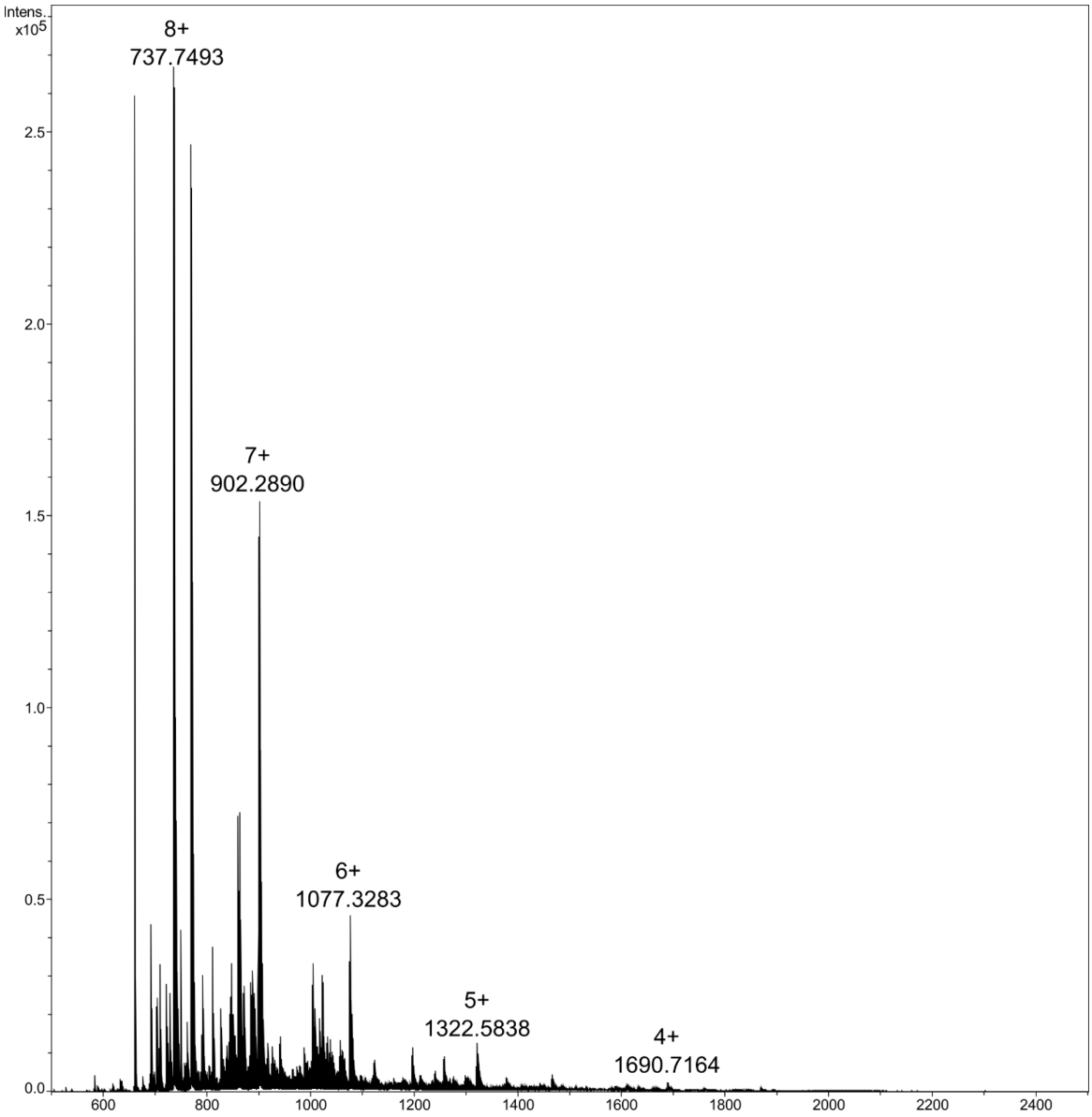

Figure S 56. CSI mass spectrum (full spectrum) of the host-guest complex **$(L2)_2$@Fe_4(Zn-L)$_6$** with a spray temperature of -40 °C and a dry gas temperature of -35 °C.

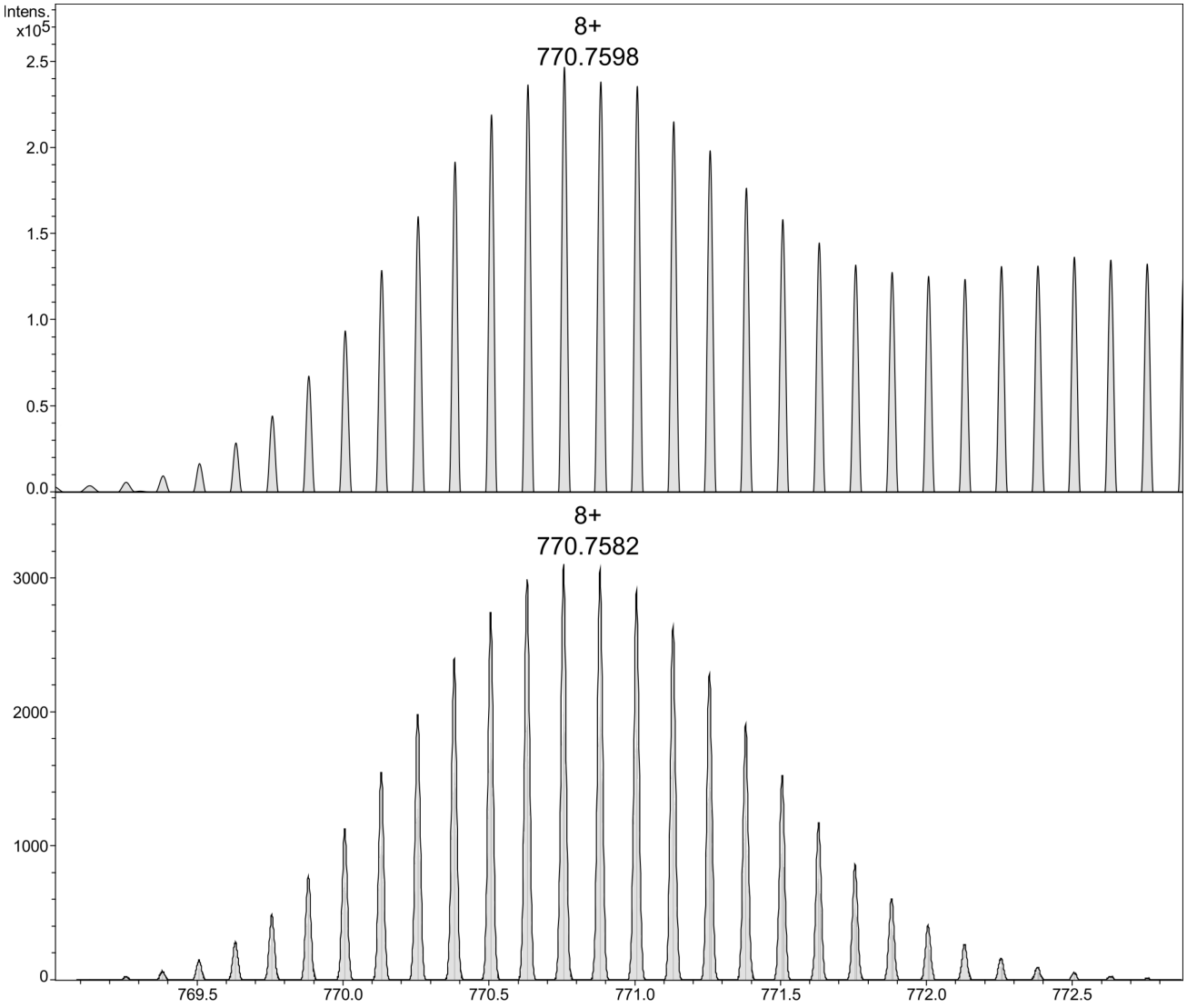

Figure S 57. Expanded spectrum for the charged species $[Fe_4(Zn\text{-}L)_6(L2)_2(OTf)_0]^{8+}$ observed (above) in the CSI mass spectrum of the host-guest complex **$(L2)_2$@Fe_4(Zn-L)$_6$** and simulated isotopic distribution (below). The shoulder on the observed signal belongs to the same species with an oxidized phosphine.

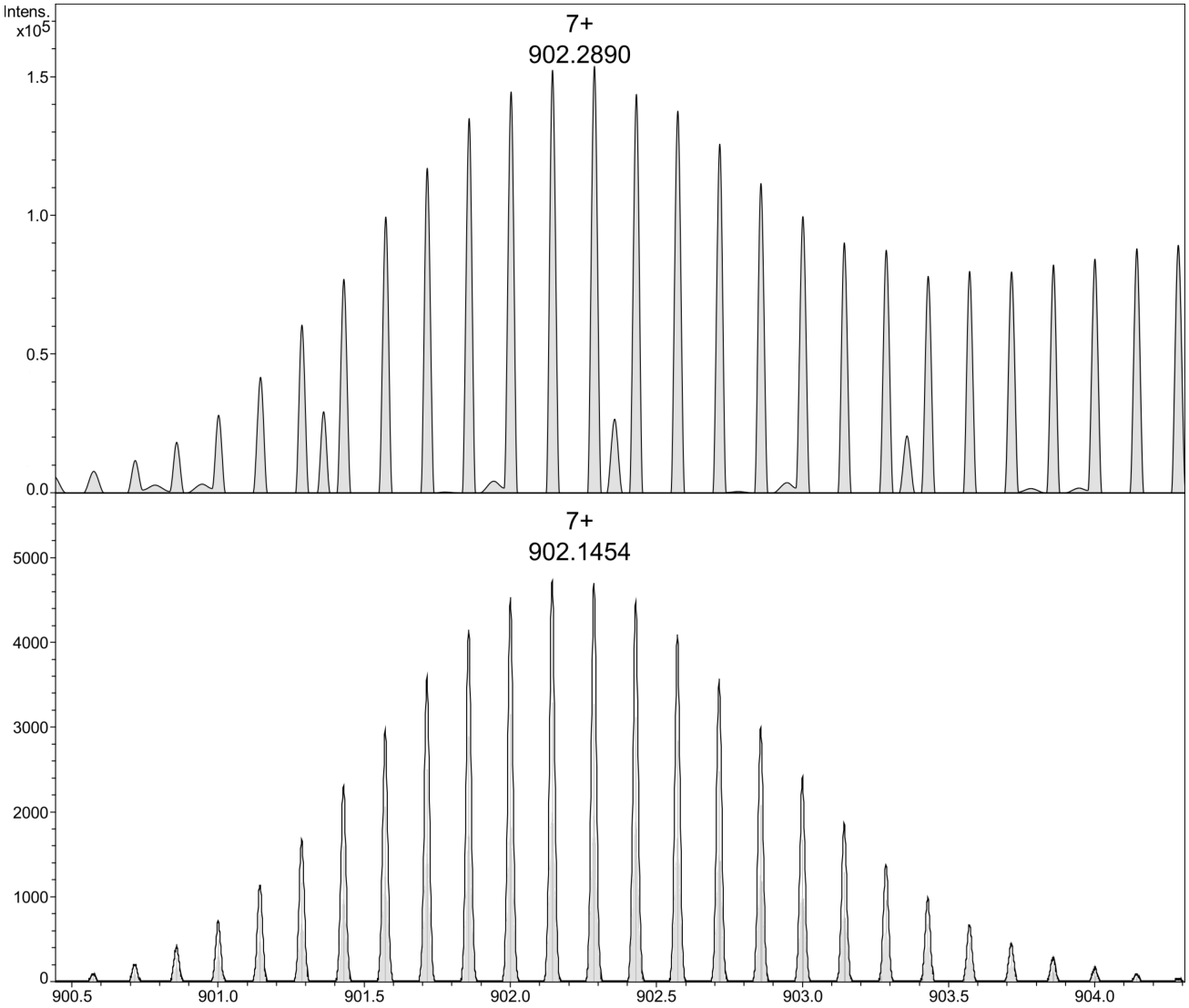

Figure S 58. Expanded spectrum for the charged species $[Fe_4(Zn\text{-}L)_6(L2)_2(OTf)_1]^{7+}$ observed (above) in the CSI mass spectrum of the host-guest complex **$(L2)_2$@Fe_4(Zn-L)$_6$** and simulated isotopic distribution (below). The shoulder on the observed signal belongs to the same species with an oxidized phosphine.

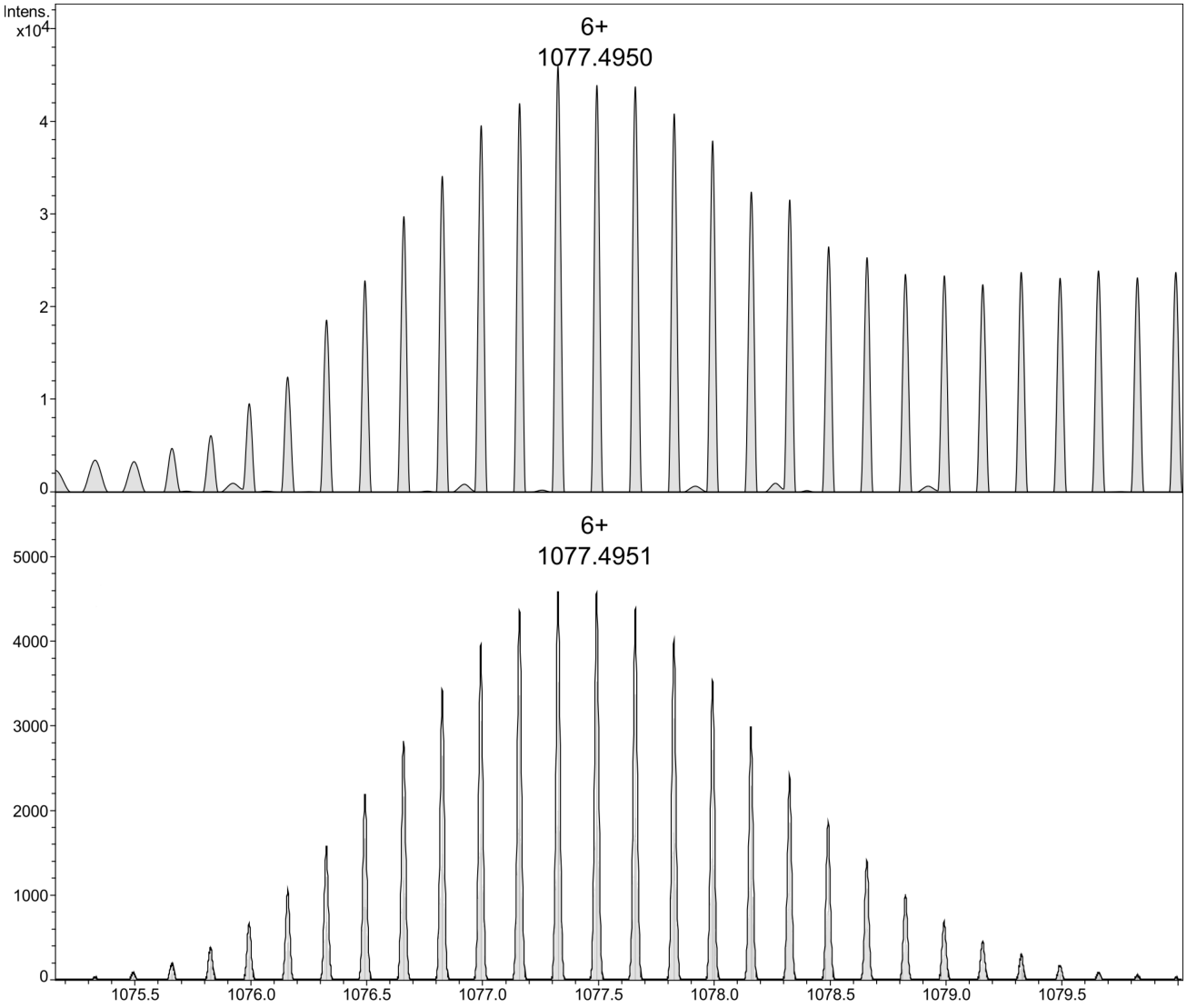

Figure S 59. Expanded spectrum for the charged species $[Fe_4(Zn\text{-}L)_6(L2)_2(OTf)_2]^{6+}$ observed (above) in the CSI mass spectrum of the host-guest complex **$(L2)_2$@Fe_4(Zn-L)$_6$** and simulated isotopic distribution (below). The shoulder on the observed signal belongs to the same species with an oxidized phosphine.

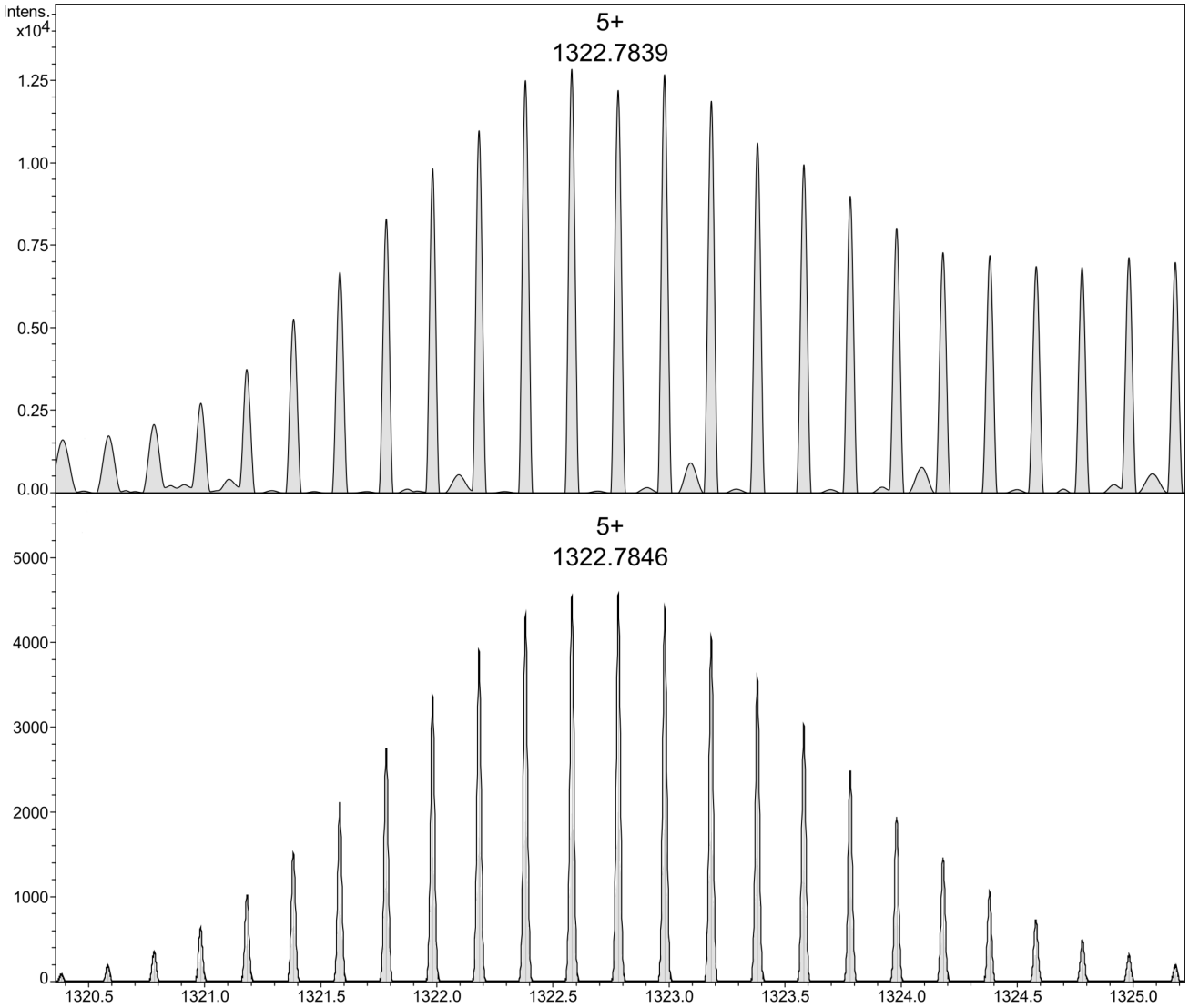

Figure S 60. Expanded spectrum for the charged species $[Fe_4(Zn\text{-}L)_6(L2)_2(OTf)_3]^{5+}$ observed (above) in the CSI mass spectrum of the host-guest complex **$(L2)_2$@Fe_4(Zn-L)$_6$** and simulated isotopic distribution (below). The shoulder on the observed signal belongs to the same species with an oxidized phosphine.

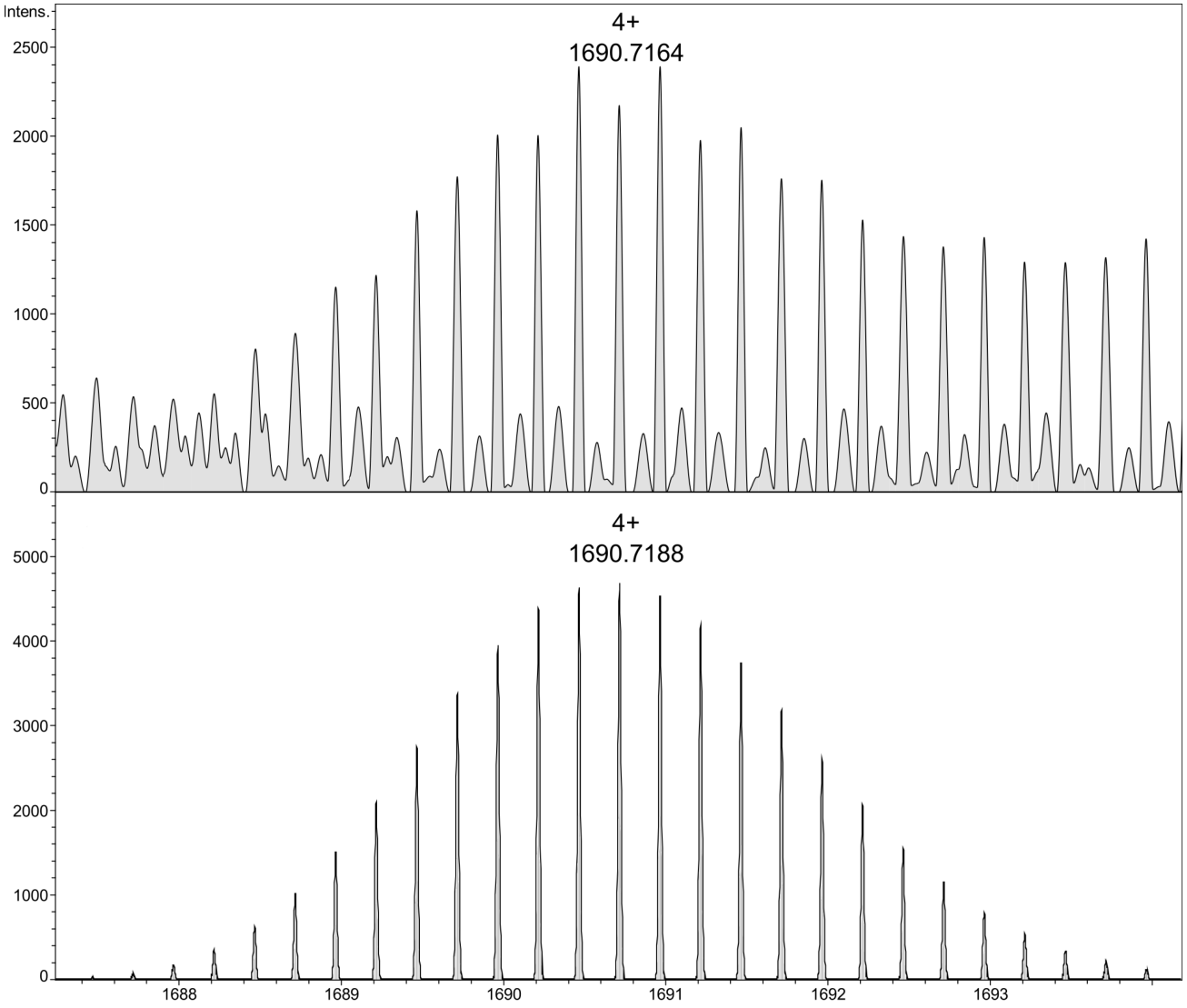

Figure S 61. Expanded spectrum for the charged species $[Fe_4(Zn\text{-}L)_6(L2)_2(OTf)_0]^{4+}$ observed (above) in the CSI mass spectrum of the host-guest complex **$(L2)_2$@Fe_4(Zn-L)$_6$** and simulated isotopic distribution (below). The shoulder on the observed signal belongs to the same species with an oxidized phosphine.

Encapsulation study of $Fe_4(Zn\text{-}L)_6$ and L3

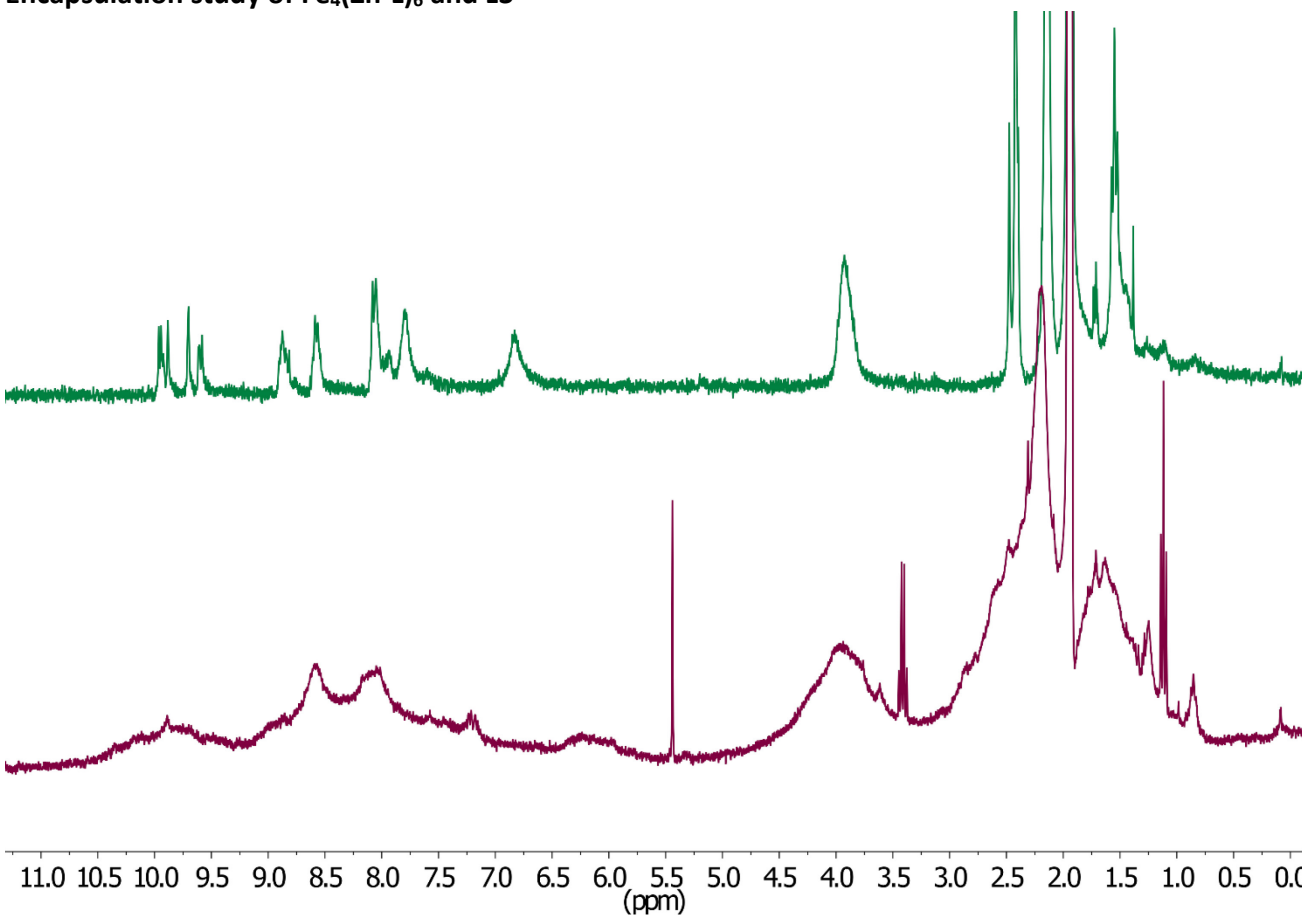

Figure S 62. ^{1}H NMR (300 MHz, 298 K) of **$Fe_4(Zn\text{-}L)_6$** (top) and **$(L3)_2@Fe_4(Zn\text{-}L)_6$** (bottom) in CD_3CN.

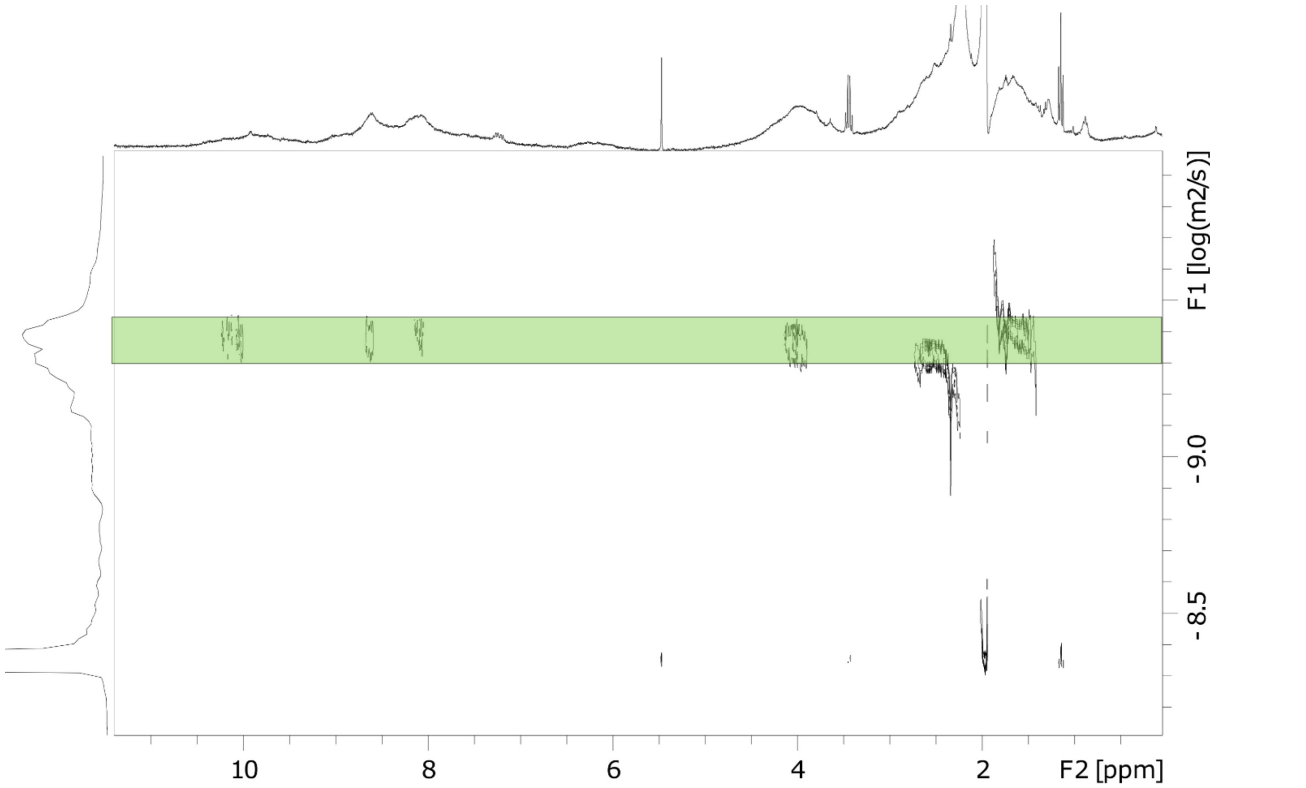

Figure S 63. 2D ^{1}H DOSY (298 K) of **$(L3)_2@Fe_4(Zn\text{-}L)_6$** in CD_3CN.

Table S 10. Different charged species observed in the CSI mass spectrum of the host-guest complex **$(L3)_2$@Fe_4(Zn-L)$_6$** and the corresponding found and calculated [m/z].

Species	Charge	Found [m/z]	Calculated [m/z]
$Fe_4(Zn\text{-}L)_6(L3)_2(OTf)_0$	8+	771.0083	771.0070
$Fe_4(Zn\text{-}L)_6(L3)_2(OTf)_1$	7+	902.5731	902.4298
$Fe_4(Zn\text{-}L)_6(L3)_2(OTf)_2$	6+	1077.8261	1077.8268
$Fe_4(Zn\text{-}L)_6(L3)_2(OTf)_3$	5+	1323.1816	1323.1826
$Fe_4(Zn\text{-}L)_6(L3)_2(OTf)_4$	4+	1691.2128	1691.2164

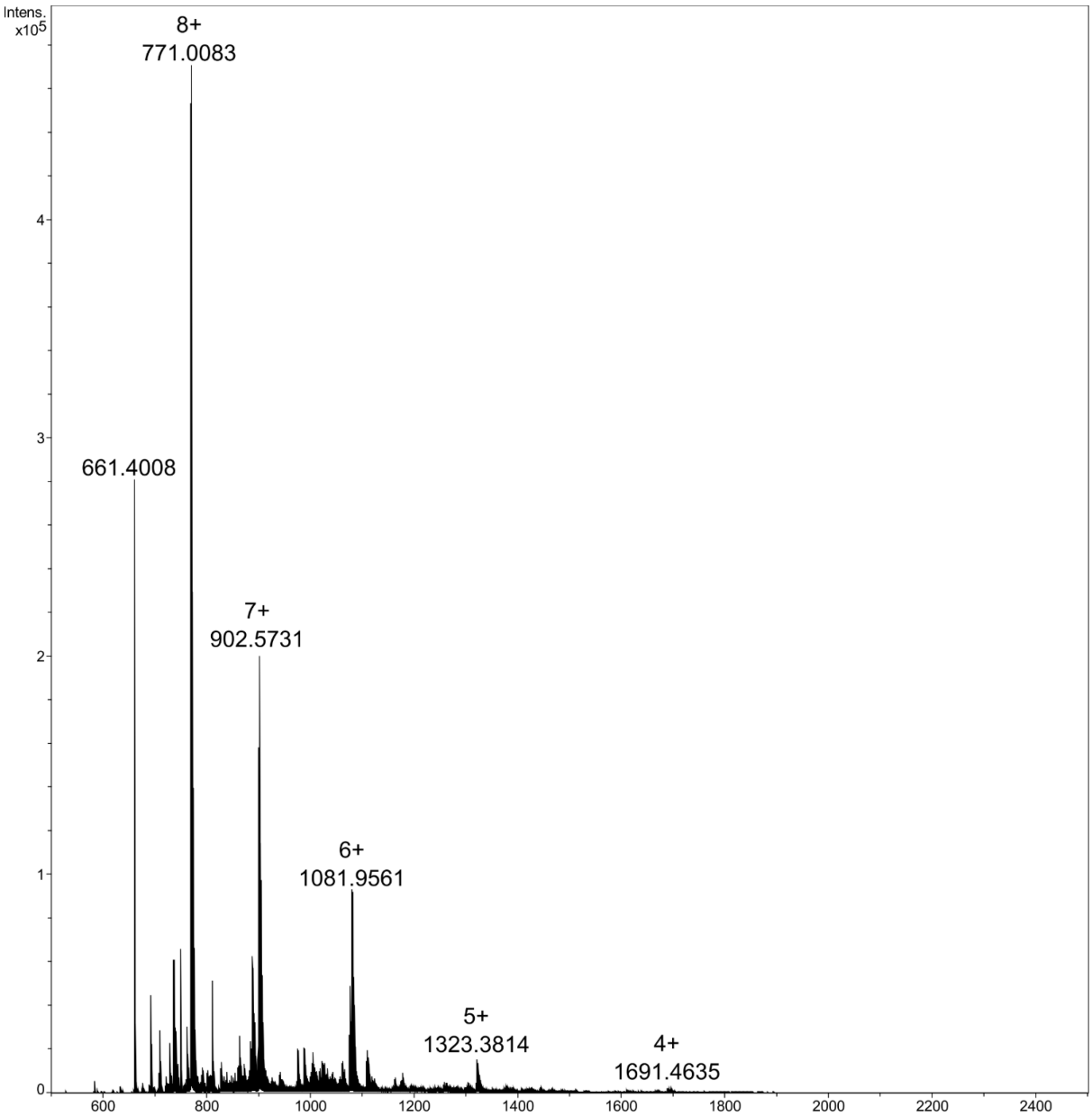

Figure S 64. CSI mass spectrum (full spectrum) of the host-guest complex **$(L3)_2$@Fe_4(Zn-L)$_6$** with a spray temperature of -40 °C and a dry gas temperature of -35 °C. The peak with m/z ratio of 661 belongs to demetallated **Zn-P**.

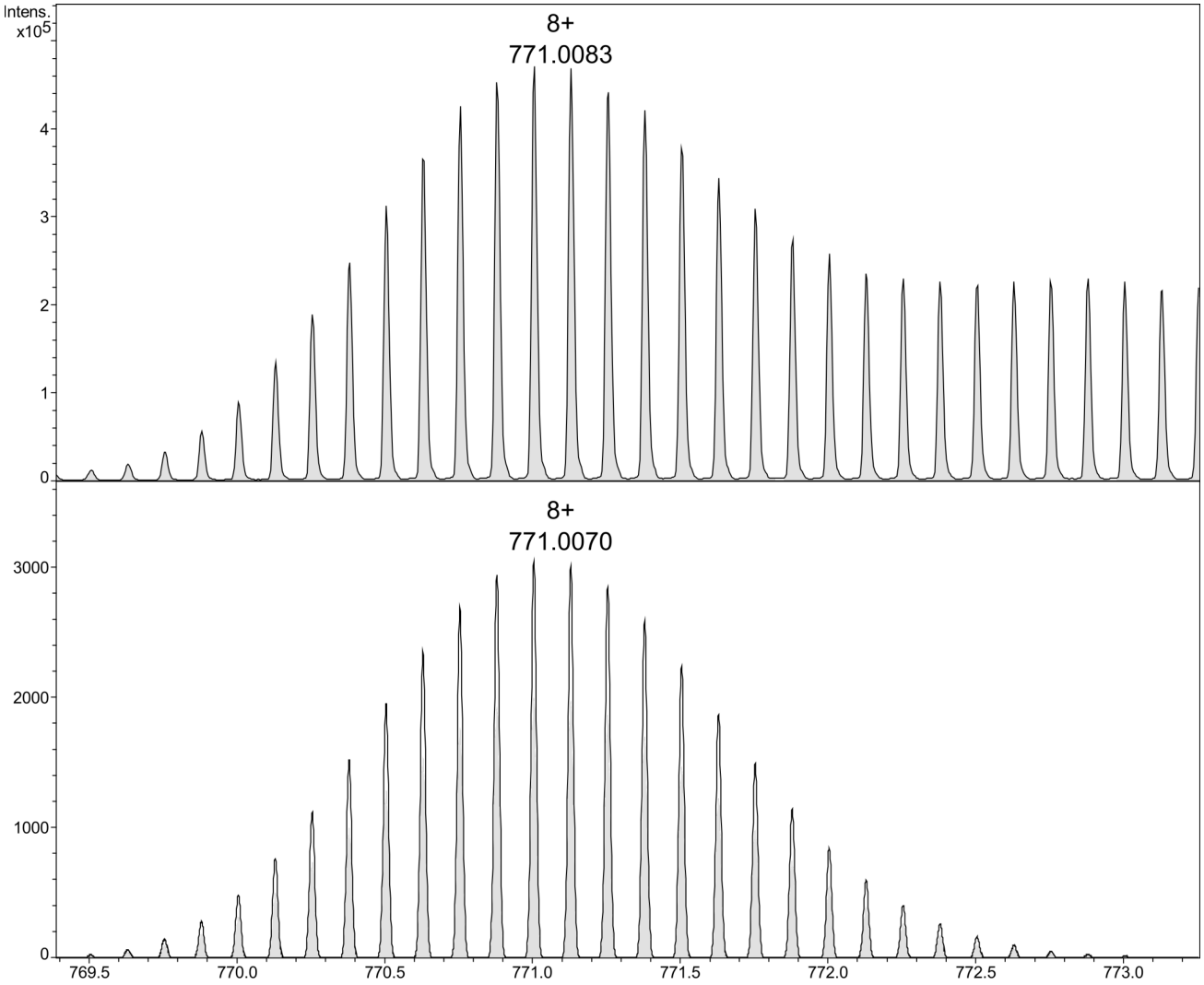

Figure S 65. Expanded spectrum for the charged species $[Fe_4(Zn\text{-}L)_6(L3)_2(OTf)_0]^{8+}$ observed (above) in the CSI mass spectrum of the host-guest complex **$(L3)_2$@Fe_4(Zn-L)$_6$** and simulated isotopic distribution (below). The shoulder on the observed signal belongs to the same species with an oxidized phosphine.

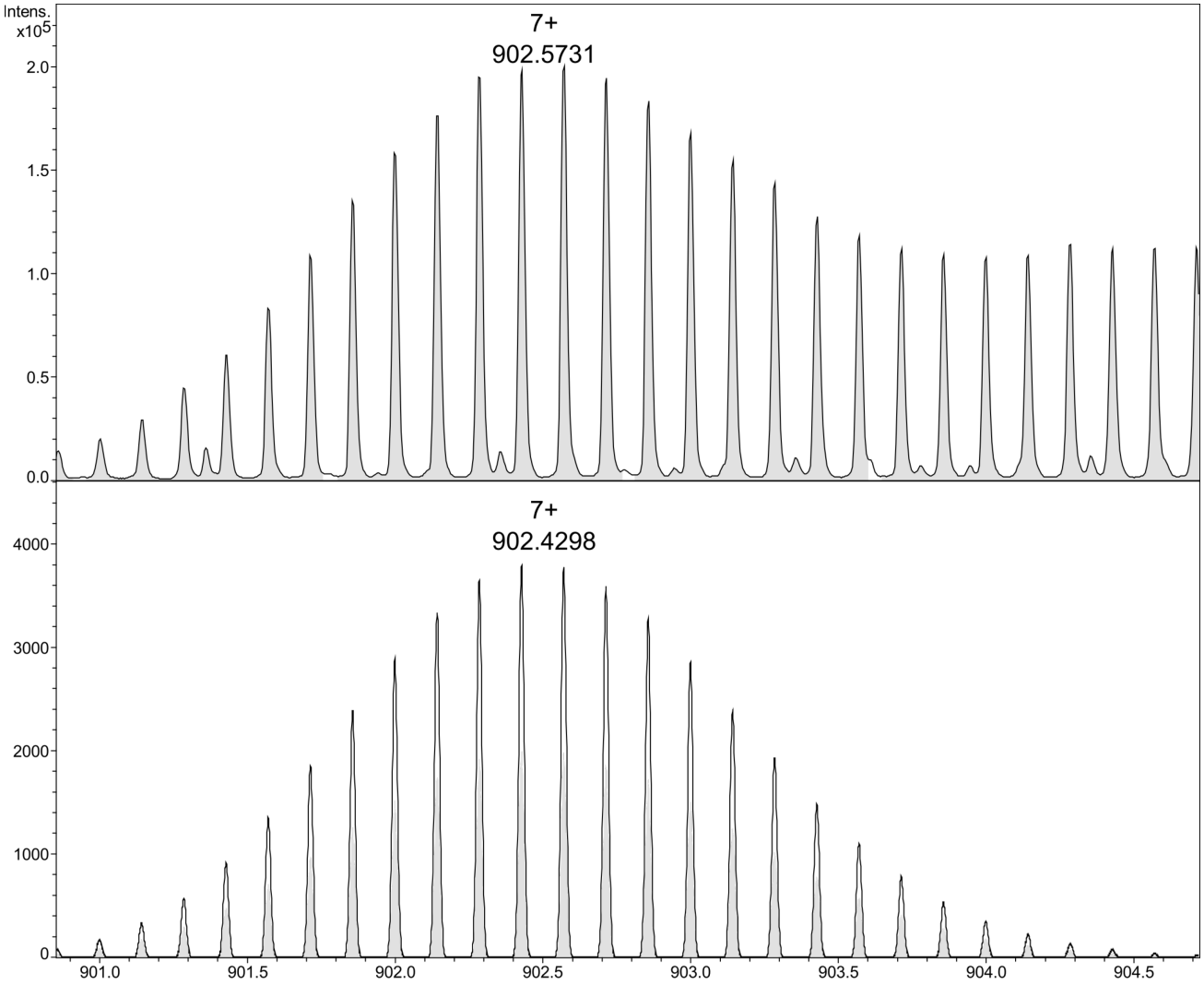

Figure S 66. Expanded spectrum for the charged species $[Fe_4(Zn\text{-}L)_6(L3)_2(OTf)_1]^{7+}$ observed (above) in the CSI mass spectrum of the host-guest complex **$(L3)_2$@Fe_4(Zn-L)$_6$** and simulated isotopic distribution (below). The shoulder on the observed signal belongs to the same species with an oxidized phosphine.

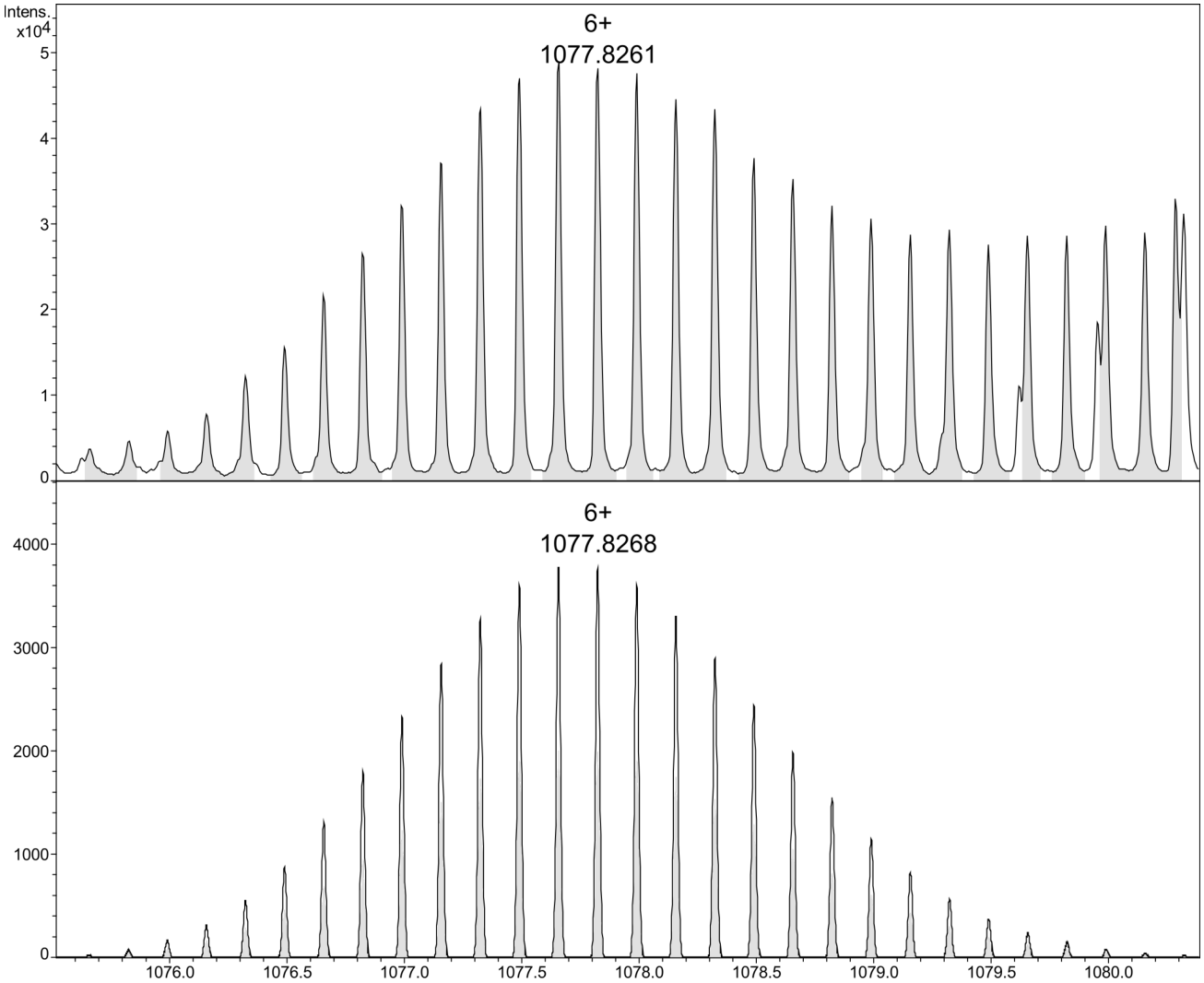

Figure S 67. Expanded spectrum for the charged species $[Fe_4(Zn\text{-}L)_6(L3)_2(OTf)_2]^{6+}$ observed (above) in the CSI mass spectrum of the host-guest complex **$(L3)_2$@Fe_4(Zn-L)$_6$** and simulated isotopic distribution (below). The shoulder on the observed signal belongs to the same species with an oxidized phosphine.

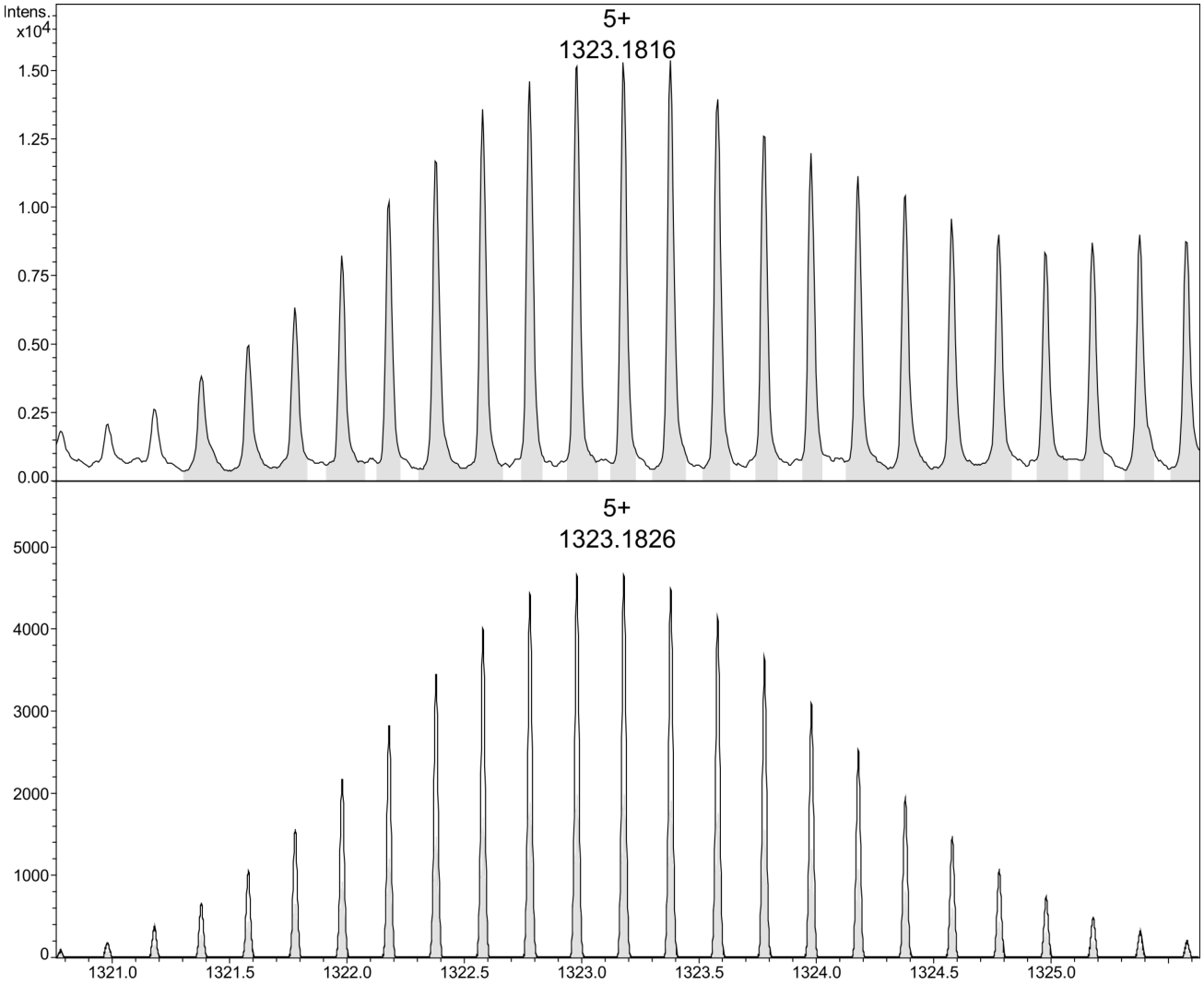

Figure S 68. Expanded spectrum for the charged species $[Fe_4(Zn\text{-}L)_6(L3)_2(OTf)_3]^{5+}$ observed (above) in the CSI mass spectrum of the host-guest complex **$(L3)_2$@Fe_4(Zn-L)$_6$** and simulated isotopic distribution (below). The shoulder on the observed signal belongs to the same species with an oxidized phosphine.

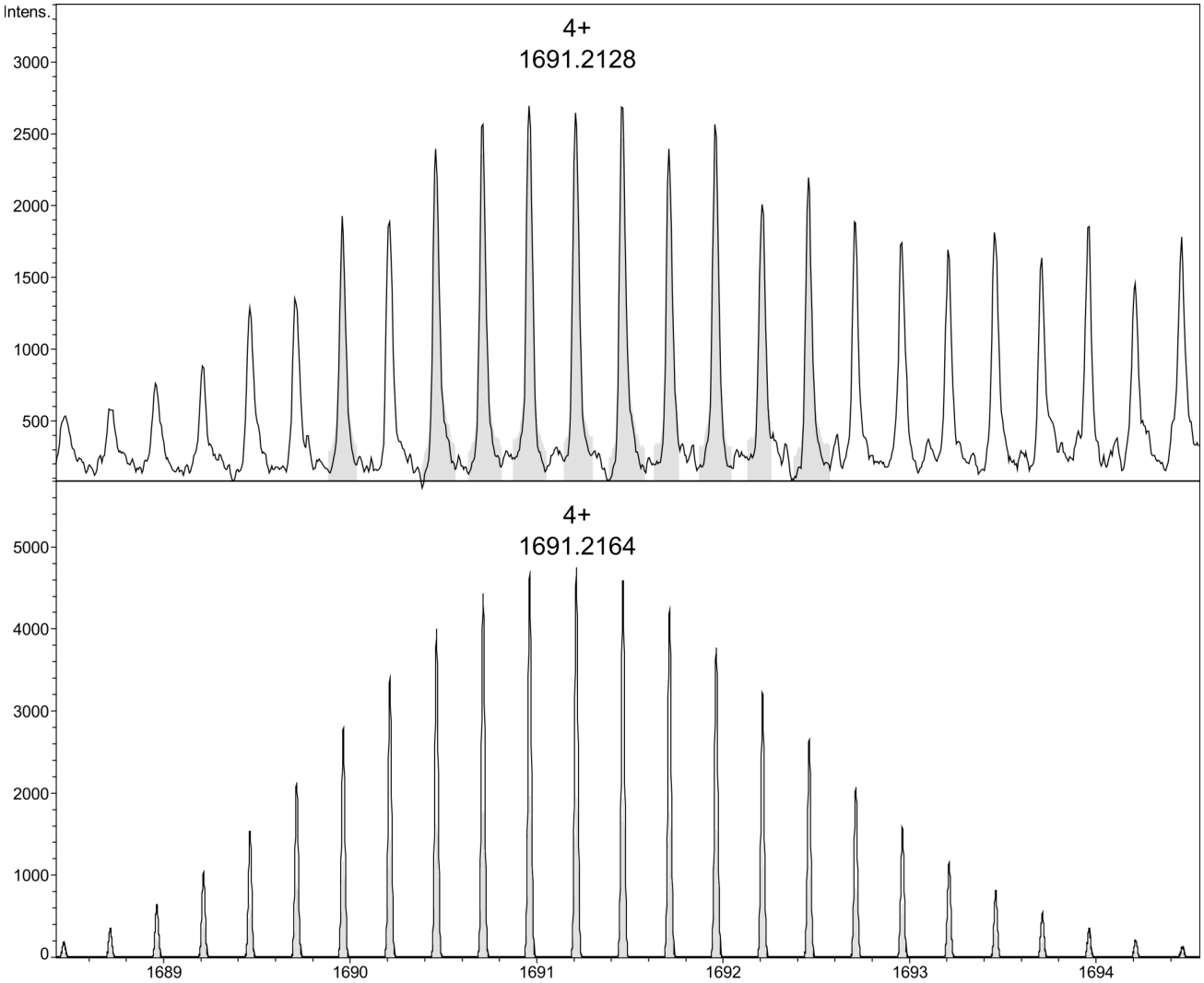

Figure S 69. Expanded spectrum for the charged species $[Fe_4(Zn\text{-}L)_6(L3)_2(OTf)_4]^{4+}$ observed (above) in the CSI mass spectrum of the host-guest complex **$(L3)_2$@Fe_4(Zn-L)$_6$** and simulated isotopic distribution (below). The shoulder on the observed signal belongs to the same species with an oxidized phosphine.

Encapsulation study of $Fe_4(Zn\text{-}L)_6$ and PPh_3

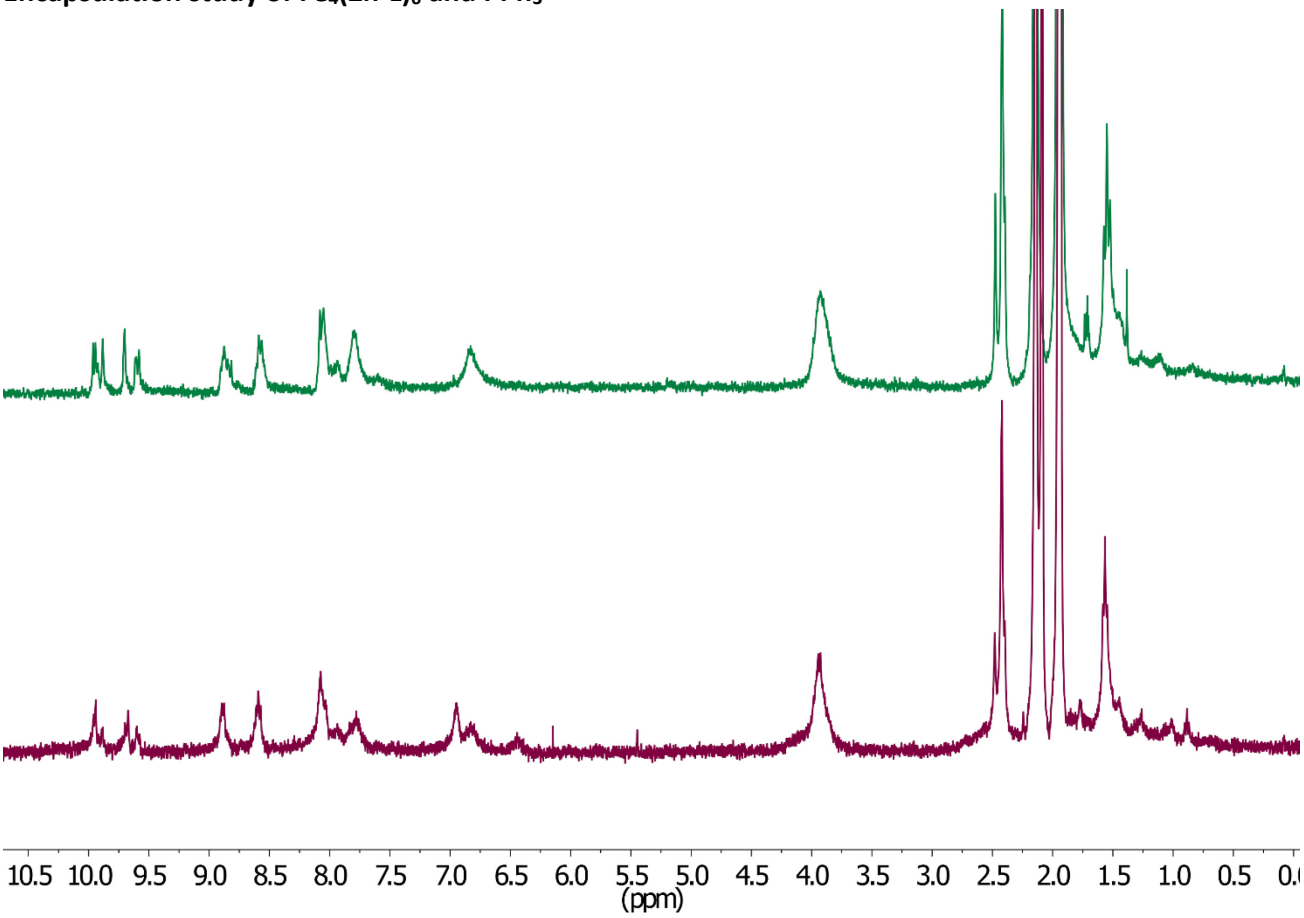

Figure S 70. ^{1}H NMR (400 MHz, 298 K) of **$Fe_4(Zn\text{-}L)_6$** (top) and a mixture of **PPh_3** and **$Fe_4(Zn\text{-}L)_6$** (bottom) in CD_3CN.

Encapsulation study of $Fe_4(Zn\text{-}L)_6$ and Au1

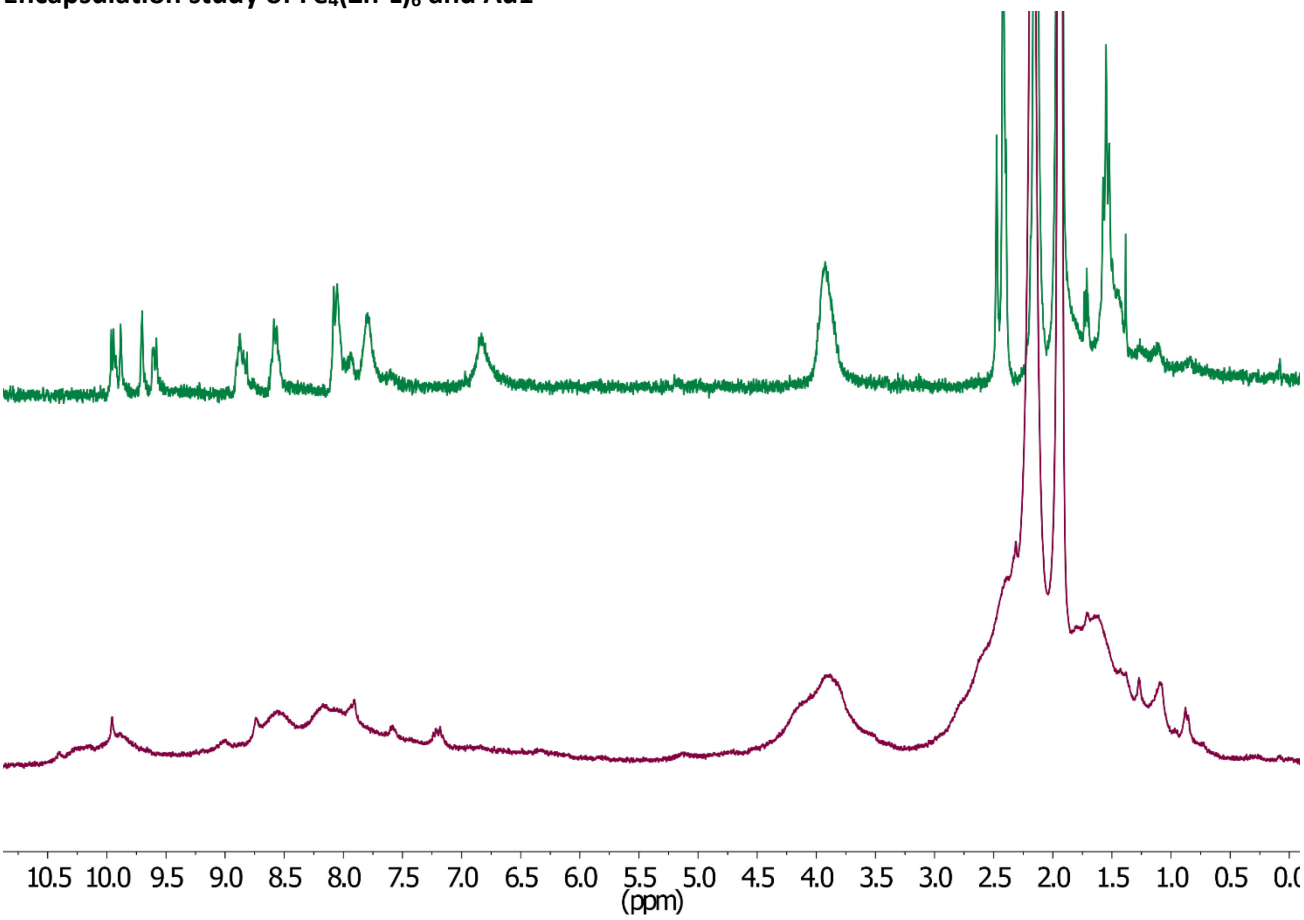

Figure S 71. ^{1}H NMR (300 MHz, 298 K) of **$Fe_4(Zn\text{-}L)_6$** (top) and **Au1@$Fe_4(Zn\text{-}L)_6$** (bottom) in CD_3CN.

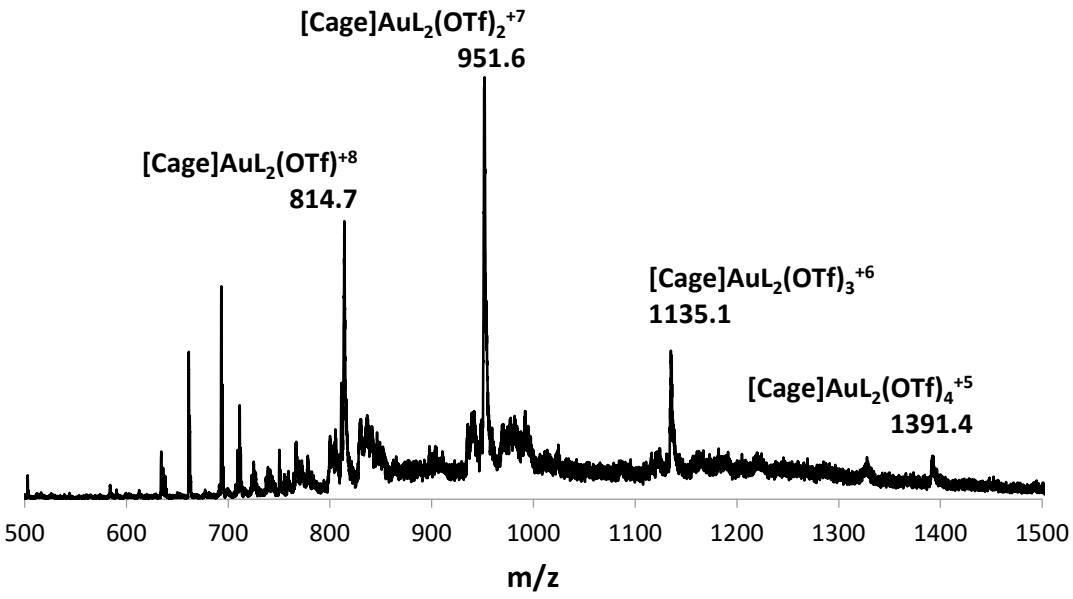

Figure S 72. ESI-MS spectrum of **Au1@$Fe_4(Zn\text{-}L)_6$**. In the image **L** = **L3**.

9. Formation and characterization of the active species

Encapsulation study of $Fe_4(Zn\text{-}L)_6$ and Rh4 complex

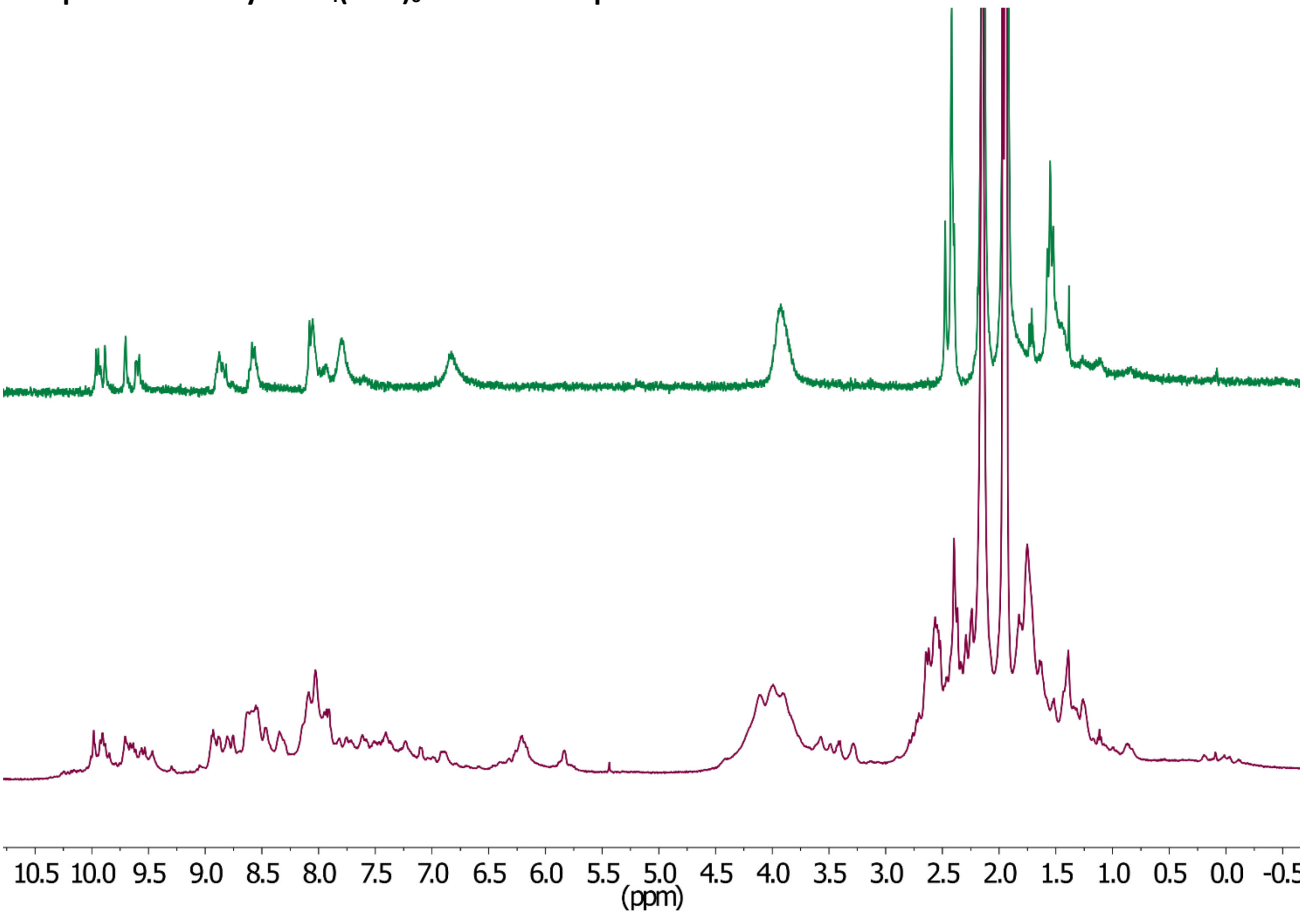

Figure S 73. ^{1}H NMR (500 MHz, 298 K) of **$Fe_4(Zn\text{-}L)_6$** (top) and **Rh4@$Fe_4(Zn\text{-}L)_6$** (bottom) in CD_3CN. The bottom spectrum contains a 1:2:1 mixture of $Rh(acac)(CO)_2$, **L3** and **$Fe_4(Zn\text{-}L)_6$**.

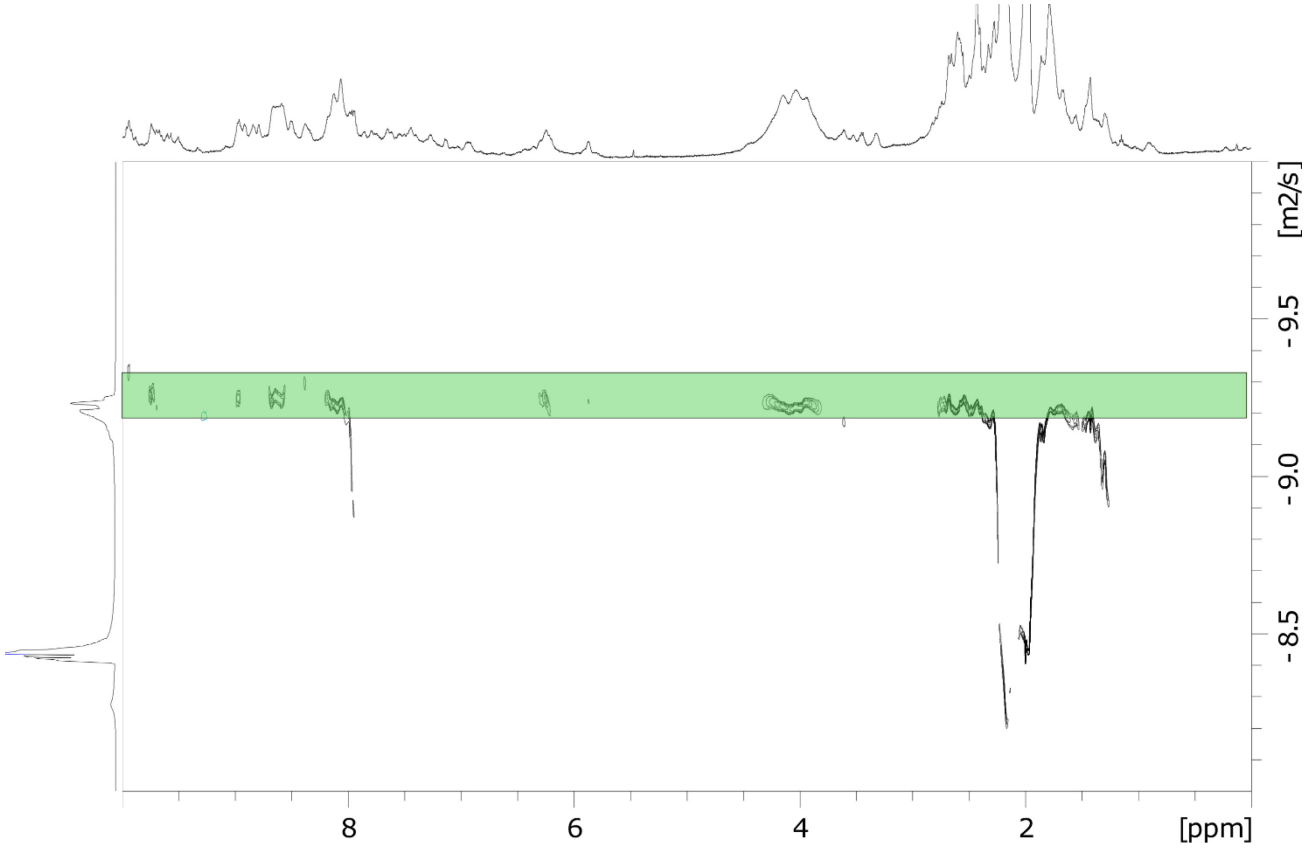

Figure S 74. ^{1}H NMR (298 K) of **Fe_4(Zn-L)$_6$** (top) and **Rh4@Fe_4(Zn-L)$_6$** (bottom) in CD_3CN. The spectrum contains a 1:2:1 mixture of Rh(acac)$(CO)_2$, **L3** and **Fe_4(Zn-L)$_6$**.

Table S 11. Different charged species observed in the CSI mass spectrum of the host-guest complex **Rh4@Fe_4(Zn-L)$_6$** and the corresponding found and calculated [m/z].

Species	Charge	Found [m/z]	Calculated [m/z]
$Fe_4(Zn\text{-}L)_6(Rh)_1(L3)_2(CO)_1(Cl)_1(OTf)_0$	8+	791.8678	791.8656
$Fe_4(Zn\text{-}L)_6(Rh)_1(L3)_2(CO)_1(Cl)_1(OTf)_1$	7+	926.2679	926.2681
$Fe_4(Zn\text{-}L)_6(Rh)_1(L3)_2(CO)_1(Cl)_1(OTf)_3$	5+	1356.3585	1356.3564
$Fe_4(Zn\text{-}L)_6(Rh)_1(L3)_2(CO)_1(Cl)_1(OTf)_4$	4+	1732.6842	1732.6836

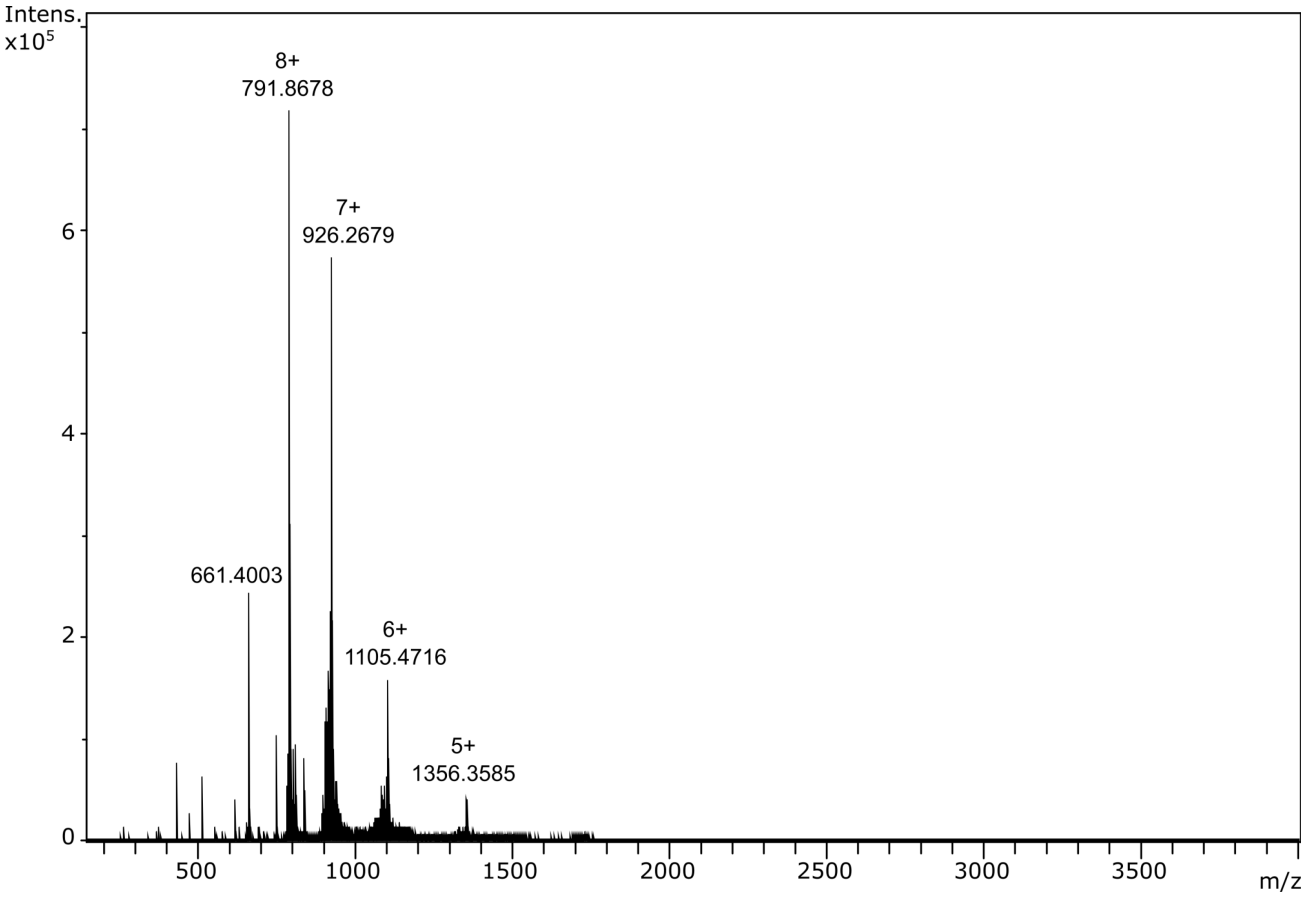

Figure S 75. CSI mass spectrum (full spectrum) of the host-guest complex **Rh4@Fe$_4$(Zn-L)$_6$** with a spray temperature of -40 °C and a dry gas temperature of -35 °C. The peak with m/z ratio of 661 belongs to demetallated **Zn-P**.

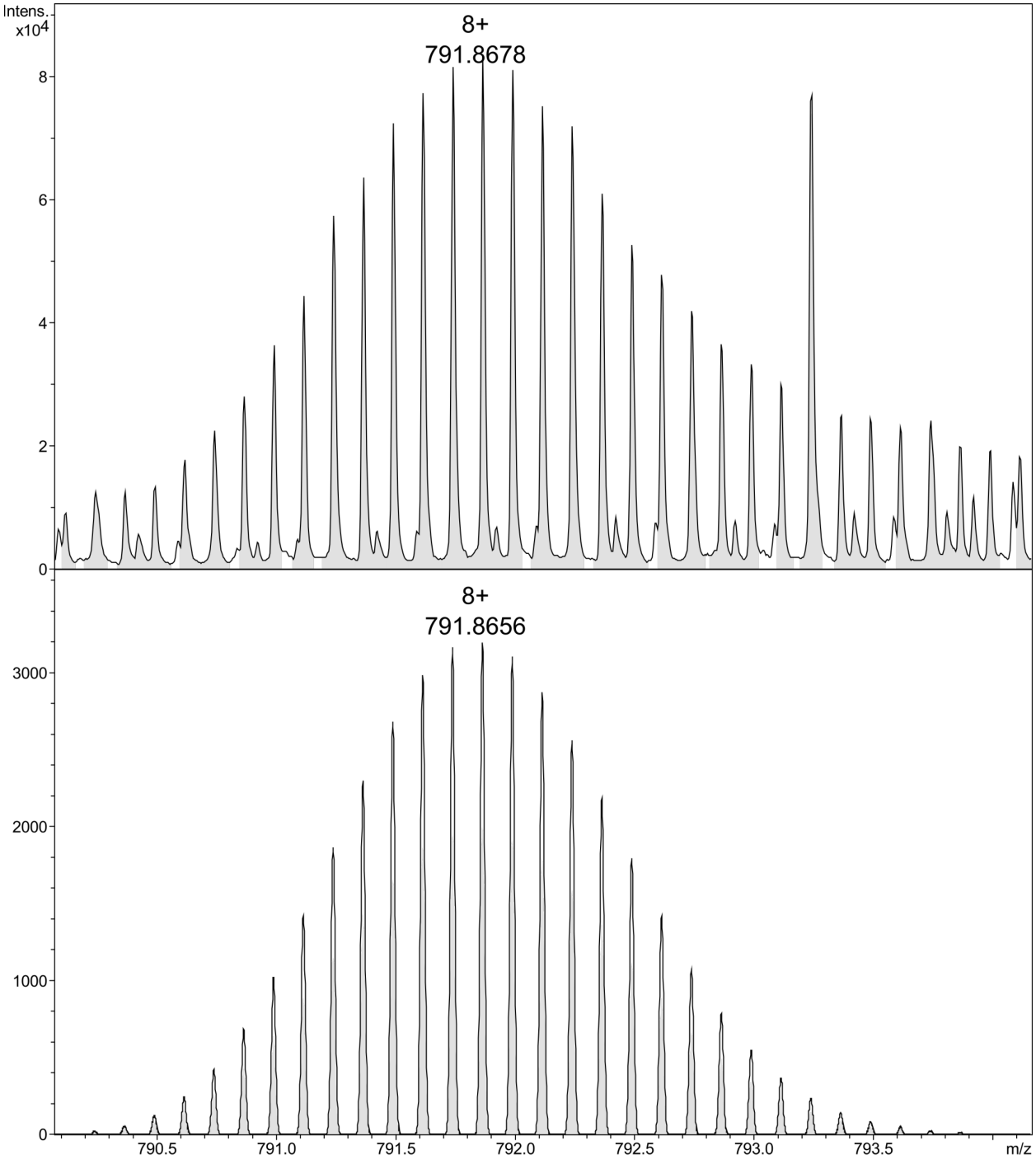

Figure S 76. Expanded spectrum for the charged species $[Fe_4(Zn\text{-}L)_6(Rh)_1(L3)_2(CO)_1(Cl)_1(OTf)_0]^{8+}$ observed (above) in the CSI mass spectrum of the host-guest complex **Rh4@Fe$_4$(Zn-L)$_6$** and simulated isotopic distribution (below).

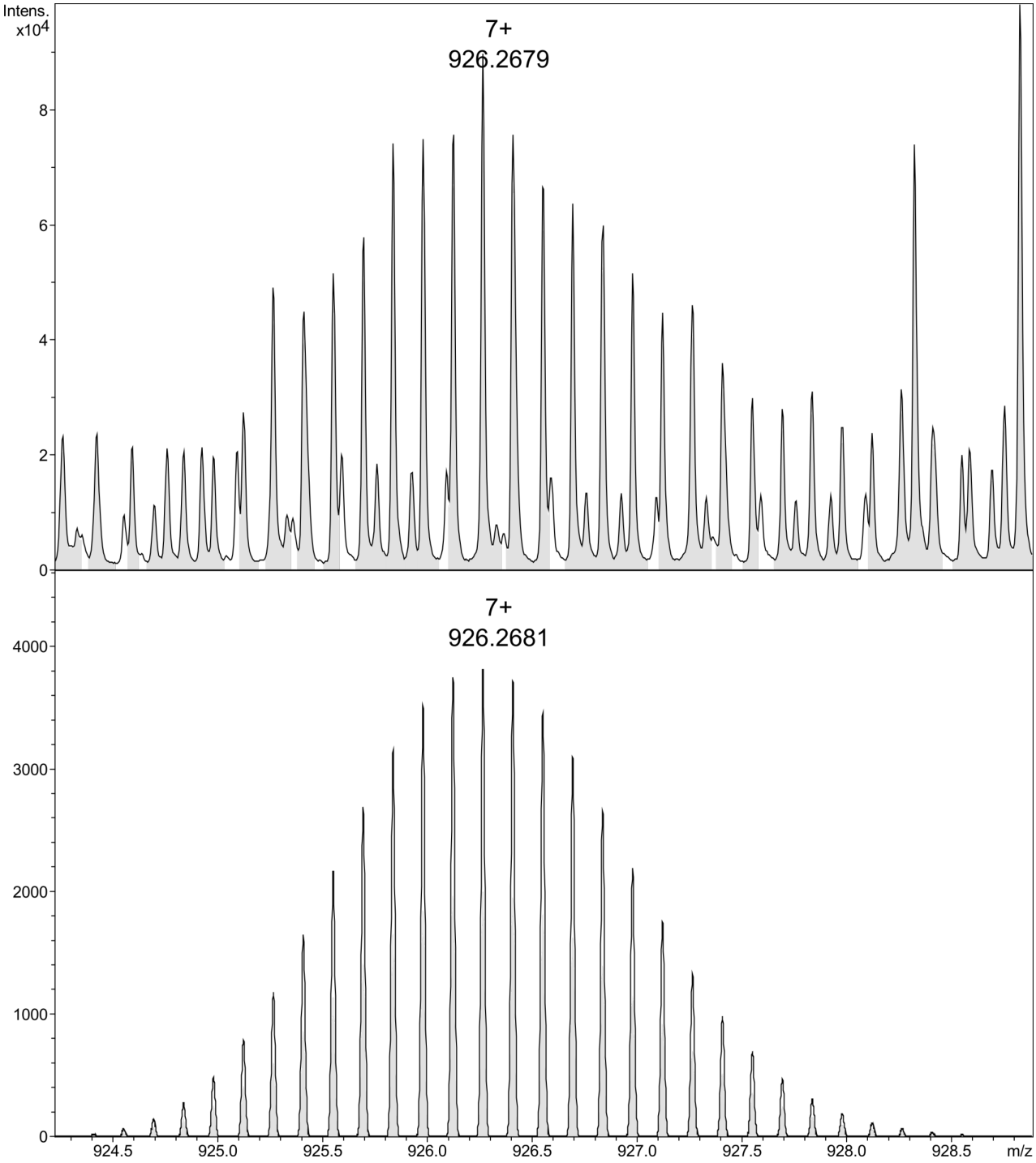

Figure S 77. Expanded spectrum for the charged species $[Fe_4(Zn\text{-}L)_6(Rh)_1(L3)_2(CO)_1(Cl)_1(OTf)_1]^{7+}$ observed (above) in the CSI mass spectrum of the host-guest complex **Rh4@Fe$_4$(Zn-L)$_6$** and simulated isotopic distribution (below).

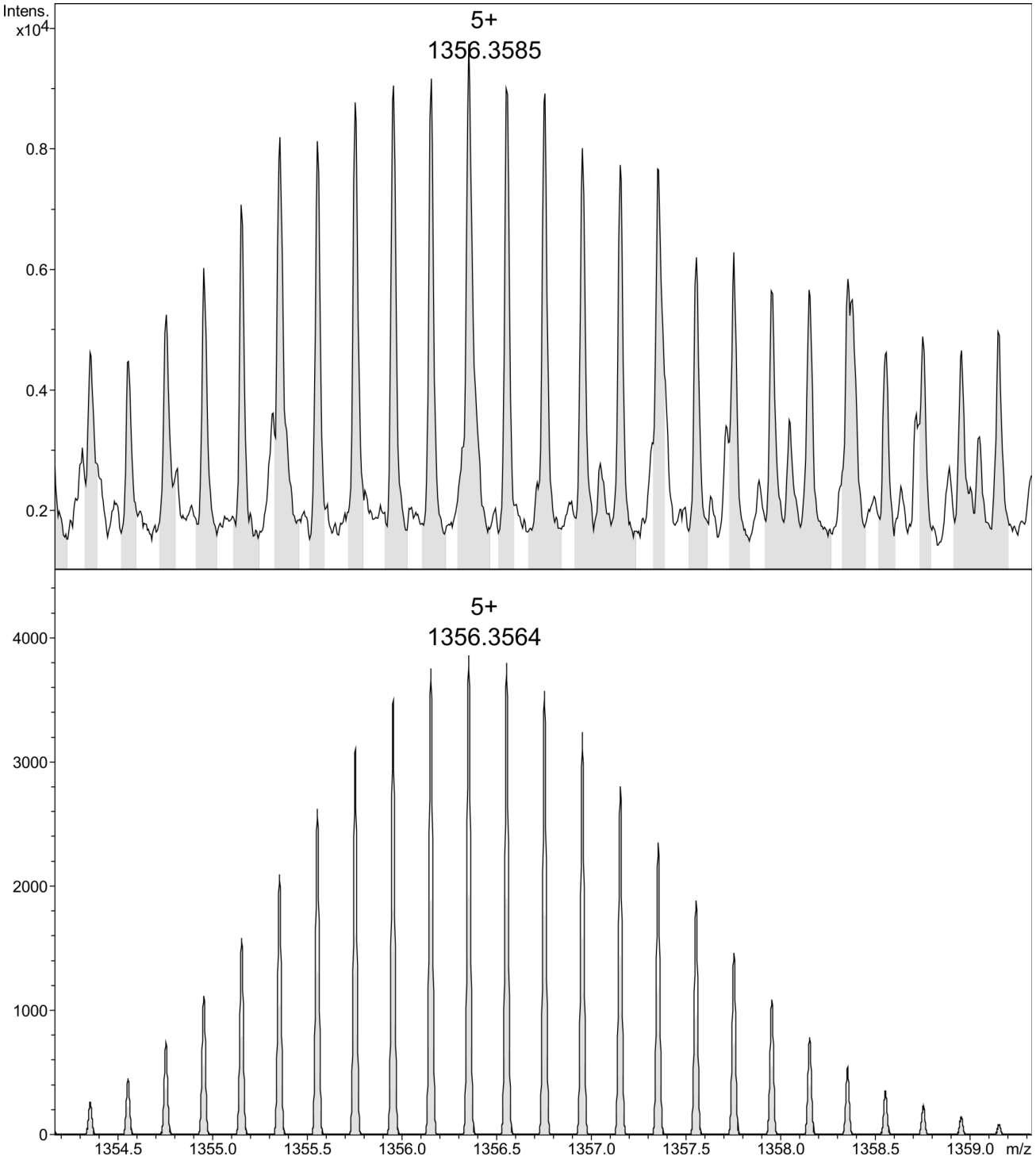

Figure S 78. Expanded spectrum for the charged species $[Fe_4(Zn\text{-}L)_6(Rh)_1(L3)_2(CO)_1(Cl)_1(OTf)_3]^{5+}$ observed (above) in the CSI mass spectrum of the host-guest complex **Rh4@Fe$_4$(Zn-L)$_6$** and simulated isotopic distribution (below).

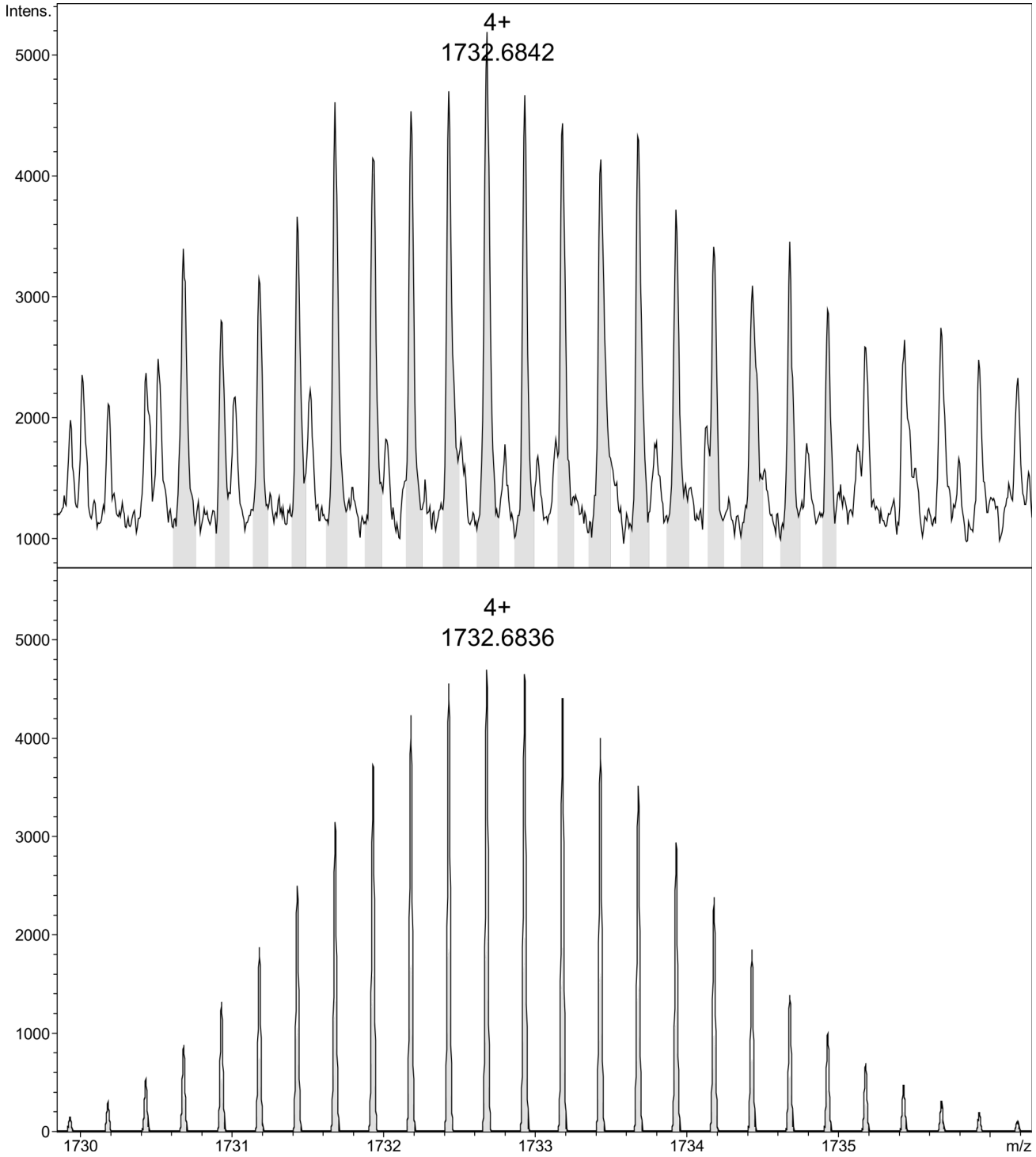

Figure S 79. Expanded spectrum for the charged species $[Fe_4(Zn\text{-}L)_6(Rh)_1(L3)_2(CO)_1(Cl)_1(OTf)_4]^{4+}$ observed (above) in the CSI mass spectrum of the host-guest complex **Rh4@Fe$_4$(Zn-L)$_6$** and simulated isotopic distribution (below).

Characterisation of the active species by ^{1}H NMR spectroscopy

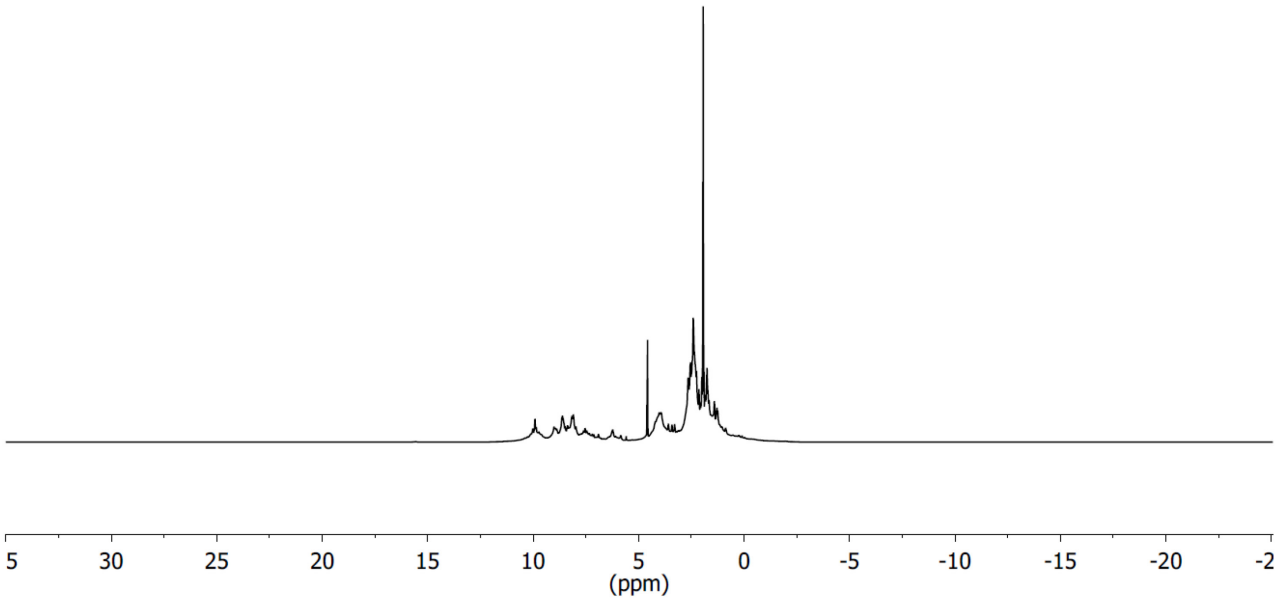

Figure S 80. High pressure ^{1}H NMR (500 MHz, 298 K, 7 bar syngas) of the active species formed from **Rh4@Fe$_4$(Zn-L)$_6$**. Hydride signals could not be detected.

Characterisation of the active species by IR spectroscopy

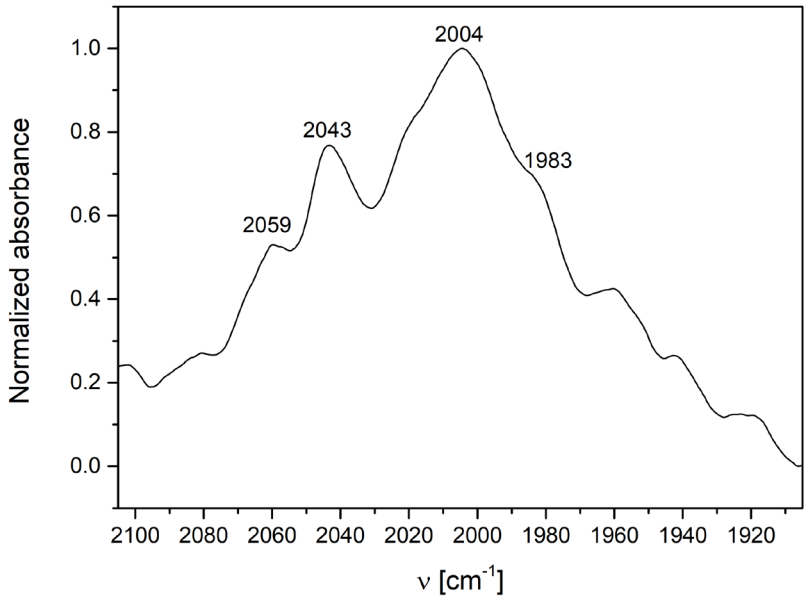

Figure S 81. IR spectrum (298 K) of a 1:2 mixture of Rh(acac)(CO)$_2$ and **L3** in acetonitrile under 20 bar syngas. [Rh] = 1.3 mM and [**L3**] = 2.6 mM.

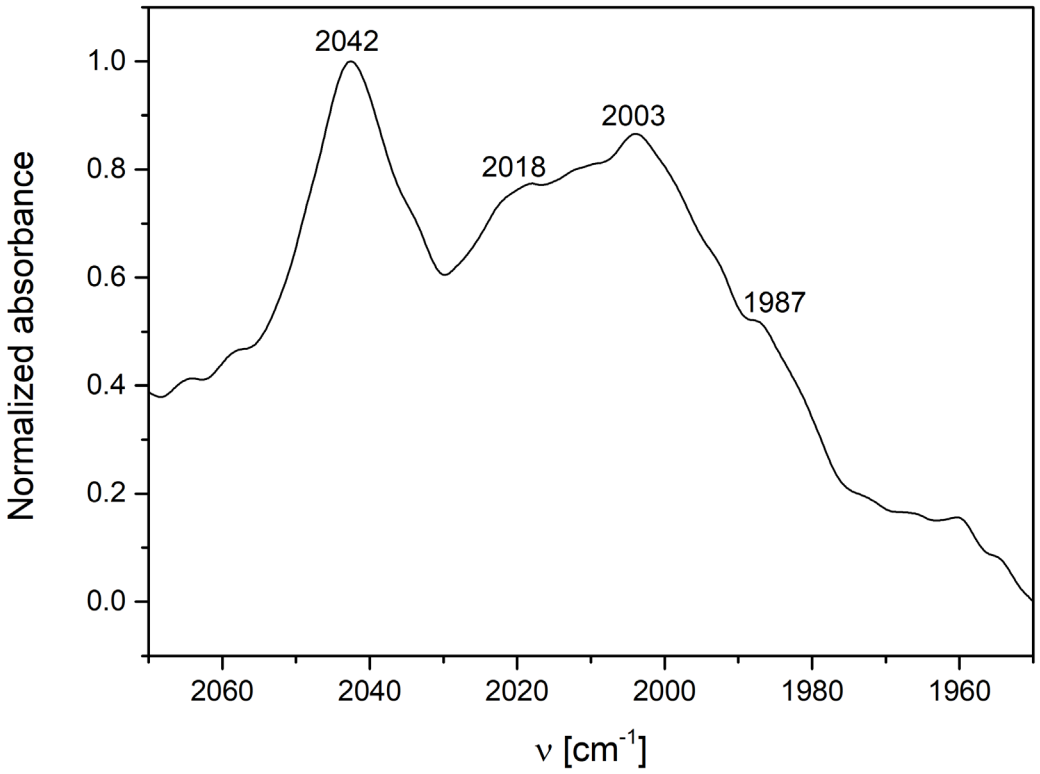

Figure S 82. IR spectrum (298 K) of a 1:2 mixture of Rh(acac)$(CO)_2$ and **L3** in a 3:2 mixture of acetonitrile and dichloromethane under 20 bar syngas. [Rh] = 1.3 mM and [**L3**] = 2.6 mM.

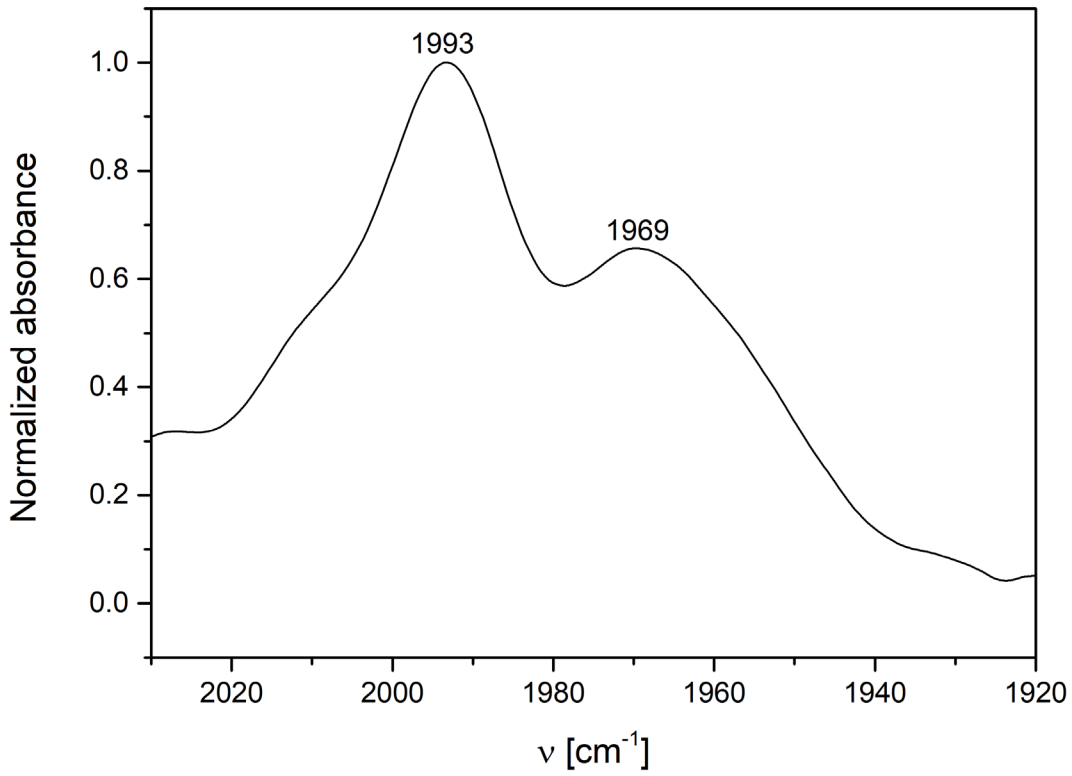

Figure S 83. IR spectrum (298 K) of a 1:2:1 mixture of Rh(acac)$(CO)_2$, **L3** and **Fe_4(Zn-L)$_6$** in a 3:2 mixture of acetonitrile and dichloromethane under 20 bar syngas. [Rh] = [**Fe_4(Zn-L)$_6$**] = 1.3 mM and [**L3**] = 2.6 mM.

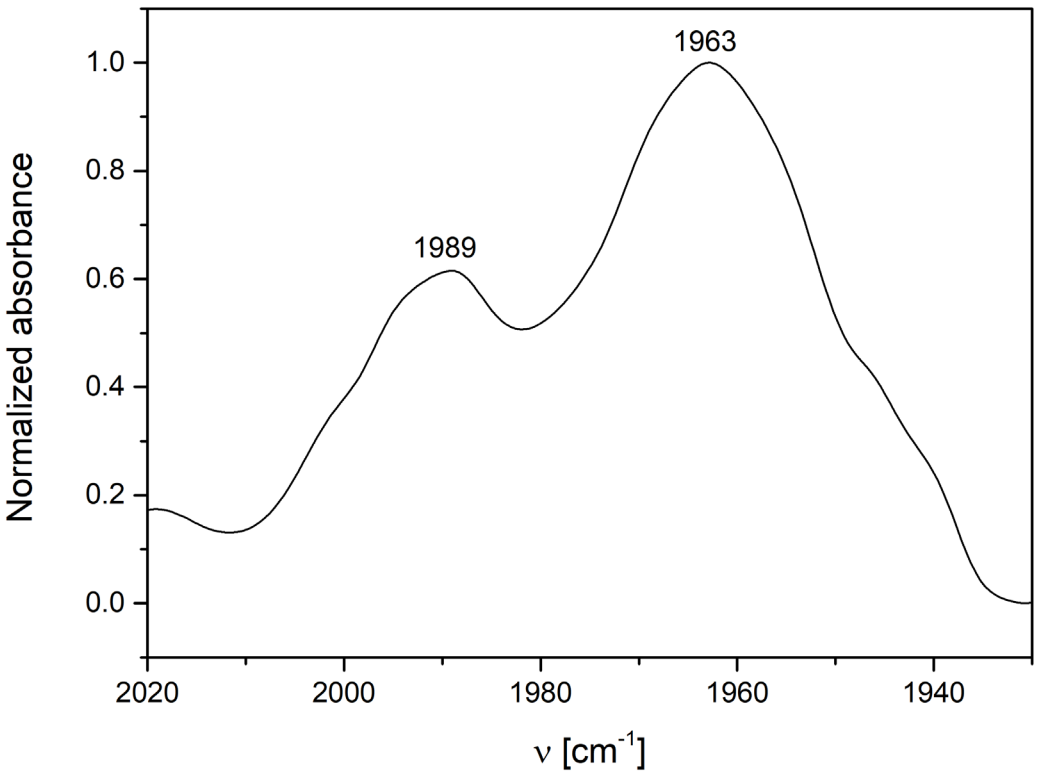

Figure S 84. IR spectrum (298 K) of a 1:2:1 mixture of Rh(acac)$(CO)_2$, **L3** and **Fe_4(Zn-L)$_6$** in a 3:2 mixture of acetonitrile and dichloromethane under 20 bar D_2/CO. [Rh] = [**Fe_4(Zn-L)$_6$**] = 1.3 mM and [**L3**] = 2.6 mM.

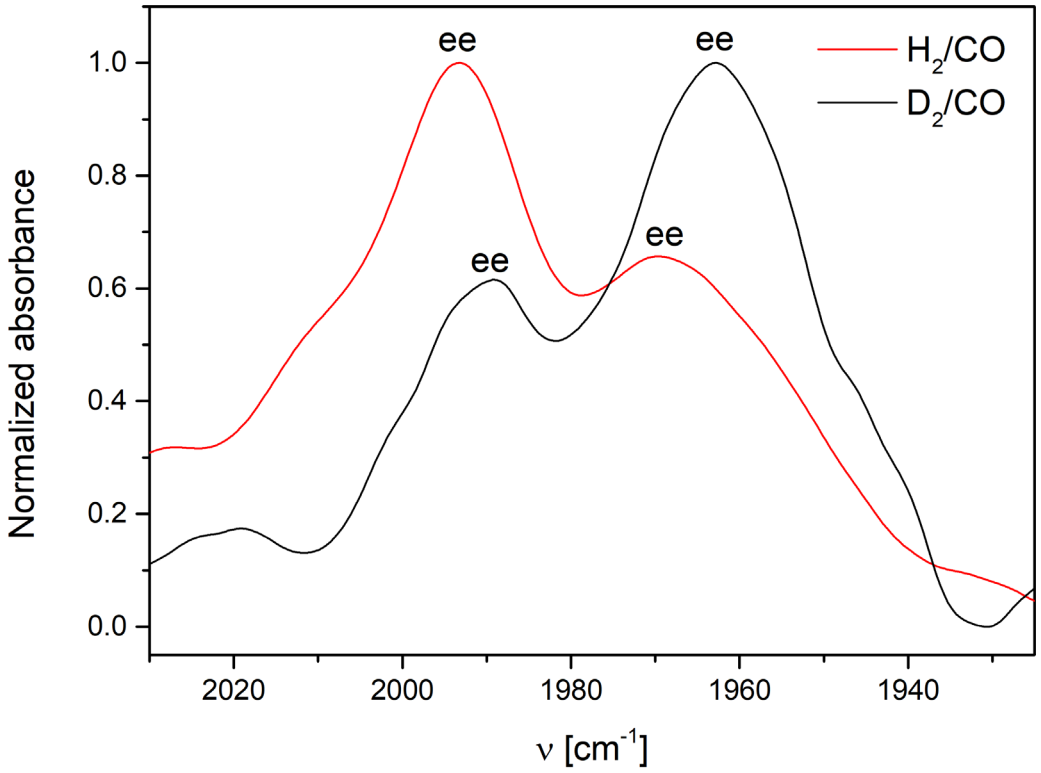

Figure S 85. Overlapped IR spectra (298 K) of a 1:2:1 mixture of Rh(acac)$(CO)_2$, **L3** and **Fe_4(Zn-L)$_6$** in a 3:2 mixture of acetonitrile and dichloromethane under 20 bar H_2/CO and D_2/CO, respectively. [Rh] = [**Fe_4(Zn-L)$_6$**] = 1.3 mM and [**L3**] = 2.6 mM.

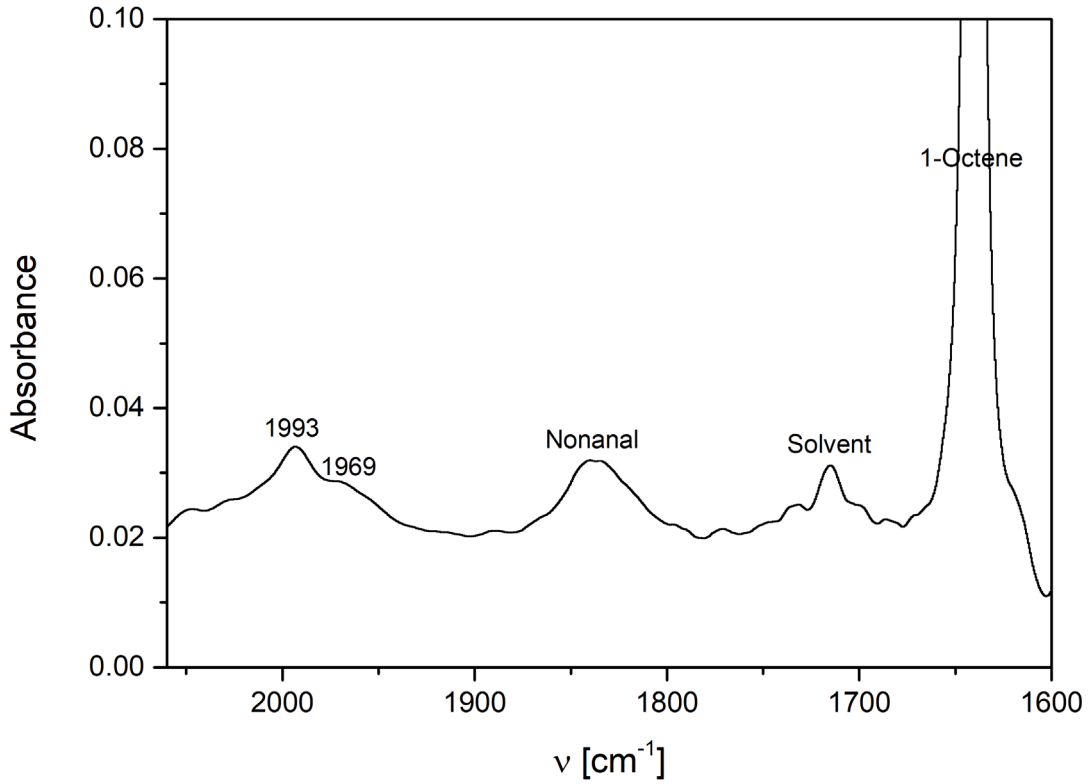

Figure S 86. IR spectrum (298 K) of a 1:2:1:200 mixture of Rh(acac)$(CO)_2$, **L3**, **Fe_4(Zn-L)$_6$** and 1-octene in a 3:2 mixture of acetonitrile and dichloromethane under 20 bar H_2/CO. [Rh] = [**Fe_4(Zn-L)$_6$**] = 1.3 mM, [**L3**] = 2.6 mM and [1-octene] = 260 mM.

10. Cage and guest volume determination

The online utility Voss Volume Voxelator[8] was used to calculate the volume of the cavity of the cage (with 0.5 Å small and 12 Å large probe radius) and of the guests (with 2 Å probe radius). A comparison of the surface areas and the volumes is displayed in Table S 12. In Figure S 87 the inner cavity volume of cage **Fe_4(Zn-L)$_6$** is shown in relation to the full volume of the cage along with the volume the active rhodium species (**ee** isomer) occupies inside the cage.

Table S 12. Surface areas and volumes for the cage **Fe_4(Zn-L)$_6$** and all the guests.

Entry	Compound	Volume (Å^3)	Occupancy factor
1	**Fe_4(Zn-L)$_6$**	1748	-
2	**L1**	422	0.24 (1 eq), 0.48 (2 eq)
3	**L2**	412	0.24 (1 eq), 0.47 (2 eq)
4	**L3**	405	0.23 (1 eq), 0.46 (2 eq)
5	**Au1**	498	0.28 (1 eq), 0.57 (2 eq)
6	**Au2**	918	0.53 (1 eq)
7	**Rh1**	928	0.53 (1 eq)
8	**Rh3**	570	0.33 (1 eq), 0.65 (2 eq)

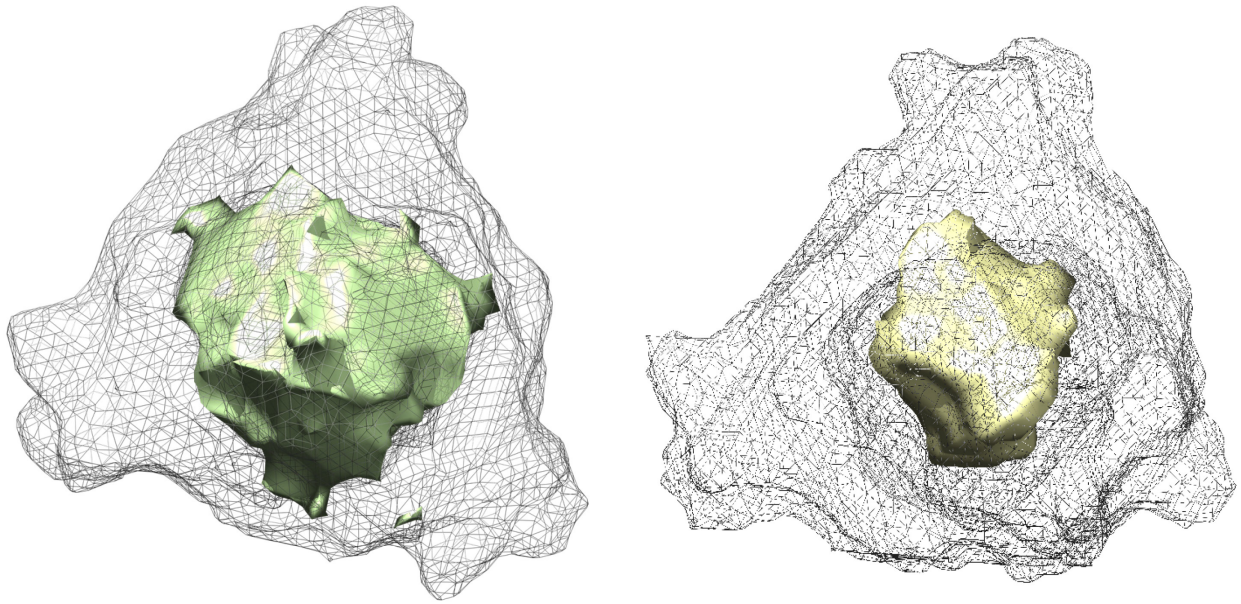

Figure S 87. (left) The inner cavity volume of cage **Fe_4(Zn-L)$_6$**. (right) The volume the active rhodium species (**ee** isomer) occupies inside the cage.

11. xTB and DFT calculations

a) Geometry optimization of catalyst-cage and substrate-catalyst-cage adducts by GFN-xTB

The geometry optimizations of the host-guest complexes were carried out with the program ADF using a tight-binding quantum chemical method (GFN-xTB) that mimics DFT and is useful for large molecular systems.[9] The vibrational spectra were computed in ADF using DFT after performing a geometry optimization on the active species structure extracted from the xTB calculated structure and by freezing all atoms except for the hydrido and CO ligands. The functional GGA BLYP-DR(BJDAMP) was used with the DZP basis set with a small frozen core. Three different host-guest complexes were computed using the method described: **Rh1@Fe_4(Zn-L)$_6$ (ee isomer)**, **Rh2@Fe_4(Zn-L)$_6$ (ea isomer)** and **Rh5@Fe_4(Zn-L)$_6$ (P-N** complex where one **L3** ligand is coordinating to rhodium through the pyridine instead of the phosphorus atom). Coordinates of the computed structures are given in a separate file. For **Rh1@Fe_4(Zn-L)$_6$ (ee isomer)** the geometries of its adducts with 1-hexene, 1-heptene and 1-octene, respectively, were also optimized using GFN-xTB.

b) Energies and structures of alkenes calculated by DFT

From the xTB-optimized substrate-catalyst-cage adducts the alkene structure (for 1-hexene, 1-heptene and 1-octene) was extracted and its Gibbs free energy was computed by single point DFT with the functional GGA BLYP-DR(BJDAMP) with the DZP basis set. For comparison, the same alkenes were geometry optimized in the absence of cage followed by calculation of their Gibbs free energy with the same functional as for the encapsulated alkenes. Δ(dG) refers to the folding energy obtained by taking the difference in the Gibbs free energy of the folded alkene (in the cage) *versus* the linear one (in the absence of cage).

c) Odd-even effect in the folding energy

The odd–even effect most likely arises from an enthalpically more favourable folding of odd numbered alkenes inside the cage. By comparing the folding energies of the encapsulated alkenes, an odd–even effect is clearly distinguishable, where odd numbered alkene 1–heptene shows a thermodynamically more favourable folding inside the cage as opposed to the even–numbered alkenes. This result suggests that odd–numbered alkenes form more stable catalyst–substrate complexes inside the cage as opposed to the even–numbered alkenes, resulting in lower reactivity explaining the observed odd–even effect.

The "alkene end" for C6, C7 and C8 compounds are all similar in structure and are probably very similarly oriented in the catalyst adducts (reactant). The next step in the catalytic cycle is a hydride transfer to the C=C bond, and locally the energy penalty for the TS should be very similar for all of these alkenes. Therefore, it can be expected that the overall TS barrier will depend on the stability of the reactant state. Since the odd alkene chain substrates feature a smaller folding energy, the corresponding reactant state is relatively more stabilized with respect to the even alkene chain counterparts. It is therefore expected that the relative TS barrier for the odd chain alkene substrate would be higher explaining its slower conversion.

It should be noted here that all the folded configurations arise from encapsulation in the cage and interaction with the catalyst. The folded geometries implicitly carry the encapsulation effect which arises from the interaction of the substrate with the cage, and the effect of forming an adduct with the catalyst. It can therefore be inferred that the quantity delta(dG) carries information about the interaction of the substrate with the cage/catalyst. A detailed quantitative analysis would require energy decomposition analysis of the entire system. Such an analysis requires advanced computational calculations, and considering the size of the caged systems are computationally intensive, and outside the scope of the present work. We suggest that the quantity delta(dG) qualitatively captures the interaction of the substrate with cage/catalyst and together with experimental results sufficiently describes the trends observed in this system.

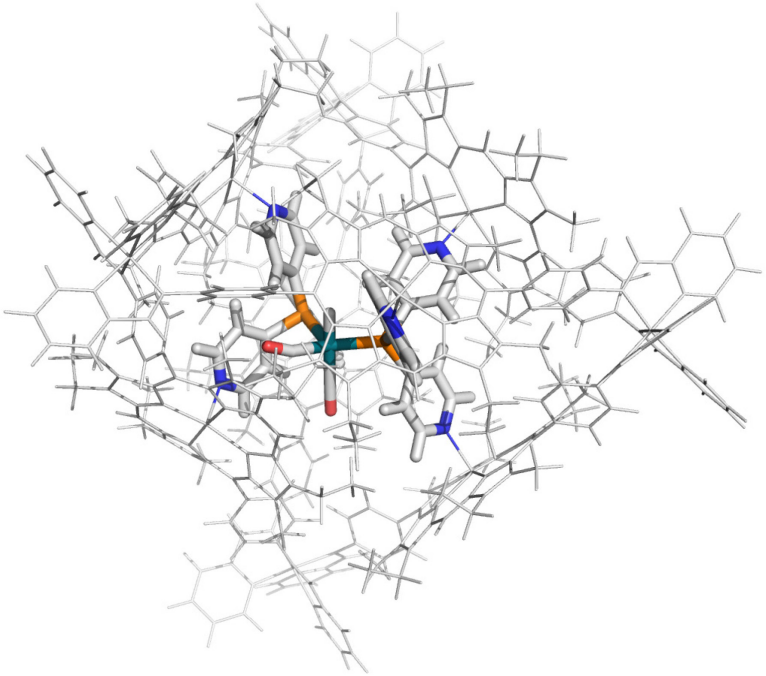

0 kcal/mol

Figure S 88. The xTB geometry optimized structure of **Rh1@Fe_4(Zn-L)$_6$ (ee isomer)**. The energy of the host-guest complex is put at 0 kcal/mol and the energies of the other host-guest complexes are compared with it.

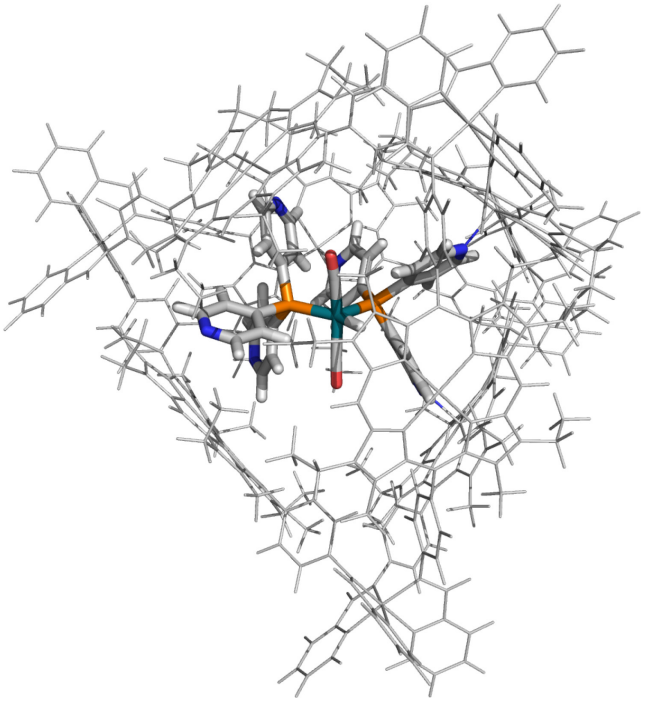

28 kcal/mol

Figure S 89. The xTB geometry optimized structure of **Rh2@Fe_4(Zn-L)$_6$ (ea isomer)**. The energy of the host-guest complex is compared to the host-guest complex with encapsulated **ee** isomer.

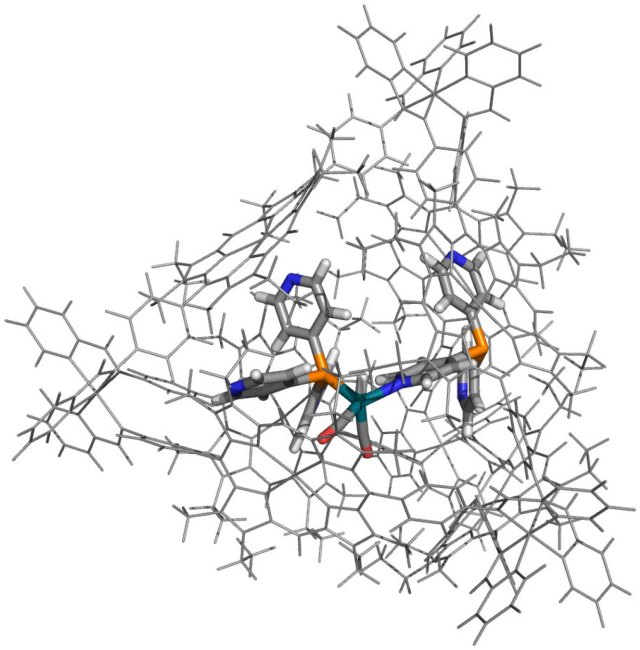

45 kcal/mol

Figure S 90. The xTB geometry optimized structure of **Rh5@Fe$_4$(Zn-L)$_6$ (P-N isomer)**. The energy of the host-guest complex is compared to the host-guest complex with encapsulated **ee** isomer.

Table S 13. Bond lengths and bond angles obtained from the xTB optimized structures.

Parameter	**ee** isomer	**ea** isomer	**P-N** isomer
Rh-P bond length	2.30 Å, 2.45 Å	2.32 Å, 2.45 Å	2.43 Å
C-Rh bond length	1.92 Å, 1.96 Å	1.92 Å, 1.93 Å	1.87 Å, 1.95 Å
H-Rh bond length	1.61 Å	1.61 Å	1.63 Å
N-Rh bond length	-	-	2.26 Å
P-Rh-P angle	117.4°	106.9°	-
N-Rh-P angle	-	-	96.3°

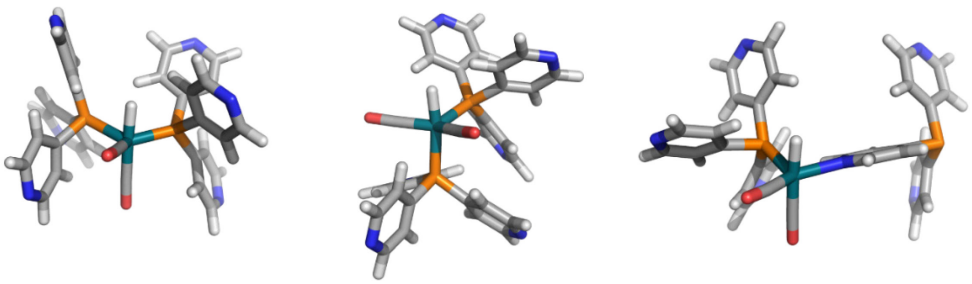

ee
0 kcal/mol

ea
21 kcal/mol

P-N
30 kcal/mol

Figure S 91. The xTB geometry optimized structures of complexes with **ee**, **ea** and **P-N** geometry extracted from the host-guest structures followed by DFT geometry optimization by freezing all atoms except for the CO and hydrido ligands. The energy of the **ee** isomer is put at 0 kcal/mol and the other isomers are compared with it.

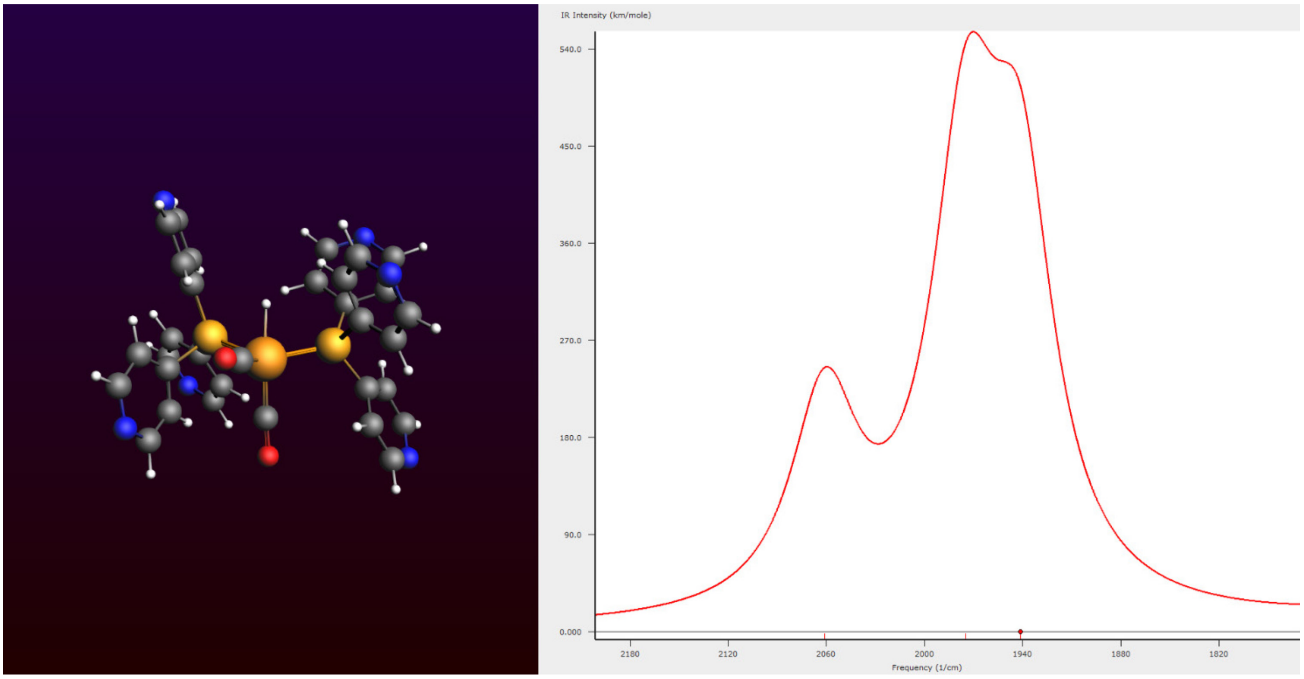

Figure S 92. DFT calculated IR spectrum of the encapsulated rhodium complex with **ee** geometry. The found vibrational frequencies are 1941, 1975 and 2061 cm^{-1}.

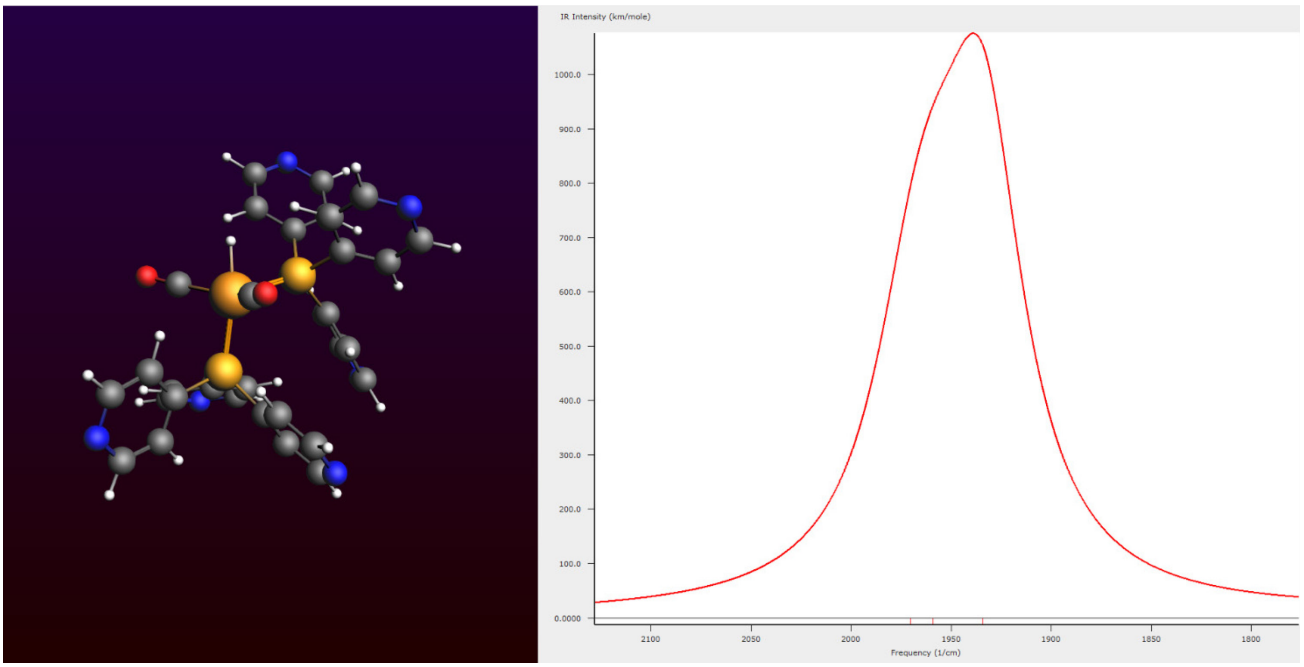

Figure S 93. DFT calculated IR spectrum of the encapsulated rhodium complex with **ea** geometry. The found vibrational frequencies are 1934, 1959 and 1970 cm^{-1}.

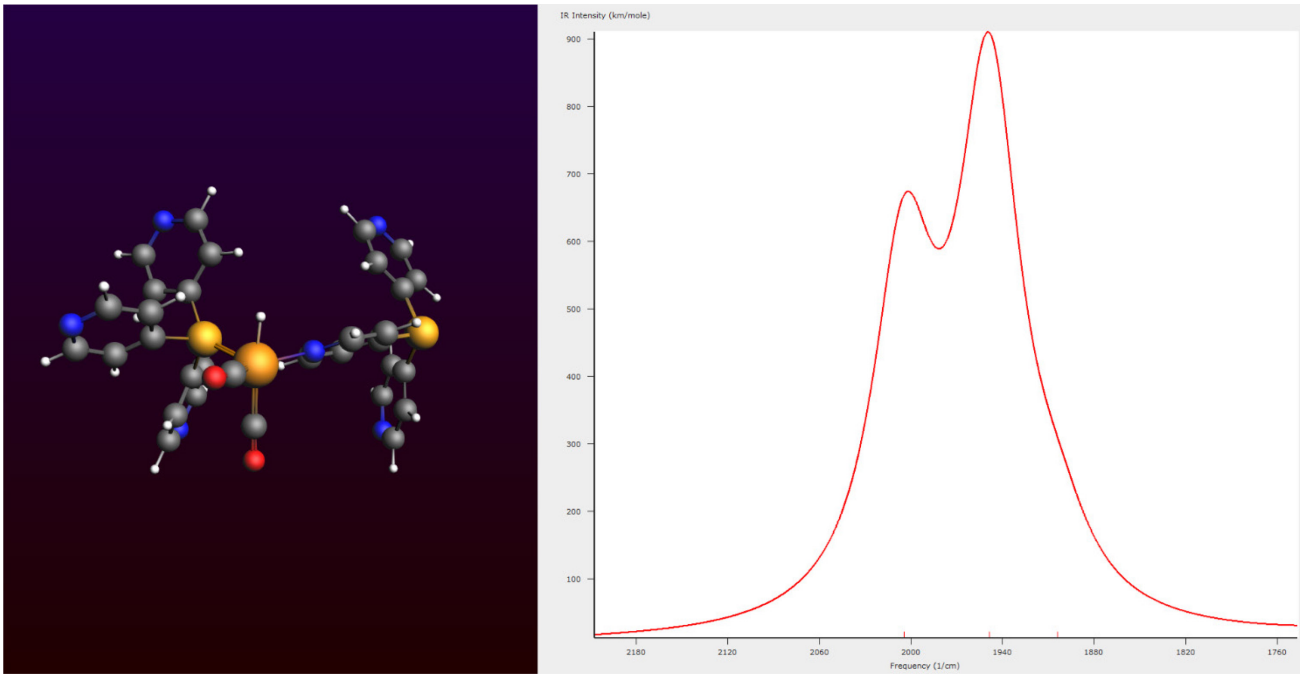

Figure S 94. DFT calculated IR spectrum of the encapsulated rhodium complex with **P-N** geometry. The found vibrational frequencies are 1904, 1949 and 2005 cm^{-1}.

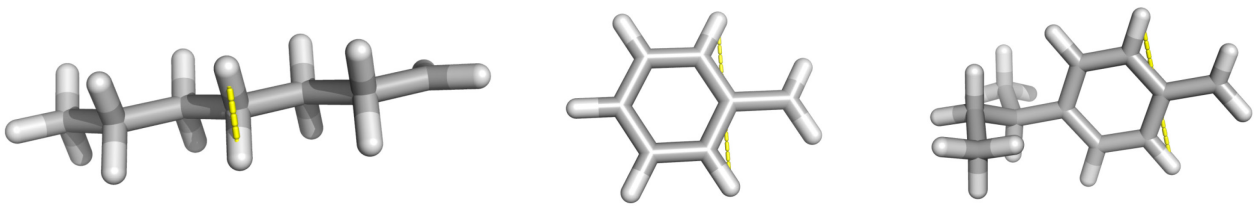

Figure S 95. Spartan geometry optimized structures of 1-octene, styrene and 4-*tert*-butylstyrene. The yellow dashed line represents the shortest H-H distance of the molecule.

12. Catalysis

All catalytic reactions were carried out in dry and degassed acetonitrile. Standard solutions for the pre-catalyst, ligand, sphere and substrate in acetonitrile were first prepared. Next, a mini autoclave (15 mL) with a separate sample container was evacuated and purged with N_2 three times. The pre-catalyst solution (1 mL) and the ligand solution (1 mL) were mixed in a dry Schlenk flask under N_2 to allow for complex formation, where after the resulting pale yellow solution was injected into the mini autoclave using a syringe with a long stainless steel needle (~ 25 cm). The autoclave was purged with 20 bar syngas ($CO:H_2$ = 1:1) three times, and subsequently pressurised with 20 bar of syngas ($CO:H_2$). The solution in the autoclave was allowed to pre-incubate for 1 h at room temperature while being stirred at 900 rpm. Next, the sphere solution (1 mL) and substrate solution (1 mL) were mixed in a dry Schlenk flask under N_2 to give a dark red-purple solution. The top part of the autoclave was de-pressurised while the bottom part of the autoclave containing the catalyst-ligand solution maintained a pressure of 20 bar syngas. The dark purple solution was injected into the sample container of the autoclave under a flow of N_2, and the

container was purged with 20 bar syngas three times. The sphere-substrate solution was injected into the autoclave with a 5 bar overpressure of syngas and the final pressure was adjusted to 20 bar. The autoclave was transferred into a pre-heated oil bath and the reaction was stirred with constant speed (900 rpm). After the reaction was finished the autoclave was cooled in an ice bath and depressurised. Two drops of *n*-tributylphosphite were added to quench the active rhodium catalyst, along with decane as an external standard. An aliquot of the reaction mixture was diluted with dichloromethane and injected into the GC directly without workup or product isolation.

Standard solutions prepared:

A: [$Rh(acac)(CO)_2$] = 0.6 mM

B: [**L3**] = 1.2 mM

C: [**Fe_4(Zn-L)$_6$**] = 0.6 mM

D: [Substrate] = 120 mM (for mixtures of substrates each substrate at 120 mM)

Upon mixing the above standard solutions as described above, the following final catalytic concentrations were obtained:

[$Rh(acac)(CO)_2$] = 0.15 mM

[**L3**] = 0.30 mM

[**Fe_4(Zn-L)$_6$**] = 0.15 mM

[Substrate] = 30 mM (for mixtures of substrates each substrate at 30 mM)

GC methods for the analysis of the hydroformylation products:

1. **Hydroformylation of 1-hexene.** Initial temperature = 30°C for 2 min, then 10°C/min to 300°C. t_R (1-hexene) = 3.68 min, t_R (linear heptanal) = 8.36 min, and t_R (branched heptanal) = 7.71 min.

2. **Hydroformylation of 1-heptene, 1-octene, 1-nonene, 1-decene, styrene and 4-tBu-styrene.** Initial temperature = 50°C for 2 min, then 10°C/min to 300°C. t_R (1-heptene) = 3.74 min, t_R (1-octene) = 5.04 min, t_R (1-nonene) = 6.62 min, t_R (1-decene) = 8.27 min, t_R (styrene) = 6.46 min, and t_R (4-tBu-styrene) = 11.66 min, t_R (linear octanal) = 8.16 min, t_R (branched octanal) = 7.58 min, t_R (linear nonanal) = 9.76 min, t_R (branched nonanal) = 9.18 min, t_R (linear decanal) = 11.30 min, t_R (branched decanal) = 10.75 min, t_R (linear undecanal) = 12.65 min, t_R (branched undecanal) = 12.13 min, t_R (linear styrene aldehyde) = 10.40 min, t_R (branched styrene aldehyde) = 9.60 min, t_R (linear 4-tBu-styrene aldehyde) = 14.16 min, t_R (branched 4-tBu-styrene aldehyde) = 12.82 min.

13. High-pressure Infrared (HP IR) studies under syngas

These experiments were performed in a stainless steel autoclave equipped with IRTRAN windows (ZnS, transparent up to 700 cm^{-1}, optical path length 0.4 mm) with mechanical stirring. The autoclave contains a separate sample container which allows for the addition of a second solution to the main chamber with an overpressure of syngas, so that the main chamber does not have to be de-pressurized.

A flame-dried schlenk was charged with nanocage **Fe_4(Zn-L)$_6$** (35.5 mg, 5.2 µmol) and dry and degassed acetonitrile (2.1 mL) and dichloromethane (1.4 mL) was added to yield a dark purple solution. In a separate flame-dried schlenk flask Rh(acac)$(CO)_2$ (1.34 mg, 5.2 µmol) and **L3** (2.76 mg, 10.4 µmol) were dissolved in acetonitrile (0.3 mL) and dichloromethane (0.2 mL) to yield a pale yellow solution. Next, the cage solution was injected into the main chamber of the autoclave under a flow of N_2. The autoclave was purged with 20 bar H_2/CO three times, where after it was pressurized to 20 bar H_2/CO. Following this, the catalyst solution was injected into the separate sample container under a flow of N_2, without de-pressurizing the main chamber. The sample container was also purged with 20 bar H_2/CO three times, where after it was pressurized to 30 bar H_2/CO. The solution in the autoclave was heavily stirred with a mechanical stirrer and after an equilibration time of 20 min a background spectrum was collected. Finally, the content of the sample container was added to the main chamber, and a series of measurements were started. For the deuteride exmperiments the same procedure was repeated using D_2/CO instead of H_2/CO. When no cage was used in an experiment, the background spectrum was collected with pure acetonitrile at 20 bar syngas.

14. Cage stability under hydroformylation conditions

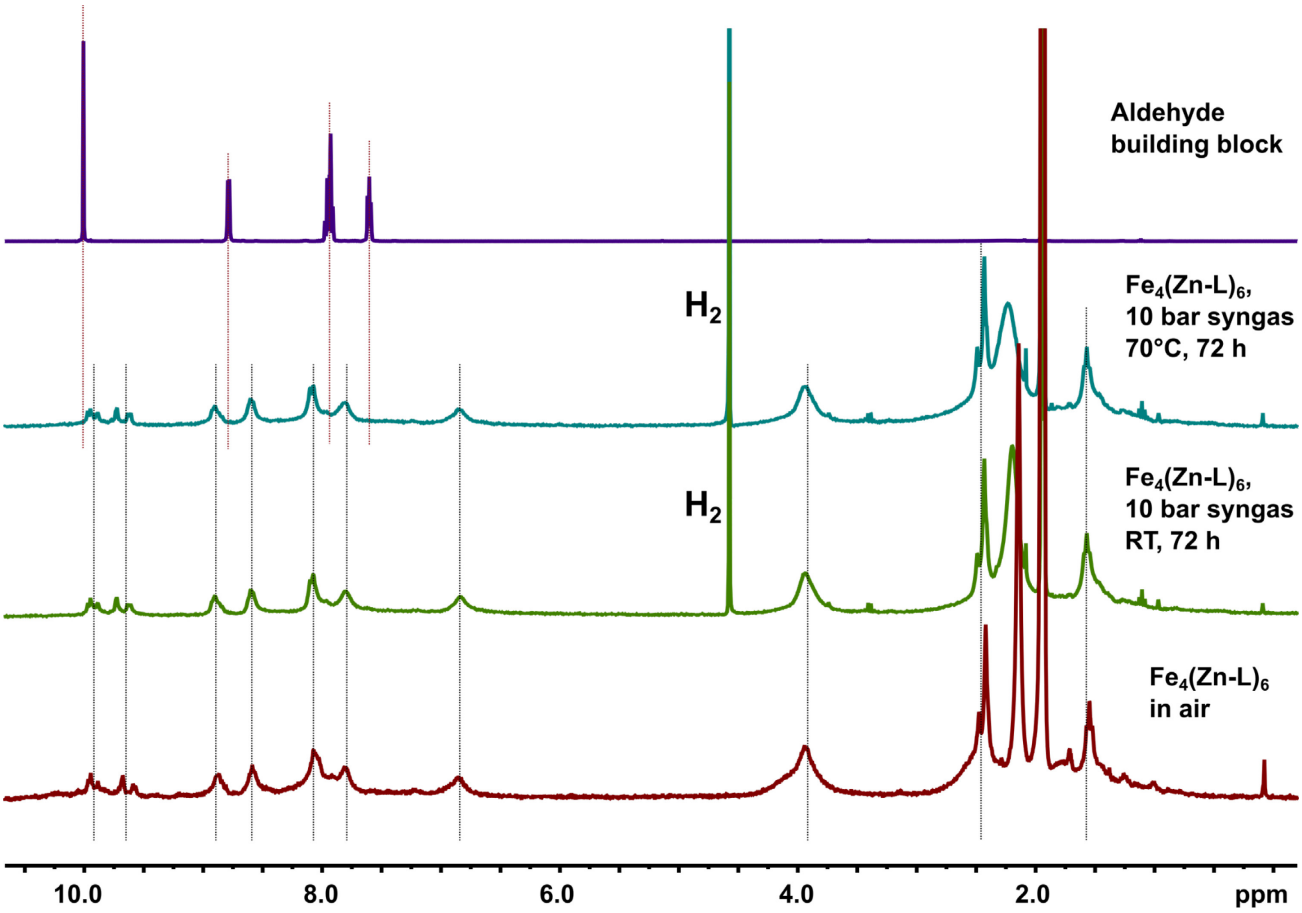

Figure S 96. Cage stability under hydroformylation conditions. (top) Aldehyde building block. (second from top) **Fe_4(Zn-L)$_6$** at 10 bar syngas at 70°C for 72 h. (second from bottom) **Fe_4(Zn-L)$_6$** at 10 bar syngas at room temperature for 72 h. (bottom) **Fe_4(Zn-L)$_6$** in air. The black dotted lines show that all cage spectra overlap, confirming the stability of the cage under the applied conditions. The red dotted lines show that no aldehyde building block is formed, also confirming the stability of the cage.

15. General titration fitting procedure

Fitting procedure

Regardless of the supramolecular model and spectroscopic method, the fitting procedure for the determination of the association constants is as follows: At each titration point *n* in *N* (the total number of titration points) the initial concentrations for the host and guess species $[H]_{0,n}$ and $[G]_{0,n}$ are known, as are the observed values for either chemical shift $\delta_{atom,obs,n}$ or absorption $A_{\lambda,obs,n}$, which we will collectively call $O_{obs,n}$. The fitting procedure is based around the COBYLA numerical optimization routine[10] which tries to minimise the difference between the observed values and calculated values, given the constraint that association constants and concentrations are greater than zero:

minimize $\quad F_n = \left|O_{obs,n} - O_{calc,n}\right|, \qquad n \in N$

subject to $\{[S]_n; K; \alpha\} \geq 0$ $n \in N$, for all species S = {H, G, HG, HGG, …}

The objective function F_n for the optimisation procedure calculates $O_{calc,n}$ through the formulae for A_λ or δ_{atom} (*vide supra*). E.g. in the case of a 1:1 HG titration followed by UV-vis, the objective function becomes:

$$F_n = \left|O_{obs,n} - O_{calc,n}\right| = \left|A_{obs,n} - A_{calc.n}\right| = \left|A_{obs,n} - \epsilon_H[H] + \epsilon_{HG}[HG]\right|$$

Given initial guesses for the association constants {K; α}, [H] and [HG] can be calculated from the initial concentrations $[H]_0$ and $[G]_0$. Since the fitting procedure calls this routine very often (in our cases roughly between 10^2 and 10^6 times per fitting procedure, depending on the size of the problem (e.g. HG versus HGG)), we use a 'rapid numerical integration algorithm for finding the equilibrium state of a system of coupled binding reactions'.[11] The objective function is then evaluated using initial guesses for the species coefficients (δ or ε), and the optimisation routine determines whether a minimum has been found or that the initial guesses have to be adjusted to provide a better fit to the data.

When a minimum has been found, the error distributions (difference between calculated and observed values) are visually checked for trends. If trends are observed that point towards a different model (e.g. cooperativity *versus* no cooperativity, or HGG *versus* HGGG), these models are fitted to the data as well and the different error distributions are compared between models.

Initial guesses and quality of fit

Since multi-parameter optimisations are difficult problems to accurately solve (many parameters, few observables), the quality of the fit should be scrutinised: The microscopic association constant in larger (e.g. 1:2) systems should be in the range for the same constant in the 1:1 system in the same solvent. The species coefficients (δ or ε) have to make sense, such that e.g. in the case of a HHHG system where the host H is tracked by UV-vis, the relation $\epsilon_{HG} \approx \frac{1}{2}\epsilon_{HHG} \approx \frac{1}{3}\epsilon_{HHHG}$ should hold, since the absorptivity per 'bound host' molecule shouldn't change appreciably in the system. Initial guesses for the optimisation procedure are made using similar, simplified relations and ideas, where e.g. in a HHHG UV-vis titration, almost all host molecules are bound in the HG form at the end of the titration curve, allowing for an estimate of ε_{HG} and thereby estimates of all other coefficients. Starting from these 'proper' guesses, the optimisation routine is generally both fastest *and* most accurate.

The accuracy of these optimisations turns out to be an ill-defined problem in supramolecular chemistry.[12] Our current understanding of this problem (after fitting a broad range of 'bad' and 'good' titrations), is that non-accurate additions during titrations translate *directly* into a noisy energy landscape with a noisy minimum. Combined with the fact that optimisation routines can never guarantee to find a global minimum, the found minimum is heavily dependent on the quality of the titration data and on the direction through which the minimum is approached (i.e. the initial guesses). Thus, when a minimum is found by the optimisation routine, we approach this minimum from multiple sides to assure this is in fact a global minimum, or to get an estimate on the size of the minimum. E.g. if we approach a one-dimensional problem from two extreme initial guesses and find minima at 900 and 1100, respectively, we conclude that the actual minimum is somewhere between these values and thereby immediately get a rough estimate of the accuracy with which we can determine the association constant.

The good/bad fitting to different binding models

In this article only 1:1, 1:2 and 1:3 host-guest stoichiometries have been fitted using an online software (*vide infra*). The fitting of all the acquired data is always first attempted with a 1:1 host-guest binding model. A 1:1 model can always be disqualified when the titration curves lack isosbestic points as this

means that a simple transition from one species (H) to another one (HG) does not occur. Only the titration between **Fe_4(Zn-L)$_6$** and **Py** displays clear isosbestic points and gave the best fit with a 1:1 binding model. For all other studied guests (**L1**, **L2**, **L3** and **Au1**) the isosbestic point is lost at some point in the titration and for all these titrations both a 1:2 and 1:3 binding model was fitted. Higher stoichiometries (1:4, 1:5 and 1:6) could not be accurately fitted as these will not be filled at the guest concentrations applied in the titration. By comparing the R^2 values of the 1:2 and 1:3 fits along with their error distributions, we could determine which model fits the experimental data the best. Specifically, we look at the overall error magnitude in addition to possible trends in the error distribution which show whether the fit is good or bad.

Software used to fit all titration data

An in-house developed script was used to fit all the acquired titration data and the online script is available here: http://limhes.net/optim/

The software is developed by Dr. René Becker, previously affiliated with the University of Amsterdam. The software has been experimentally validated with known literature systems (e.g. Zn^{II}TPP with pyridine) and gives association constants consistent with literature values. Moreover, the software has been applied to many literature systems and is successfully used in five peer-reviewed publications.[13–17]

Information about the software taken from the website:

On the webpage binding/association constants from titration data can be determined using any equilibrium model. Commonly known approximation methods such as the Benesi–Hildebrand or Scatchard plot are not used, but a non-linear optimization is applied to fit the observed titration data to calculated titration data, which is calculated by numerically solving equilibrium concentrations from a set of binding constants and equilibrium reactions. Therefore, the equilibrium species concentrations do not have to be algebraically solved (Hunter's method; recently implemented by Thordarson at Supramolecular.org), which limits the equilibrium models to 1:1, 1:2 and 2:1 stoichiometries. The website offers functionality similar to HypNMR.

System of equilibria / supramolecular system

The example system is a 2:1 (HHG) system, where a host molecule H (B) can bind to a guest molecule G (AA) according to the chemical equilibrium depicted below. The 'host molecule' is defined as the molecule whose initial concentration remains constant for each point in the titration, since this is the molecule whose (changing) properties are going to be tracked. The guest molecule's initial concentration is increased over the course of the titration.

$$AA + 2B \overset{2K_1}{\longleftrightarrow} AA \cdot B + B \overset{\frac{1}{2}K_2}{\longleftrightarrow} AA \cdot B_2$$

Binding constants (microscopic/macroscopic), statistical factors and cooperativity parameters

In this supramolecular system, the equilibrium constants K_1 and K_2 are the so-called microscopic binding constants, which can be seen as the binding constant that would be observed in the case of 1:1 binding for identical molecular binding sites. The factors 2 and ½ are statistical factors which can very often be deduced by simple reasoning: there are 2 paths to go from AA to AA·B (either the left side binds, or the right side binds), but only 1 path to go from AA·B to AA. The statistical factor is then 2/1 = 2. For the second equilibrium, the reasoning is the same: there is only 1 path to go from AA·B to AA·B_2 (only one

side can bind, the other is already bound), but there are 2 paths to go from $AA{\cdot}B_2$ to $AA{\cdot}B$ (remove bound species from either left or right side). The statistical factor is then 1/2 = ½.

When the system is *non-cooperative*, this means that the first binding event does not influence the second binding event, and $K_1 = K_2 = K_{ass}$. When the system is *cooperative*, the opposite holds, and the microscopic association constants are not equal. In this software, we depict this inequality through cooperativity parameters, as in $K_1 = K_{ass}$ and $K_2 = \alpha_1 \cdot K_{ass}$.

Concentrations, observed values and coefficients

To determine the association constant K_{ass} and the cooperativity parameter α_1 for the system described above, a titration is performed by keeping the initial host concentration $[H]_0$ constant, while incrementing the initial guest concentration $[G]_0$. For each point on the titration curve, some (e.g. spectroscopically, calorimetrically, ...) experimentally observed value O_{exp} is recorded. These initial concentrations and experimentally observed values should be entered in the DATA tab.

How the software does its job

The software then calculates "observed" values $O_{calc} = \beta_H \cdot [H] + \cdots + \beta_{HHG} \cdot [HHG]$. The coefficients $\beta_{species}$ are e.g. the molar extinction coefficients $\epsilon_{species}$ (for UV-vis titrations) or the chemicals shifts $\delta_{species}$ (for NMR titrations) of the respective species, which are optimized by the software and whose initial guesses should be entered in the FITTING tab. The equilibrium concentrations of the species present in the system ([H], [G], [HG] and [HHG]) are calculated from the initial concentrations $[H]_0$ and $[G]_0$, K_{ass} and α_1 using a numerical algorithm developed by D. Bray and S. Lay. The values for K_{ass} and α_1 are also optimized by the software (that's the whole point!) and their initial guesses should also be entered in the FITTING tab. The software optimizes these values by minimizing the error between O_{calc} and O_{exp}.

16. References

[1] R. J. Bowen, A. C. Garner, S. J. Berners-Price, I. D. Jenkins, R. E. Sue, *J. Organomet. Chem.* **1998**, *554*, 181–184.

[2] M. A. Weiner, P. Schwartz, *Inorg. Chem.* **1975**, *14*, 1714–1716.

[3] T. E. Müller, J. C. Green, D. M. P. Mingos, C. M. McPartlin, C. Whittingham, D. J. Williams, T. M. Woodroffe, *J. Organomet. Chem.* **1998**, *551*, 313–330.

[4] A. Helms, D. Heiler, G. McLendon, *J. Am. Chem. Soc.* **1992**, *114*, 6227–6238.

[5] C. Poriel, Y. Ferrand, S. Juillard, P. Le Maux, G. Simonneaux, *Tetrahedron* **2004**, *60*, 145–158.

[6] D. M. Wood, W. Meng, T. K. Ronson, A. R. Stefankiewicz, J. K. M. Sanders, J. R. Nitschke, *Angew. Chem. Int. Ed.* **2015**, *54*, 3988–3992.

[7] M. Holz, X. A. Mao, D. Seiferling, A. Sacco, *J. Chem. Phys.* **1996**, *104*, 669–679.

[8] N. R. Voss, M. Gerstein, *Nucleic Acid Res.* **2010**, *38*, W555-562.

[9] S. Grimme, C. Bannwarth, P. Shushkov, *J. Chem. Theory Comput.* **2017**, *13*, 1989–2009.

[10] M. J. D. Powell, in *Adv. Optim. Numer. Anal.*, Springer Netherlands, Dordrecht, **1994**, pp. 51–67.

[11] D. Bray, S. Lay, *Comput. Appl. Biosci.* **1994**, *10*, 471–6.

[12] D. Brynn Hibbert, P. Thordarson, *Chem. Commun.* **2016**, *52*, 12792–12805.

[13] P. Li, S. Amirjalayer, F. Hartl, M. Lutz, B. de Bruin, R. Becker, S. Woutersen, J. N. H. Reek, *Inorg. Chem.* **2014**, *53*, 5373–5383.

[14] R. Becker, S. Amirjalayer, P. Li, S. Woutersen, J. N. H. Reek, *Sci. Adv.* **2016**, *2*, e1501014.

[15] X. Wang, S. S. Nurttila, W. I. Dzik, R. Becker, J. Rodgers, J. N. H. Reek, *Chem. Eur. J.* **2017**, *23*, 14769–14777.

[16] S. S. Nurttila, R. Becker, J. Hessels, S. Woutersen, J. N. H. Reek, *Chem. Eur. J.* **2018**, *Accepted*.

[17] S. Derossi, R. Becker, P. Li, F. Hartl, J. N. H. Reek, *Dalt. Trans.* **2014**, *43*, 8363–8367.